**Schlüsseltechnologien /
Key Technologies
Band / Volume 155
ISBN 978-3-95806-265-8**

JÜLICH
FORSCHUNGSZENTRUM

Schlüsseltechnologien
Key Technologies

155

Graphene Devices for Extracellular Measurements

Dmitry Kireev

Member of the Helmholtz Association

JÜLICH
FORSCHUNGSZENTRUM

Graphene Devices for Extracellular Measurements

Dmitry Kireev

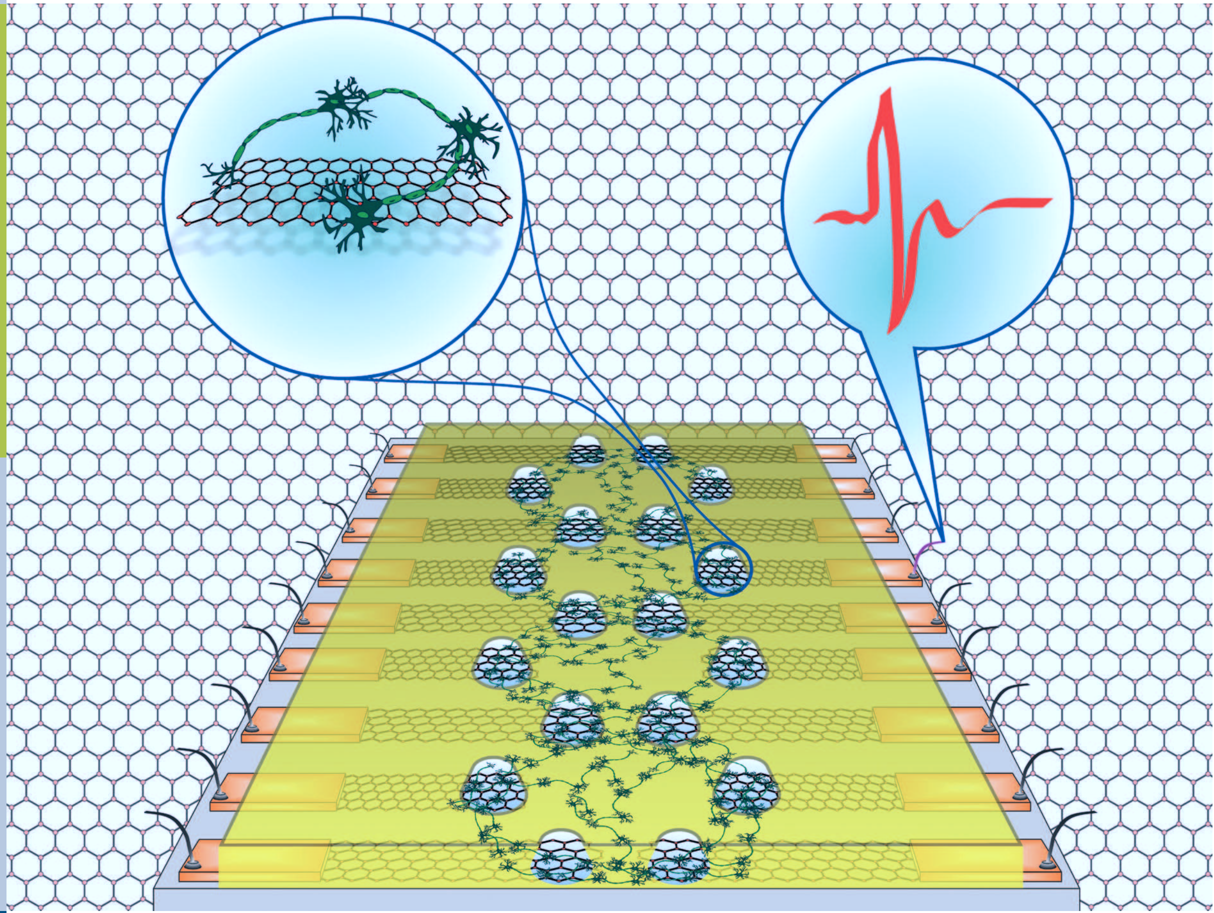

**Schlüsseltechnologien /
Key Technologies
Band / Volume 155
ISBN 978-3-95806-265-8**

JÜLICH
FORSCHUNGSZENTRUM

Schriften des Forschungszentrums Jülich
Reihe Schlüsseltechnologien / Key Technologies Band / Volume 155

Forschungszentrum Jülich GmbH
Institute of Complex Systems
Bioelectronics (ICS-8)

Graphene Devices for Extracellular Measurements

Dmitry Kireev

Schriften des Forschungszentrums Jülich
Reihe Schlüsseltechnologien / Key Technologies Band / Volume 155

ISSN 1866-1807 ISBN 978-3-95806-265-8

Bibliographic information published by the Deutsche Nationalbibliothek.
The Deutsche Nationalbibliothek lists this publication in the Deutsche Nationalbibliografie; detailed bibliographic data are available in the Internet at http://dnb.d-nb.de.

Publisher and Distributor: Forschungszentrum Jülich GmbH
Zentralbibliothek
52425 Jülich
Tel: +49 2461 61-5368
Fax: +49 2461 61-6103
Email: zb-publikation@fz-juelich.de
www.fz-juelich.de/zb

Cover Design: Grafische Medien, Forschungszentrum Jülich GmbH

Printer: Grafische Medien, Forschungszentrum Jülich GmbH

Schriften des Forschungszentrums Jülich
Reihe Schlüsseltechnologien / Key Technologies, Band / Volume 155

D 82 (Diss. RWTH Aachen University, 2017)

ISSN 1866-1807
ISBN 978-3-95806-265-8

The complete volume is freely available on the Internet on the Jülicher Open Access Server (JuSER)
at www.fz-juelich.de/zb/openaccess.

Abstract

Recording extracellular potentials from electrogenic cells (especially neurons) is the hallmark destination of modern bioelectronics. Graphene is a promising material, which possesses features relevant to bioelectronics applications. Graphene-based electrode arrays (GMEAs) and more complicated graphene field effect transistors (GFETs) comprise a new type of bioelectronic device application. Biocompatibility, stability, excellent and unique electronic properties, scalability, and pure two-dimensional structure make graphene the perfect material for bioelectronic applications. The advantages of graphene as part of such devices are numerous: from a general flexibility and biocompatibility to the unique electronic properties of graphene.

In this work, the GMEAs and GFETs are fabricated using CVD–grown graphene and a scalable cleanroom-based technology. The devices are fabricated on both rigid and flexible substrates.

In order to ensure a wafer-scale fabrication of the devices, a new high throughput graphene transfer technique is established. The technique allows me to use just 4 cm^2 of CVD-grown graphene to fabricate a whole 4-inch wafer with 52 chips on it.

Rigid GFETs, fabricated on different substrates, with a variety of channel geometries (width/length), reveal a linear relation between the transconductance and the width/length ratio. The area normalized electrolyte-gated transconductance is in the range of 1-2 $\text{mS V}^{-1}\ \square$, and does not strongly depend on the substrate. Influence of the ionic strength on the transistor performance is investigated as a part of the work. Double contacts are found to decrease the effective resistance and the transfer length, but do not improve the transconductance. An electrochemical annealing/cleaning effect is investigated and proposed to originate from the out-of-plane gate leakage current. The devices are used as a proof-of-concept for bioelectronic sensors, recording external potentials from *ex vivo* heart tissue and *in vitro* cardiomyocyte-like cells (HL-1). Via multichannel measurements we are able to record and analyze both difference in action potentials as well as their spatial propagation through the chip. The recordings show distinguishable action potentials with a signal to noise ratio over 14 from *ex vivo* tissue and over 6 from the cardiac-like cell line *in vitro*. Furthermore, I accomplished *in vitro* recordings of neuronal signals with a distinguishable bursting activity for the first time.

Flexible GFETs are fabricated on polyimide substrates and exhibit extremely large transconductance values, up to 11 mS/V, and a mobility over 1750 $\mathrm{cm}^2\,\mathrm{V}^{-1}\,\mathrm{s}^{-1}$. Furthermore, controllably flexible polyimide-on-steel (PIonS) substrates are able to record *ex vivo* electrical signals from a primary embryonic rat heart tissue.

Rigid GMEAs are used for extensive *in vitro* studies of a cardiac-like cell line and cortical neuronal networks. They show excellent ability to extracellularly record the action potentials with signal to noise ratios up to 116 for HL-1 cells and up to 100 for the spontaneous bursting-spiking neuronal activity. Complex neuronal bursting activity patterns as well as a variety of HL-1 action potentials are recorded with the GMEAs.

Flexible GMEAs show extracellular recordings from *ex vivo* heart tissue with excellent signal-to-noise ratios up to 80 and from *in vitro* HL-1 cells with SNR up to 30. The use of flexible polyimide substrates in combination with graphene‘s physical and biological stability results in good cell-interface properties and is promising for further applications. Due to the transparency of these devices, the concept can be extended for optogenetic experiments.

Furthermore, a new fabrication design and flow has been explored in the thesis, aimed for prospective, more specific *in vivo* probes and their use as bio-implants.

Zusammenfassung

Messungen extrazellulärer Aktionspotentiale von elektrisch aktiven Zellen (insbesondere Neuronen) ist einer der Meilensteine der modernen Bioelektronik. Graphen ist ein Material mit vielen vielversprechenden Eigenschaften, relevant für diverse bioelektronische Anwedungen.

Graphen-basierende Mikroelektroden Arrays (GMEAs) und die komplizierteren Graphen Feldeffekt Transistoren (GFETs) umfassen eine neue Art von bioelektronischen Bauelementen. Biokompatibilität, Stabilität, ausgezeichnete und einzigartige elektronische Eigenschaften, Skalierbarkeit und seine reine zweidimensionale Struktur machen Graphen zu einem perfekten Material für bioelektronische Anwedungen. Die Vorteile von Graphen als Teil dieser Bauelemente sind vielzählig: von einer generellen Flexibilität und Biokompatibilität zu den einzigartigen elektrischen Eigenschaften von Graphen.

Die GMEAs und GFETs in dieser Arbeit wurden mit CVD-gewachsenem Graphen und mittels einem skalierbaren Reinraum Prozess hergestellt. Dabei wurden sowohl rigide als auch flexible Substrate verwendet.

Um eine skalierbare Wafer-basierte Fabrikation der Bauelemente sicher zu stellen wurde eine Hochdurchsatz-Graphentransfer Technik entwickelt und etabliert. Die Technik ermöglicht es, ein nur 4 cm^2 großes Stück von CVD-gewachsenem Graphen für die gesamte Fabrikation eines 4-zoll Wafers mit 52 Chips zu benutzen.

Die rigiden GFETs, hergestellt auf verschieden Substraten mit einer Vielzahl verschiedener Kanalgeometrien (Breite/Länge) zeigen einen linearen Zusammenhang zwischen der Transkonduktanz und dem Verhältnis von Kanalbreite zu Länge. Die flächennormierte elektrolyt-gesteuerte Transkonduktanz befindet sich in einem Bereich von 1-2 mS V^{-1} □ und ist nicht stark abhängig von dem Substrat. Der Einfluss der Ionenstärke auf die Leistung der Transistoren wurde als Teil dieser Arbeit untersucht. Doppelkontakte zeigten einen reduzierten effektiven Widerstand, sowie Transferlänge, jedoch keine Verbesserung der Transkonduktanz. Ein elektrochemischer Glüh-/Reinigungseffekt wurde untersucht und es wird vorgeschlagen, dass dieser durch den Gate-Leckstrom hervorgerufen wird. Die Bauelemente werden als Marbarkeitsnachweis für bioelektronische Sensoren zur Aufnahme von extrazellulären Potentialen von *ex vivo* Herzmuskelgewebe und *in vitro* kardiomyozyt ähnlichen Zellen (HL-1) benutzt. Mit Hilfe von multikanal Messungen können die unterschied-

lichen individuellen Aktionspotentiale, sowie ihre örtliche Ausbreitung über den Chip gemessen und analysier werden. Die Aufnahmen zeigen unterscheidbare Aktionspotentiale mit einem Signal-zu-Rausch Verhältnis von über 14 für *ex vivo* Gewebe und über 6 für die kardiomyozyt-ähnliche Zelllinie *in vitro*. Desweiteren gelang es uns zum ersten Mal *in vitro* Aufnahmen von neuronalen Signalen mit unterscheidbaren Entladungssalven zu machen.

Flexible GFETs wurden auf Polyimidsubstraten hergestellt und weisen extrem große Transkonduktanzen von bis zu 11 mS/V und Mobilitäten von bis zu 1750 $\text{cm}^2\,\text{V}^{-1}\,\text{s}^{-1}$ auf. Weitergehend waren kontrollierbar flexible Polyimid-auf-Stahl (engl. Polyimide-on-steel: PIonS) Substrate in der Lage elektrische Signale *ex vivo* von primärem embrionalen Rattenherzgewebe aufzunehmen.

Rigide GMEAs wurden für umfangreiche *in vitro* Studien von herzähnlichen Zelllinien, sowie kortikalen neuronalen Netzwerken benutzt. Sie zeigten herausragende Leistungen für die Aufnahme von extrazellulären Aktionspotentialen mit einem Signal-zu-Rausch Verhältnis von bis zu 116 für HL-1 Zellen und bis zu 100 für die spontanen Entladungssalven der Neuronenaktivität. Die komplexen Muster der neuronalen Entladungssalven wurden, ebenso wie eine Viehlzahl von HL-1 Aktionspotentialen, mit Hilfe der GMEAs aufgenommen.

Flexible GMEAs zeigen extrazelluläre Aufnahmen von *ex vivo* Herzgewebe mit herausragenden Signal-zu-Rausch Verhältnissen von bis zu 80 und von bis zu 30 von *in vitro* HL-1 Zellen. Der Einsatz von flexiblen Polyimidsubstraten in Kombination mit Graphens physikalischer und biologischer Stabilität resultiert in guten Eigenschaften für die Zell-Chip Schnittstelle und ist vielversprechend für weitere Anwedungen. Durch die intrinsische Transparenz dieser Bauelemente kann das Konzept für optogenetische Experimente erweitert werden.

Als Abschluss dieser Arbeit wird ein neues Design, sowie ein neuer Prozessablauf untersucht und auf zukünftige, spezifischere *in vivo* Elektroden und deren Einsatz als Implantate abgestimmt.

Contents

Chapter 1

Introduction

Mammalian organisms are very complex structures, which operate via even more complex biochemical reactions. In order to understand their functions and behavior, one must understand individual cellular activities. What is important, the two main organs - brain and heart - partially consist of electrogenic cells. While the details, peculiarities and functions of these cells are different, the basis of the electricity in such cells is ionic flows throughout the cellular membrane. Such ionic flow generates the extracellular potential changes. The extracellular potentials are in the range that modern electronics already has the ability to detect accurately, therefore a new research field, at the convergence of biology and electronics has been developed: bioelectronics. Electrophysiology, as a part of bioelectronics, studies the electrical properties of the biological cells and tissues (from single cells to whole organs). The electrophysiology is aimed at recording the intracellular and extracellular electrical potentials of cells in order to study their functions. Knowledge of the cellular functions leads to deeper understanding of the organ's functions, and to further understanding their malfunctions (diseases), finding way to predict, prevent, or mimic the functions, therefore treat the diseases.

While patch-clamp remains the main electro-physiological tool [1, 2], planar microelectrode arrays (MEAs) [3–6] and field effect transistors (FETs) [7–9] have gained their relevance in recording extracellular signals, therefore being non-invasive. Both of them, FETs and MEAs are traditionally used for a variety of *in vitro* studies from different biological cells and tissues [5,10–12]. The MEAs' performance was studied for decades [13,14]. Planar gold, titanium, and platinum, are the most commonly exploited electrode materials [15–20]. In particular, it became clear that decreasing the electrode's impedance would in general improve the recording performance. Since that became widespread in the electrophysiological community, many interesting approaches and devices have appeared: from simply electrodeposited electrodes [19] and porous metals [17, 21] to bundles of carbon nanotubes (CNTs) [22, 23], nanocavity electrodes [24, 25], and micro 3D electrodes [26, 27]. Many carbon-based nanomaterials, such as CNTs (bundles of CNTs), black carbon, porous carbon, etc. have been implemented for fabrication of the MEAs and gained interest due to their simplicity, biocompatibility, and excellent conductivity [28–30]. Biocompatibility of the graphene used in this work was also studied specifically and it was shown that neurons prefer to grow on graphene. The details can be found in Appendix E of this thesis.

The FETs, used for electrophysiological recordings are, classically, silicon-based [7, 8, 31]. The years of silicon research makes the Si-based FETs an important building block of electrophysiological recordings [32], specially considering the many break-through advances, that made it possible to fabricate flexible and even biodegradable probes [33]. Silicon nanowire-based transistors show a great applicability to such applications, as shown in a large number of works [34–36]. However, usually silicon-based FETs are comparably large in size, and they still introduce glia scars and other tissue responses if inserted *in vivo* and are rather fragile.

Graphene, an allotrope of carbon [37], has gained its attraction to scientists in various fields since 2004 [38]. Starting with discovery of its field effect, it raised up into the adjacent subjects of biology and bioelectronics [39–41]. In the field of electrophysiology, graphene has gained influence in cellular interfacing and signal recordings [42–44]. There it can be used either actively as a transistor's active area [45] or passively as an electrode [46, 47]. While the graphene transistors require at least two electrodes and complicated electrochemical gating, in the case of GMEAs there is just one feedline required for an electrode. Moreover, such graphene-based devices are comparably easy to fabricate, characterize and use.

In spite of the above-mentioned trend towards 3D architectures, graphene devices result in a totally opposite approach; since it is a truly two dimensional material with its charge carriers freely open to the surrounding environment. Combination of the graphene's excellent electronics properties and its pure flatness, if exploited in a correct way, can even outperform the 3D-structured electrodes. Considering the recent research [48–50], graphene might be a superior material, especially for neuronal interfacing. For neuronal interfaces, with axonal sizes in the sub-micron range, it is easier to form a good coupling towards the graphene surface rather than engulf a 3D electrode. Moreover, graphene's transparency is already an advancement compared to the conventional gold or platinum MEAs, and allows direct on-electrode observation of cellular viability through the substrate.

Interestingly, it was found that graphene transistors, biased via a liquid, exhibits a very impressive gating behavior [45, 51–53]. The change of reference electrode potential from zero to 500 mV is usually enough to move from p-type to n-type regime through the Dirac point. At the same time, the conductivity curve is very steep and the resulting transconductance, in some cases, can be as high as 11 mS V^{-1}.

CVD-grown graphene was utilized in this thesis to fabricate the graphene multielectrode arrays (GMEAs) and graphene field effect transistors (GFETs). Transconductance, mobility, and noise of the GFETs have been analyzed in the thesis. The GFETs and GMEAs are further implemented for the study of conventional cellular cultures: the cardiac-like cell line HL-1 and more complex primary cortical neuronal cultures. The overall simplicity of the fabrication process, together with the wafer-scale approach results in low-cost and easy-to-reproduce devices. HL-1 cultures are ideal for testing new devices due to their stable and repetitive generation of action potentials (AP). The multiple HL-1 cultures have provided us with a large amount of different recordings, APs and their shapes, recorded via the GMEAs and GFETs. Activity of the complex cortical neuronal networks was recorded with the GFETs and GMEAs, resulting in a huge number of extracellular activities with different spikes' shapes, amplitudes and patterns. Low noise recordings combined with good coupling allow us to detect cardiac extracellular activity with signal-to-noise ratio (SNR) over 116 and neuronal bursting activity with a SNR up to 100.

The GFETs are fabricated on different substrates: SiO_2/Si, sapphire, HfO_2, polyimide (PI), and controllably flexible polyimide-on-steel (PIonS). Polyimide is a flexible and biocompatible polymer, what is widely used as a substrate in biosensing applications due to its robust structure, chemical, mechanical, and biological stability [54]. Additionally, the absence of dangling bonds makes it a perfect substrate for interfacing with graphene.

This work proves the applicability of the truly two-dimensional material, graphene, for the complex job of *in vitro* and *ex vivo* electrophysiological recordings. Additionally, an initial platform for future *in vivo* measurements based on new, GFET- and GMEA-based *in vivo* probes is developed.

The thesis is structured as follows: **Chapter 2** presents the fundamentals on graphene, graphene transistors and electrodes and a basic introduction to the electrophysiology of biological cells. In **Chapter 3**, important information regarding methods, measurements and cell culture techniques is given. **Chapter 4** deals with a new method for graphene transfer, so-called "high-throughput transfer", which is important for low-cost and large-scale fabrication of the devices described in the following chapters. The two sections of **Chapter 5** deal with research on rigid and flexible graphene field effect transistors (GFETs), consecutively. Their use for electrophysiological measurements, including heart tissue, cardiac and neuronal cells is presented. **Chapter 6** continues with study on rigid and flexible graphene-based microelectrode arrays and their electrophysiological application. The last, **Chapter 7** concludes the results part with design and fabrication of brand new *in vivo* probes for use in neuroprosthesis and, in the future, brain research. **Chapter 8** summarizes the thesis and gives outlooks for future improvements and applications of the devices.

The above-described research resulted in five manuscripts, that are published by the moment of the thesis submission [52, 55–58].

Chapter 2

Fundamentals and Theory

2.1 Graphene

2.1.1 Electronic Properties of Graphene

Carbon is one of the most abundant elements on Earth. Two of the most well-know allotropes of carbon are *diamond* (sp^3) and *graphite* (sp^2) [59]. However, as research always goes forward, new allotropes of carbon have been found, such as *fullerenes*, C_{60}, which is a zero-dimensional material (0D) [60]. *Carbon nanotubes*, the one-dimensional (1D) allotrope of carbon have been introduced in 1991 [61]. It took just a decade for the research community to complete the carbon family with the last, and long ago predicted to be the most promising unit - *graphene* [38].

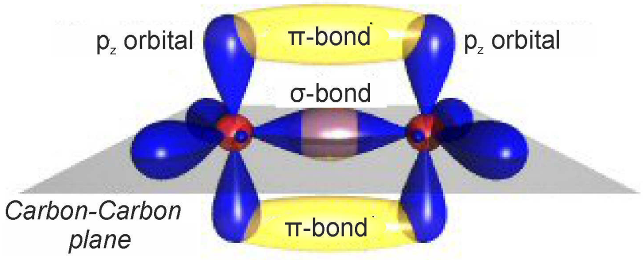

Figure 2.1: The sp^2 hybridization and σ-bonds and π-bond formed in graphene.

As each Carbon molecule has six electrons: two are core electrons and four valence electrons, one $2s$ and three $2p$ orbitals are created. The single $2s$ orbital hybridizes with two $2p$ orbitals, forming three "σ bonds" in the x-y plane in a characteristic angle of 120°C. The remaining $2p$ orbital is perpendicular to the x-y plane , and forms the so called "π-bond".

Graphite, which is a multi-layered stack of single graphene layers, is the typical example of sp^2 hybridization, where σ bonds create a strong in-plane binding, while the inter-layer bonding is related to the π-bonds and weak Van-der-Waals forces. Therefore graphite is well known for it's softness, used for example, in pencils. However, the band structure of graphite reveals the interaction of the valence and conduction bands therefore graphite is a so-called semi-metal and a good conductor [62].

When graphene (a single layer of graphite) is taken into consideration, the sp^2 bonding provides excitingly remarkable properties, such as absence of a bandgap at the K-points (also known as *Dirac points*) and linear energy dispersion near the Fermi level. In some considerations (close to the Fermi level) it is possible to describe graphene as a "2D gas of massless Dirac fermions". For comparison, for typical semiconductors the energy-momentum relation is quadratic, and can be solved by the Schrödinger equation:

$$E = \frac{p^2}{2m^*} \tag{2.1}$$

where p is the momentum and m^* is mass of charge carriers. As for graphene, the energy dispersion is linear (near Fermi level), carriers must be considered as massless and relativistic particles, and can be solved by the Dirac equation.

$$E = \nu|p|, \text{where } c/\nu \cong 300, \tag{2.2}$$

where ν is the Fermi velocity and c is the speed of light.

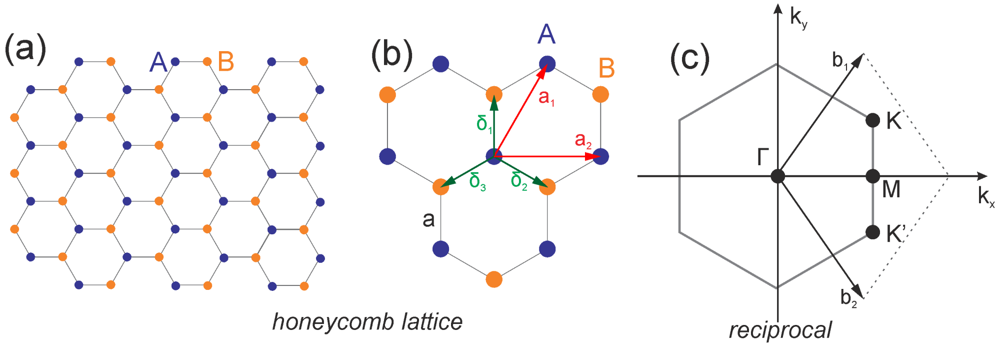

Figure 2.2: (a) schematics of the graphene honeycomb lattice which is split in two sub-lattices (A – blue; B – yellow). (b) Closer look into the neighbor cells, showing vectors $\mathbf{a_{1,2}}$, connecting atoms within one sub-lattice and vectors $\delta_{\mathbf{1,2,3}}$, connecting atoms of sub-lattice A with three atoms of sub-lattice B. (c) The Brillouin zone, a single unit cell in a reciprocal space, showing vectors $\mathbf{b_{1,2}}$, which are corresponding to the vectors $\mathbf{a_{1,2}}$ in real space. Adapted from [63].

A perfect sheet of graphene has a hexagonal lattice structure with a distance to the closest neighbor a = 0.142 nm. The electronic structure of graphene can be in general solved by an orthogonal nearest-neighbor tight-binding model [64]. In order to do so, the whole hexagonal graphene lattice can be divided into two equivalent sub-lattices (with atoms A and B). The further simplification can be done by finding the symmetry points via the lattice vectors, which are [62]:

$$\boldsymbol{a_1} = \frac{a}{2}(3, \sqrt{3}), \qquad \boldsymbol{a_2} = \frac{a}{2}(3, -\sqrt{3}). \tag{2.3}$$

The corresponding reciprocal lattice vectors are:

$$\boldsymbol{b_1} = \frac{2\pi}{3a}(1, \sqrt{3}), \qquad \boldsymbol{b_2} = \frac{2\pi}{3a}(1, -\sqrt{3}). \tag{2.4}$$

The three nearest neighbors of an atom A in real space (see Figure 2.2b) are the three atoms of type B with their vectors given as [62]:

$$\boldsymbol{\delta_1} = \frac{a}{2}(1, \sqrt{3}), \qquad \boldsymbol{\delta_2} = \frac{a}{2}(1, -\sqrt{3}), \qquad \boldsymbol{\delta_3} = -a(1, 0). \tag{2.5}$$

For the first approximation, a nearest-neighbor (n.n.) tight-binding Hamiltonian has the simple form:

$$H_{n.n.} = -t \sum_{<ij=n.n.>,\sigma} (\boldsymbol{a}^{\dagger}_{i,\sigma}\boldsymbol{b}_{j,\sigma} + H.c.) \tag{2.6}$$

where **t** denotes the numerical value of the nearest neighbor hopping matrix element, and is expected to be around 2.8 eV, and H.c. stands for conjugate Hamiltonian. As there is one π-orbital, which is oriented normal to the x-y plane, which is unfilled with electrons, it can accommodate two electrons with spin σ ($\sigma = \uparrow, \downarrow$). The orbital on atom i with spin σ can be denoted as (i, σ), and the $\boldsymbol{a}_{i,\sigma}(\boldsymbol{a}^{\dagger}_{i,\sigma})$ is an operator of annihilation (creation) of such an electron. The reduced Planks constant, $\hbar$ is considered equal to 1 for the calculations.

In order to get a realistic model one has to include also the second nearest neighbor hopping (from atoms A to other atoms A). Their location coordinates are:

$$\boldsymbol{\delta'_1} = \pm\boldsymbol{a_1}, \qquad \boldsymbol{\delta'_2} = \pm\boldsymbol{a_2}, \qquad \boldsymbol{\delta'_3} = \pm(\boldsymbol{a_2} - \boldsymbol{a_1}). \tag{2.7}$$

The overall tight-binding Hamiltonian for electrons that can hop to nearest neighbor as well as to second-nearest neighbor atoms [63]:

$$H = -t \sum_{<i,j>,\sigma} (\boldsymbol{a}^{\dagger}_{\sigma,i}\boldsymbol{b}_{\sigma,j} + H.c.) - t' \sum_{<i,j>,\sigma} (\boldsymbol{a}^{\dagger}_{\sigma,i}\boldsymbol{a}_{\sigma,j} + \boldsymbol{b}^{\dagger}_{\sigma,i}\boldsymbol{b}_{\sigma,j} + H.c.). \tag{2.8}$$

where t' is the next nearest neighbor hopping energy.

The energy bands, derived from this Hamiltonian have the following form [63]:

$$E_{\pm}(\mathbf{k}) = \pm t\sqrt{3 + f(\mathbf{k})} - t' f(\mathbf{k}); \tag{2.9}$$

$$f(\boldsymbol{k}) = 2\cos(\sqrt{3}k_y a) + 4\cos\left(\frac{\sqrt{3}}{2}k_y a\right)\cos\left(\frac{3}{2}k_x a\right), \tag{2.10}$$

where the plus sign is related to the upper π^*-band, and the minus sign to the lower π-band. From the equations it is seen that if $t' = 0$ (no next nearest neighbor hopping), the spectrum is symmetric around zero energy (see Figure 2.3a-b). For non-zero t' values, the electron-hole symmetry is broken, and the π and π^* bands are asymmetric. Typical values of t' are known to be in the range of $0.02t \leq t' \leq 0.2t$ [63–65].

By expanding the full band structure (eq. 2.9) close to the Dirac points (**K** and **K'**), which are known to be:

$$\boldsymbol{K} = \left(\frac{2\pi}{3a}, \frac{2\pi}{3\sqrt{3}a}\right), \qquad \boldsymbol{K} = \left(\frac{2\pi}{3a}, \frac{2\pi}{-3\sqrt{3}a}\right),$$

the dispersion relation is found to be:

$$E_{\pm}(\boldsymbol{q}) = \pm\nu_F|\boldsymbol{q}| \tag{2.11}$$

where $\boldsymbol{q}$ is the momentum, relative to Dirac points, $\nu_F \approx c/300$ is the Fermi velocity, and c is the speed of light. This is a significantly different and unique dispersion relation compared to normal semiconductors (shown in equation 2.1). Graphene's dispersion relation (2.11) does not depend on the mass of the charge carriers and linearly depend to $\boldsymbol{q}$ in the first order approximation. The dispersion relation in the second order approximation also does not depend on the charge carrier's mass, however, the addition of next nearest neighbor and its hopping energy t' only brakes the electron-hole symmetry as discussed above.

2.1.2 Graphene Synthesis

Monolayer graphene has been synthesized in a variety of different ways [67, 68]. Below is summary of the four main fabrication methods.

Micromechanical exfoliation from a bulk graphite is historically the first and technologically the easiest method [38]. Although the graphene, fabricated in such a way is of a high quality, the results are irregular in terms of flake shape, size and composition. A large number of new test electronic devices have been fabricated and analyzed utilizing the micromechanically exfoliated graphene, however no large-scale fabrication is possible.

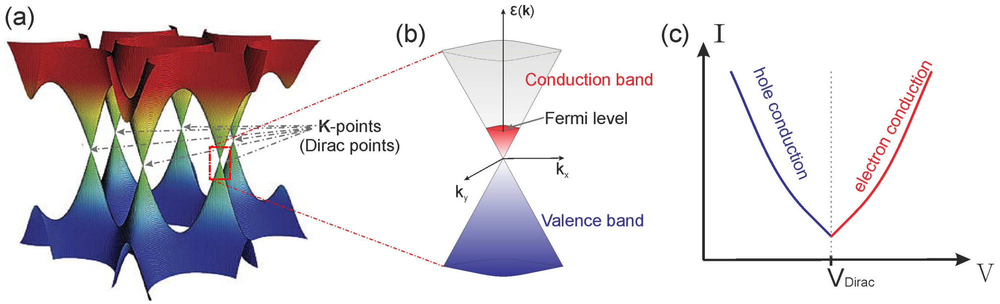

Figure 2.3: (a) Energy spectrum dispersion in the graphene lattice in the n.n. approach, showing the six Dirac points, where the conductance and valence band coalesce. Adapted from [66]. In (b) is shown a simplified zoom into one of the Dirac cones, showing how position of the Fermi level influences the graphene's properties. Any intrinsic or extrinsic factors may dope the graphene and therefore shift the Fermi level. In a best case, the typical GFET's conductance plot is shown in (c), and in a case of un-doped, pure graphene lattice the $V_{Dirac} = 0$.

Chemical vapor deposition (CVD) graphene is grown on metallic catalytic surfaces under high temperatures and a carbon-containing gas environment [73]. The development of the technique has evolved since the first reported growth [74]. As on Ni and other metals, it turned out to be difficult to control precisely the number of grown layers. The CVD growth on a copper (Cu) surface resulted in a so-called "purely surface-mediated CVD process". Since the solubility of carbon in copper is minimal, the graphene can form a layer only through complete decomposition of the gas into the Cu surface and the process is limiting: as soon as a single layer graphene (SLG) is formed, the process is slows down/stops. Graphene used in this thesis is CVD-grown, and the details of the growth are given in the Section 3.1.

Graphitization of SiC surface is another possible approach [70]. In the method, graphene is formed via vacuum annealing of the SiC substrates. During the high-temperature annealing, the atoms of Si diffuse into the bulk, leaving the C-C layer on the surface. Depending on the face of the SiC crystal, different results can be achieved: either SLG with one "buffer" graphene layer or multilayers of graphene. However, the SiC substrates are expensive and do not provide the dielectric control of the graphene, as SiO_2/Si does, for example.

Liquid-phase exfoliation and fabrication of graphene is also possible, and as perceivable from the name, the method is highly scalable [72]. There are many different approaches, but most consist of exfoliating the graphite or graphite-oxide in a liquid, then dispersing/spin-coating it on the destination substrate. The method is very scalable, although it is difficult to achieve the single layer graphene coverage over a large area.

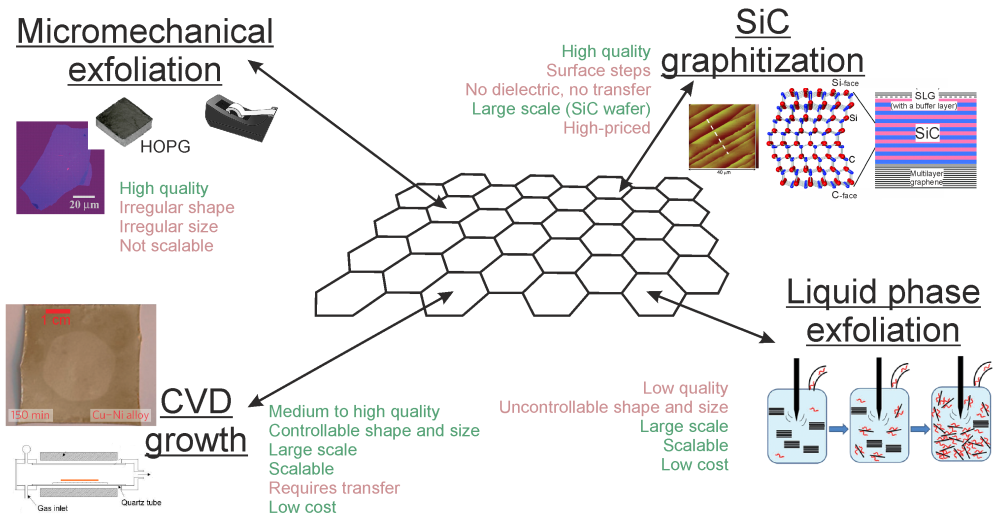

Figure 2.4: The overview of the main graphene fabrication methods, such as mechanical exfoliation, graphitization of SiC, liquid phase exfoliation and CVD growth. Primary advantages and drawbacks are shown and based on the current state of the technologies. The figure is partially adapted from [38, 69–72].

2.2 Graphene Transistors

A transistor is a semiconducting electrical element that is used to amplify or switch electrical signals upon application of an external bias. The meaning of *transistor* comes from two words: *trans*fer and var*istor* [75]. A simple transistor has three terminals: source, drain and gate. The current, I_{DS}, is flowing through the channel upon application of the drain-source potential, V_{DS}. The current can be modulated upon application of the gate-source potential, V_{GS}.

In a classical silicon-based field effect transistor, the channel conductivity is a parameter of the semiconductor (Si), which has a bandgap (indirect; 1.1 eV), and therefore is usually not conducting at $V_{GS} = 0$ (*OFF-state*). Upon application of an external field, the Fermi level of the semiconductor is shifted and the channel conductivity increases (*linear regime*). However, it reaches a limit at some point (*saturation regime*). The silicon-based transistors have a long history of development, going back almost 60 years. During the years, a consistent down-scaling in channel size has been evident, and reached 10 nm per node in 2017. However, there are some classical limitations to the scaling, which, in short, rule that further scaling will be impossible. That is because at lower dimensions the quantum effects, such as tunneling, will be more pronounced and the classical device operation will not be possible [76]. Therefore, new approaches are taken into consideration by the scientific community. One of these approaches is implementation of carbon nano materials, specially

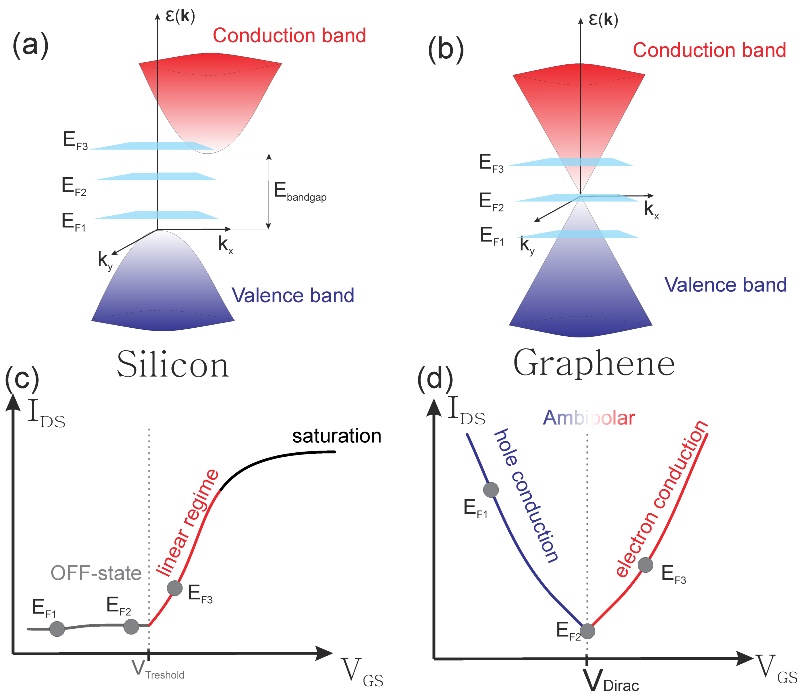

Figure 2.5: Comparison between operation procedure and physics behind Si-based unipolar FET and graphene-based ambipolar FET. In (a) and (b) are shown (schematically), the energy dispersions of the silicon and graphene, and three points of the Fermi level, which are commensurate to the applied V_{GS} potential. The bandgap of silicon is shifted in order to represent a more realistic case, since it is an indirect bandgap semiconductor. In (c) and (d) are shown the $I_{DS} - V_{GS}$ curves of the Si-based and graphene-based devices. As seen for the Si-devices, the energy gap is large, and the performance depends on the position of the intrinsic Fermi level, and the resulting I-V curve is mostly uni-polar, with a linear regime and a saturation (due to a limited number of charge carriers and their mobility). Graphene, as a zero-gap semiconductor, upon a small gate potential, jumps into either hole or electron conductivity, and therefore is an ambipolar transistor.

CNTs and graphene for the application, since they are intrinsically thin and governed by quantum effects [38, 77].

Graphene-based transistors were first proposed by Geim and Novoselov in their Nobel-prize winning publication in 2004, showing graphene's response to an applied external potential [38]. Further developments and research had shown that indeed, theoretical predictions are not far from reality, and in special conditions the GFETs can exhibit extremely large mobilities, up to $1 \times 10^5 - 1 \times 10^6$ cm^2 V^{-1} s^{-1}. However, the values are obtained on of exfoliated graphene, suspended and measured in a close-to-zero temperature [78–81]. If more common and ambient conditions are taken into account, the mobility is usually in the range of 1000-50000 cm^2 V^{-1} s^{-1}, depending on the quality of graphene, it's growth, transfer, fabrication details, etc. [82]. Nevertheless, the value is still extremely large, especially if compared to that of silicon nanowires, which is in the range of ∼1000 cm^2 V^{-1} s^{-1} [83].

However, as discussed in the section above, graphene does not have a real bandgap, therefore it is still conducting in the *OFF-state* as well. This factor makes it a bad example for a general logic applications, but great for other applications, such as sensing, biosensing, high-frequency application, etc [84]. Some approaches exist to open a band gap in graphene, but they are out of the scope of this thesis.

For the biosensing applications, such as electrophysiology, the important parameter of the I-V sweep curve is the transconductance. Transconductance is the factor of how much the drain-source current is changed (measured) upon changes in the gate potential (cellular signals). The comparison between typical Si-FETs and GFETs, is given in Figure 2.5. The highest transconductance up to now recorded in the GFETs is 11 mS/V, which is outperforming the Si-FETs by a factor of two [52].

A general GFET's I-V curve is given in the Figure 2.5d, showing a cone-like behavior of the current flowing through the channel (y-scale) upon applied electrical field to the gate dielectric (x-scale). The current is first dominated by holes, then reaches the minimum at the Dirac point, where the number of charge carriers is minimal, and then increases again, but is then dominated by electrons. The overall relation in the linear regimes of the plots can be expressed by the following formula [82]:

$$I_{DS} = \frac{W}{L} \cdot C_{ox} \cdot \mu \left(V_{GS} - V_{Dirac}\right) \cdot V_{DS}, \tag{2.12}$$

where I_{DS}, V_{DS}, and V_{GS} are the drain-source current, drain-source voltage and gate-source voltage consecutively; V_{Dirac} is the Dirac potential, or charge neutrality point; μ is mobility, C_{ox} is the gate oxide's capacitance, W and L and the width and length of graphene's conducting channel.

If all geometrical and measurement parameters are known, the two parameters, transconductance (g) and mobility (μ), can be computed:

$$g = \frac{\partial I_{DS}}{\partial V_{GS}}; \qquad \mu = \frac{L}{W} \cdot \frac{g}{C_{ox} V_{DS}} \tag{2.13}$$

As seen from the formulas 2.13, transconductance, g, is the amplification factor, as well as, a sensitivity factor when the GFET is used for sensor applications. Mobility, on the other hand, is a more complicated property of a material, and is related to the oxide capacitance, or interface capacitance in the case of liquid gating.

Liquid-gated graphene field effect transistors were first fabricated and measured in 2010 by two groups independently [42, 44]. As it turned out, the graphene is fully stable in the electrolyte environment, even upon application of sufficiently large electric fields (e.g. more than 1.4V in 1x PBS). An electrical double layer (EDL) is formed at the interface of the graphene and electrolyte if a potential is applied and plays a role of a dielectric/oxide compared to classical GFETs. The EDL's structure, composition and dielectric properties are still under a careful examination, but as known to date, there are three main capacitances which are arranged in series (see Figure 2.6a) [44, 58, 85]:

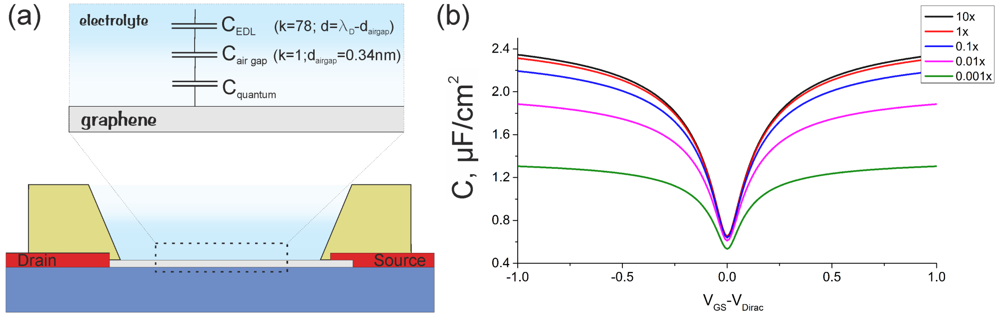

Figure 2.6: (a) Schematics of a typical graphene-based transistor and the simplified electrical circuit used for the calculations of the interfacial capacitance given in the inset. (b) The results of the modeling, with capacitance being a parameter of the used electrolyte (its molarity) and the gate potential.

1. **EDL** with a thickness equal to the Debye length, which is dependent on the electrolyte's molarity, M. Dielectric permittivity is considered to be equal $\epsilon_r = 78$. The details on EDL, its formation mechanisms and peculiarities is given in Section 2.3:

   $$C_{EDL} = \frac{\epsilon_r \epsilon_0}{\lambda_D}; \qquad \lambda_D = \frac{0.304}{\sqrt{M}}\ [\text{nm}]$$

   where ϵ_0 is vacuum permittivity, and λ_D is the Debye length.

2. **Air gap capacitance**, which appears due to hydrophobicity of the graphene. Dielectric permittivity is assumed to be that of air ($\epsilon_{air} = 1$), and of thickness, d, is considered as graphene's interlayer distance, 0.3 nm [44, 85]. The air gap capacitance in our case is used as a term, following the relevant literature, but, in general, it plays role of a Stern layer (see section 2.3):

   $$C_{airgap} = \frac{\epsilon_{air} \epsilon_0}{d}$$

3. **Quantum capacitance**, which is an inherent property of graphene [86–88], as dis-

cussed in details in Section 5:

$$C_Q = \frac{2e^2}{\hbar \nu_F \sqrt{\pi}} \cdot \sqrt{|n_G| + |n^*|},$$
$$n_G = \left(\frac{eV_{GS}}{\hbar \nu_F \sqrt{\pi}} \right)^2 .$$

where e is the elementary charge, $\hbar$ is reduced Planck constant, $\nu_F \approx c/300$ is the Fermi velocity (c is the speed of light). n_G and n^* are the charge carrier concentrations, induced by gate potential and charged impurities, correspondingly.

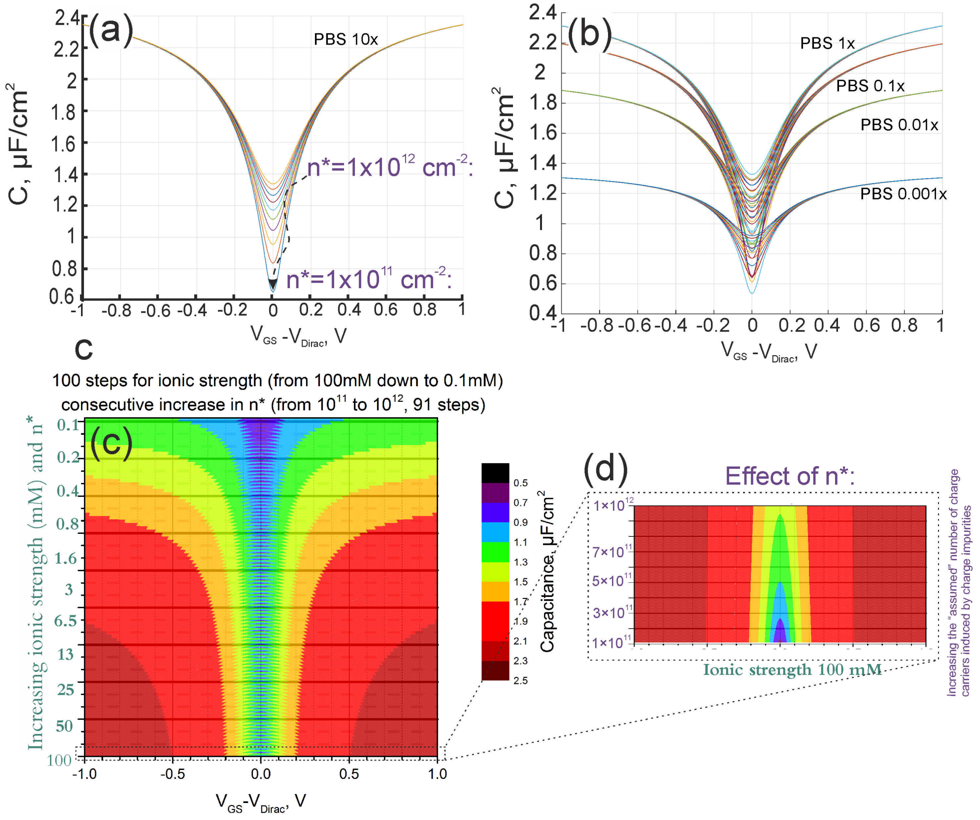

Figure 2.7: (a) Basic model of the interface capacitance for PBS 10x ($\approx$ 1.5 M), varying n^* from $1{\times}10^{11}$ cm^{-2} to $1{\times}10^{12}$ cm^{-2} with 10 steps. (b) Basic model of the interface capacitance for PBS 1×and below while varying n^* from $1{\times}10^{11}$ cm^{-2}to $1{\times}10^{12}$ cm^{-2}with 10 steps each. (c) The detailed color plot for changes in capacitance with varied ionic strength (from 0.1 to 100 mM) and the n^* changed between $1{\times}10^{11}$ cm^{-2} and $1{\times}10^{12}$ cm^{-2} with 91 steps. In (d) is given a zoom in into one data set, when ionic strength is set to 100 mM, and n^* is changed.

Since the charge carrier concentration is proportional to the applied gate potential ($n_G \propto V_{GS}$), the quantum capacitance is linearly dependent on the applied potential ($V_{GS} - V_{Dirac}$), and the dependency is plotted in Figures 2.7. n^*, on the other hand, is the number of charge carriers induced by charge impurities, and varies from 1×10^{11} to 1×10^{12} cm^{-2}. As seen from the Figure 2.7, the interface capacitance slightly influenced by the n^*, but only in the region close to Dirac point, while the influence can be neglected further from the point ($|V_{GS} - V_{Dirac}| > 100mV$). Further calculations of the interface capacitance and use of the model to the real experiment data are given in the Chapter 5.

A correct modeling of the total interface capacitance can be calculated by the following equation:

$$\frac{1}{C_{total}} = \frac{1}{C_{EDL}} + \frac{1}{C_{airgap}} + \frac{1}{C_Q} \tag{2.14}$$

Knowing the actual interface capacitance is important to correct estimation of GFET's parameters, such as mobility and transconductance. The basic plot of such capacitances is dependent on electrolyte's ionic strength and are plotted in the Figure 2.6b. A more comprehensive analysis of the capacitance with n^* taken into consideration is given in the Figure 2.7. The capacitance values are used to calculate the mobility values of the GFETs, reported in Chapter 5.

2.3 Electrical Double Layer

Classically, EDL is the ionic arrangement at and near the surface of an object inserted into an electrolyte [89]. In this sense, the first layer is typically a layer of ions, specifically adsorbed on the surface, while the second layer is composed of the oppositely charged ions, attracted by the Coulomb force. These screen the charge of the object. The second layer can not be considered static, and should be described as rather diffusive.

In 1853, Helmholtz proposed a simple double layer theory, suggesting a simple ion separation and therefore the EDL can be modeled as a parallel-plate capacitor [89, 90]:

$$C = \epsilon_0 \epsilon_r \frac{A}{d} \tag{2.15}$$

where ϵ_0 is the dielectric constant, ϵ_r is the relative dielectric permittivity of the solvent, A is the area of an electrode and d is the distance.

In 1910, L.G. Gouy and in 1913 D.L. Chapman observed that this capacitance is not constant, and an electrolyte is not an ideal conductor [91, 92]. They developed the Helmholtz model further by considering the thermal movement of the ions and proposed a diffuse layer of ions at a charged surface (see Figure 2.8). The local ion concentration depends on the potential, Φ, at a distance d from a surface with a potential Φ_0:

$$\Phi = \Phi_0 \times \exp\left(\frac{-d}{\lambda_D}\right) \tag{2.16}$$

where λ_D is the Debye length, and can be calculated as

$$\lambda_D = \sqrt{\frac{\epsilon_0 \epsilon_r k_B T}{2 n_0 z^2 e_0^2}} \tag{2.17}$$

where n_0 is the bulk concentration of ions in the electrolyte, e_0 is the elementary charge, z is the ion charge, k_B is the Boltzmann constant, and T is temperature. For $z = 1$, the approximate λ_D values, calculated for electrolyte concentrations of 1×10^{-3}M, 1×10^{-5}M, and 1×10^{-7}M are 10 nm, 100 nm, and 1 µm, respectively.

As described above, and schematically illustrated in the Figure 2.8, the excess charge at the solution side has an opposite sign, but equal value to that of the solid surface. The ions, therefore are electrostatically attracted to the electrode interface, but the attraction is counteracted by the random thermal motion that aims to equalize the concentration throughout the solution (see Figure 2.8). The overall equilibrium can be easily computed via the linear Poisson-Boltzmann equation [89]:

$$\frac{\mathrm{d}^2\phi}{\mathrm{d}x^2} = \frac{\phi(x)}{\lambda_D^2} \tag{2.18}$$

which, in turn is calculated from the following equations and assumptions:

- Poisson equation: $\frac{\mathrm{d}^2\phi}{\mathrm{d}x^2} = -\frac{\rho(x)}{\epsilon_r \epsilon_0}$;
- $\rho(x) = z e_0 (n_+(x) - n_-(x))$ is the charge density in the electrolyte;
- $n_{+/-}$ are the densities of cations and anions and can be calculated by Boltzmann statistics (considering n_0 as the bulk density and k_B as the Boltzmann constant) as follows: $n_{(+/-)} = n_0 \cdot \exp\left((-/+)\frac{z e_0 \phi(x)}{k_B T}\right)$;
- $\frac{z e_0 \phi(x)}{k_B T} \gg 1$.

Solving the simplified Poisson-Boltzmann equation (2.18) results in the following equation for the Gouy-Chapman capacity:

$$C_{GC} = \frac{\epsilon_r \epsilon_0}{\lambda_D} \cdot \cosh\left(\frac{z e_0 \phi(0)}{2 k_B T}\right) \tag{2.19}$$

However, in the Gouy-Chapman model all ions are considered as point charges, and can approach the surface infinitely close. This assumption leads to a major drawback that leads to unlimited increase of capacitance at high ionic concentrations. This has never been verified experimentally, and the model was further improved by O. Stern in 1924 [93]. Stern introduced that ions cannot approach the electrode's surface closer than their ionic radius. The distance of the closest possible approach is called Outer Helmholtz Plane (OHP) (see Figure 2.8).

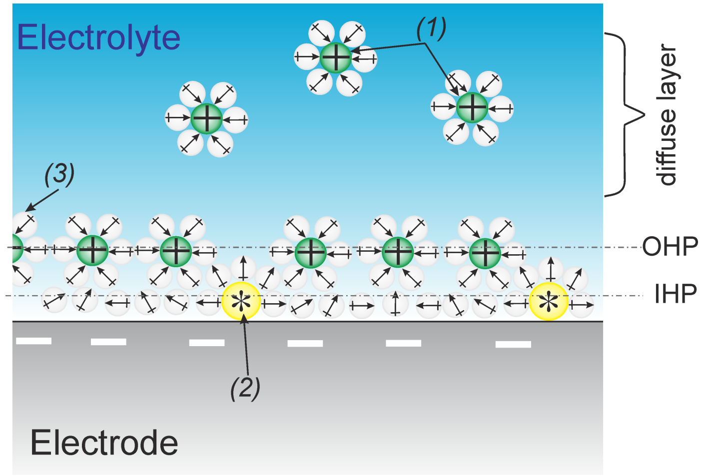

Figure 2.8: The schematics of the electrical double layer arrangement. IHP and OHP stand for Inner and Outer Helmholtz Plane, respectively. In green are marked the hydrated ions, also marked as *(1)* in the figure; in yellow are shown specifically adsorbed ions, also marked as *(2)* in the figure. The gray spheres *(3)* represent water molecules, and arrows the direction of their dipoles. Adapted from [94].

2.4 Electrophysiology of Cells and Action Potentials

Electrophysiology is the study of the behavior and properties of electrically active biological cells and tissues. It consists of measurements of either voltage or current changes of ion channels, individual cells, or even whole organs (e.g. heart). As a part of neuroscience the important component is the measurements of neuronal electrical activities, especially their action potentials (AP). Action potential is an event in which cell's membrane potential quickly raises and falls. Such APs can propagate through cellular layers and are responsible for a large variety of organism's functions: sensory processing, thinking, muscle control, cardiac function, etc.

As known, all eukaryotic cells (including cardiac and neuronal) are enclosed by a membrane, made of bilayer phospholipid molecules. The membrane has an approximate thickness of 5 nm, and in general is a perfect insulator [95]. However, in the case of such electroactive cells like neurons or cardiac muscle, the membrane incorporates some ion-selective channels and pumps, allowing ions to flow inside/outside of the cell's cytosol. Ion channels are specific proteins, which form pores inside the membrane, allowing ions to pass through. This is a passive transport, since no energy is consumed for the process. There is a variety of factors which can influence the ion channel's conductivity, and therefore cause the changes in the further ionic concentration, and consequently cause repolarization of the membrane.

The equilibrium potential (E_X) for a single ion species (X) can be calculated via the Nernst equation:

$$E_X = \frac{RT}{zF} \cdot \ln\left(\frac{[X]_{ext}}{[X]_{int}}\right) \tag{2.20}$$

where T is the temperature, $F = 96.4 \cdot 10^3$ C/mol is the Faraday constant, $R = 8.31$ $\mathrm{J \cdot mol^{-1} K^{-1}}$ is the gas constant, z is the ions valence, $[X]_{ext}$ and $[X]_{int}$ are the external and internal concentrations of species X, respectively. If permeabilities P^X of the species X are taken into account, the overall membrane potential can be calculated using the following, so-called *Goldman-Hodgkin-Katz equation*:

$$E_m = \frac{RT}{zF} \cdot ln\left(\frac{P^{K^+} \cdot [K^+]_{ext} + P^{Na^+} \cdot [Na^+]_{ext} + P^{Cl^-} \cdot [Cl^-]_{ext}}{P^{K^+} \cdot [K^+]_{int} + P^{Na^+} \cdot [Na^+]_{int} + P^{Cl^-} \cdot [Cl^-]_{int}}\right) \tag{2.21}$$

As the intra- and extra-cellular surrounding is filled with electrolyte with different ionic compositions and concentrations (see Table 2.1), a potential difference, so-called *membrane potential*, E_m, is established [95, 96]. Typically the value of E_m is in the range between -60 mV and -90 mV. While at the equilibrium state, the reciprocity of diffusion, pumping, leakage, and other interactions results in the equilibrium state and so-called *resting potential*. Some of the channels are voltage-activated, providing interesting aspects for further cellular stimulations. Ion pumps, on the other hand, require energy (ATP to ADP conversion) to move the ions against the electrochemical gradient.

Table 2.1: The intracellular and extracellular concentrations of ions for cardiac muscle and neuronal cells [95, 96].

	Ion concentrations	
Ion species	Intracellular (mM)	Extracellular (mM)
K^+	100-155	5
Na^+	8-30	145
Cl^-	4-30	120
Ca^{2+}	10^{-4}	2
HCO_3^-	8-15	25
other anions	155	—

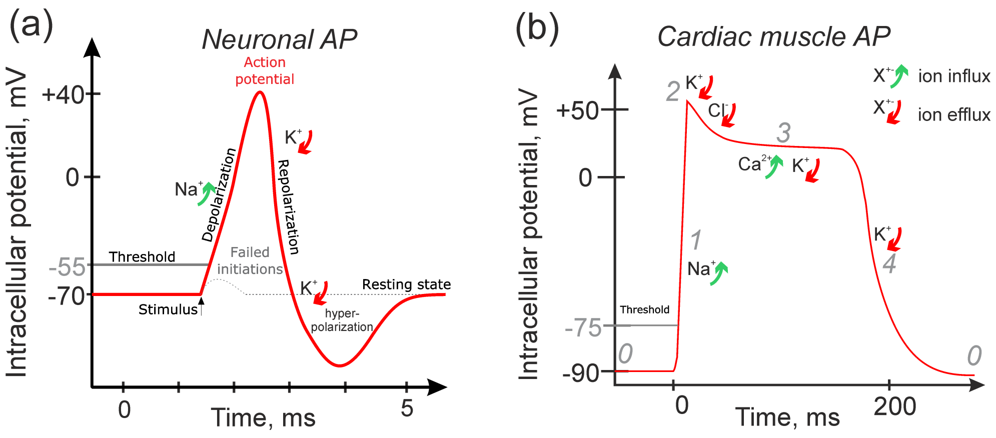

Figure 2.9: The typical action potentials of a neuronal cell (a) and a cardiac muscle cell (b). The neuronal firing (of APs) is mostly related to the influx Na^+ ions and the corresponding efflux of the K^+ ions along the chemical gradient, and the whole duration of an AP is short: less than 5 milliseconds in total. In contrast to that, the signal decay in the cardiac muscle cells is related to the slow Ca^{2+} channels, and the total duration of their APs tens of milliseconds with a prolonged repolarization period, up to 200 ms.

If an external stimulus is applied to the membrane of an electrogenic cell, the cell may produce an action potential. The external stimulus can be of different kind: e.g. intracellular potential induced by a patch-clamp (see Section 2.4.1). The neuronal and cardiac APs are shown in Figure 2.9. When in equilibrium, the cell is at its resting potential, which is usually around -70 mV for neuronal cells and -90 mV for cardiac muscle cells. When an external stimulus is applied, it can temporarily depolarize the membrane. If the depolarization potential reaches some threshold value, the fast sodium channels open, and the Na^+ ions flow into the cell due to the chemical gradient. The threshold potential is in the range of -50±5 mV for neuronal cells and -75 mV for cardiac muscle cells [95,96]. If the initial depolarization is below the threshold, no AP is formed (see gray line in Figure 2.9a). The sodium ion flow is rapid in both neuronal and cardiac AP, and consequently changes the the membrane potential to rise rapidly up to $+40 \pm 10$ mV. The influx of sodium ions increases the concentration of positively charged cations inside the cell. By the moment the sodium ion flow has reached its maximum, the potassium ion channels are still open and continue leaving the cells. The efflux of potassium ions, in the case of neuronal cells, results in membrane hyperpolarization, when the membrane potential can reach even lower values than the resting potential. The principle of a cardiac muscle AP is similar, and is shown in details in Figure 2.9b. While the initial depolarization (due to Na^+ ions, see (1) in Figure 2.9b) in the range of several milliseconds. The first repolarization step is due to first potassium efflux (see (2) in Figure 2.9b), which is followed by a characteristic plateau (see (3) in Figure 2.9b) caused by the impact of slow Ca^{2+} channels, keeping the membrane potential near its excited potential for as long as 200 ms. The final repolarization is as well due to efflux of potassium ions.

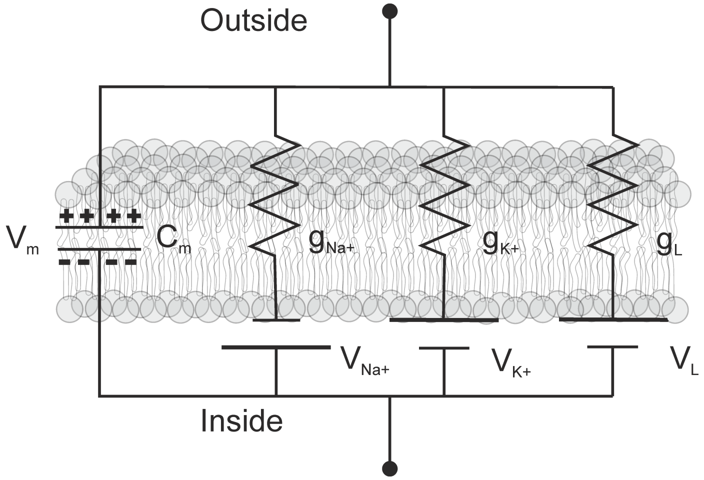

Figure 2.10: The ideal electric circuit of the membrane, according to Hodgkin-Huxley [97]. It consists of a single capacitive element, representing the membrane capacitance and three sources of ionic flow (with their corresponding conductances g_X): Na^+ current flow outside-to-inside, K^- and leakage currents (mainly Cl^- ions) flowing inside-to-outside. The membrane potential is depicted as battery since there is a built-up potential due to differences in ionic concentrations inside/outside of the cell and the membrane serves as the separator.

Hodgkin and Huxley were the first ones to systematically study the origin of action potential, and they ended up with an equivalent circuit model which describes the membrane potential, and can help in further understanding of the signal recording [97]. The Hodgkin-Huxley model represents the electrical activity through the membrane as a network of individual pathways (see Figure 2.10). The current through the membrane, according to the model, can be changed either via charging the membrane capacitance (C_m) or by movements of ions through the ion-specific channels (represented as resistances), which are in parallel to the capacitance. The ionic current is divided into the sodium and potassium components (I_{Na} and I_K), with an additional leakage current (I_L, mainly consisting of Cl ions). Each individual ionic current can be determined via the following equations:

$$\begin{aligned} I_{Na} &= g_{Na}(E - E_{Na}); \\ I_K &= g_K(E - E_K); \\ I_L &= g_L(E - E_L). \end{aligned} \tag{2.22}$$

where $E_{Na,K}$ are the corresponding equilibrium potentials, and E_L is the potential at which the leakage current is zero. The g_{Na} and g_K are the conductances of the ionic flow, which vary in time and with membrane potential, while other components are constant.

Therefore, the total current through the membrane can be simplified to the following:

$$I_m = C_m \frac{dV}{dt} + I_{Na} + I_K + I_L \tag{2.23}$$

where V is the difference of the membrane potential compared to its resting potential, C_m is the membrane capacitance (per unit area), and t is time.

2.4.1 Intracellular Electrophysiology

Intracellular electrophysiology methods, such as the patch clamp technique, are still the gold standard in providing the background/reference information about electrical activity of the cells [1, 2]. There are four kinds of the patch clamp technique, but since we are interested in action potentials of an entire cell, below described is so-called “whole-cell” patch clamp method. In this method, a glass micro-pipette is driven close to the cell’s body (Figure 2.11a), and an underpressure/suction is applied, causing the membrane to bend inside (Figure 2.11b) and further break inside the pipette (Figure 2.11c). Since the pipette is filled with an *intracellular patch solution* (I-patch), the cell does not “feel” disturbed and behaves normally for the time of measurements. However, upon retracting the pipette, the measured cell will be stressed or can even die. Nevertheless, for the time the pipette is connected to a cell, every intracellular activity of the cell can be measured. Further one can apply the voltage/current through the pipette in order to stimulate the cell intracellularly.

The signal-to-noise ration (SNR) of this method is usually large. However, the method is invasive, therefore not fully suitable for long-term and multiple measurements from one neuron, for example. Moreover, a simultaneous recording from multiple neurons/cells is difficult and almost impossible. Therefore, the non-invasive techniques has been established, and mostly implemented are the simple MEA or FET approaches.

2.4.2 Extracellular Electrophysiology

It is of high importance to measure the changes of membrane potential in a non-invasive, stable, yet high SNR way. Many techniques have been developed, such as using voltage-sensitive dyes, ion-sensitive FETs, or light addressable potentiometric sensors (LAPS). However, the two most commonly used and the most developed ones are multielectrode arrays (MEAs) and field effect transistors (FETs) [99].

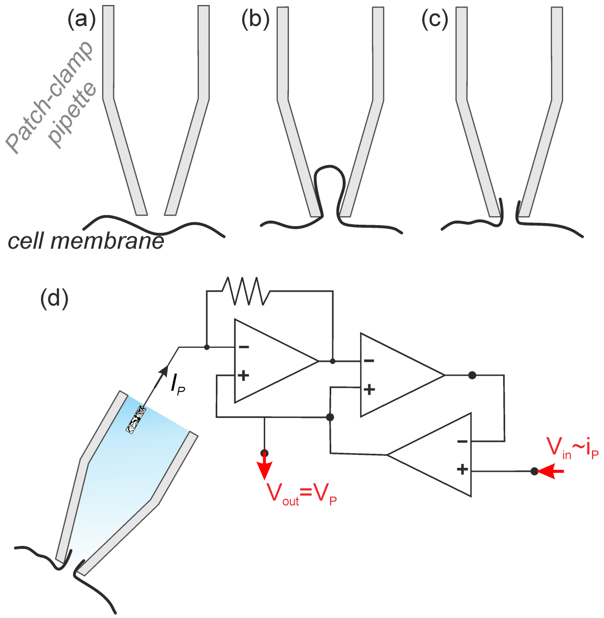

Figure 2.11: A simplified schematics of the patch clamp method, commonly used for direct probing of the intracellular signal. The dynamics of the process is following: (a) the glass micropipette is driven close to the cell (under a microscope), then an under-pressure is applied, forcing the cellular membrane to bend inside the pipette (b). Following an application of under-pressure or an external voltage brakes the cell membrane (locally), however still being intact with the I-patch solution inside the pipette (c). In (d) is shown an electrical diagram of a current clamp measurement . The figure is partially adapted from [98].

2.4.2.1 Point Contact (neuronal) Model

The interface between a cell and a sensor (electrode or transistor) can be explained via the point contact model [7, 31]. The model states that the electrolyte fills the cleft between a cell and a sensor. The contact between cell and electrode is simplified to one single point in the cleft with the junction potential, V_J. The cleft itself is further represented by a seal resistance, R_S. The membrane's permeability and conductance is modeled with the above-explained Hodgkin-Huxley model. A schematic view of the point contact model is given in Figure 2.12. An electrode/transistor in the model is seen as a capacitor (C_E) in parallel with a resistor (R_E), which are connected to a recording unit on one side and to the cleft (between cell and electrode) on the other side. The cellular membrane, is separated into two components, *junction membrane* and *free membrane*, both of which can be modeled via the Hodgkin-Huxley elements, depicted as HH_{JM} and HH_{FM} respectively. The cleft, represented by g_J, provides a path for a current to flow away, instead of being detected by the electrode. Therefore it is possible that the shape of the action potentials, recorded by the electrodes is non-ideal and may lose features correlated with specific ionic flows.

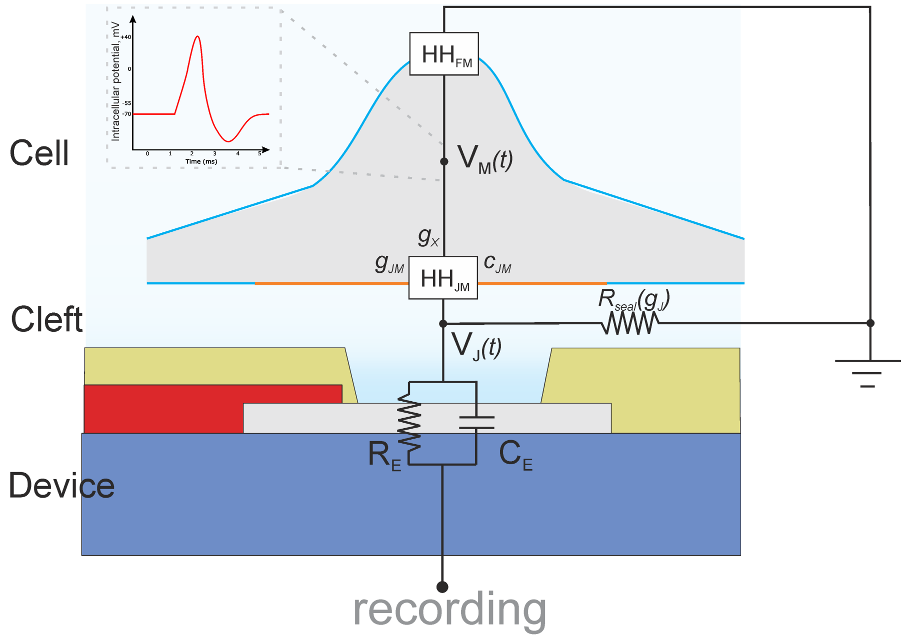

Figure 2.12: The simplified point contact model. The cell (gray) can be modeled by two HH elements, considering free membrane (not attached or in contact with the device/electrode) and junction membrane (the one in contact with the electrode). The cleft of the junction is filled with electrolyte and is modeled via the junction's conductivity (g_J) or resistance (R_{seal}). The electrode itself is modeled as a combination of resistance and capacitance in parallel. Adapted from [13, 31].

The relation between the junction potential and the intracellular potential can be solved via *Kirchhoff's law*:

$$\mathrm{g}_J V_J = \mathrm{c}_{JM}\frac{\mathrm{d}V_M}{\mathrm{d}t} + \mathrm{g}_{JM} V_M + \sum_X \mathrm{g}_X (V_M - E_X) \tag{2.24}$$

where the first term on the left is ohmic current in the junction; first and second terms on the right side are capacitive and ohmic currents through the junction membrane correspondingly, and the third term on the right side is related to the current caused by specific ionic flows. where X is ion species, g_X is its conductance, as introduced in equation 2.22, g_J is junction conductance. c_{JM} and g_{JM} are the junction membrane capacitance and conductance correspondingly. The V_M and V_J are, as introduced above; time dependent they are given as $V_M(t)$ and $V_J(t)$.

However, in order to simplify the explanations, we split the model into three, accordingly to Fromherz [100]:

A. Capacitive response. If ionic current flow in the junction membrane is completely neglected, the relation between the junction potential and the intracellular potential can be simplified from equation 2.24 to the following:

$$V_J = \mathrm{c}_{JM}\frac{1}{\mathrm{g}_J}\frac{\mathrm{d}V_M}{\mathrm{d}t} \tag{2.25}$$

which means that in this case the extracellular potential is proportional to the first derivative of the intracellular voltage. Such kinds of extracellularly recorded APs are very typical and can be found, for example in Chapters 5 and 6 of this thesis.

B. Ohmic response. If no voltage-gated ion channels are present in the the junction membrane, and the ohmic conductance (leakage currents) dominates over over the capacitive response, the equation 2.24 can be simplified to the following:

$$V_J(t) \approx \frac{1}{\mathrm{g}_J}\mathrm{g}_{JM}V_M(t) \tag{2.26}$$

which means that in this case the extracellular potential is directly proportional to the intracellular voltage. Such kinds of APs can also be usually found in the recording, see for example in Chapters 5 and 6 of this thesis.

C. Mixed response. This is the most realistic and most common response, where both capacitive and ohmic parts contribute to the final junction potential. The strength of the response is given by the ionic currents, scaled by the seal conductances. Such arrangements results in a variety of waveforms, $V_J(t)$ could have. This is also experimentally observed in this thesis as shown in Chapters 5 and 6.

2.4.2.2 Gap Junction (HL-1) Model

The general explanation of the cardiac APs has been given in the previous Section 2.4. If a single cardiac-line cell is placed on top of an electrode, the coupling model will be exactly similar to the one presented above. Although, in contrary to neuronal cells, HL-1 cells, upon maturation, are grown into a continuous layer, which *"beats"* continuously and the electrical signals are propagated through the layer via formed gap junctions. Gap junctions are a kind of electrical synapses, that directly connected to each other, and the cytoplasms of the (neighboring) cells are connected by intracellular channels. This allows direct transmission of the electrical ionic currents and other species with almost no transmission delay.

Moreover, the mature HL-1 culture forms specific pacemaker cells. The mechanism of the pacemaker cells is similar to those of cardiac pacemaker cells located in the sinusoidal node

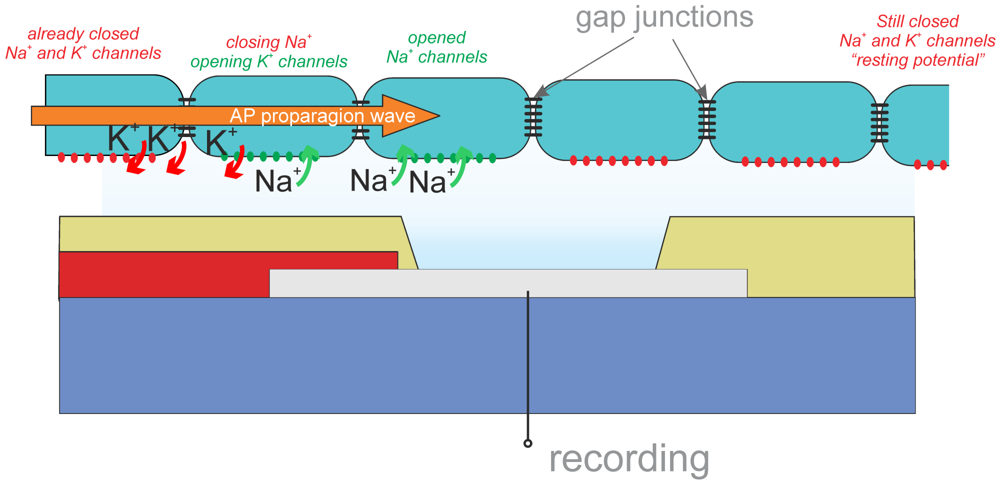

Figure 2.13: The sketch of the "gap junction" model, which is valid for the HL-1 layer. A signal is propagating through it via the gap junctions. When a neighboring cell is excited, the induced influx of Na^+ ions, consequently causes the next cell to fire an AP, resulting in a wave-like signal propagation. Adapted from [101, 102].

of a heart. There, from the membrane potential of -60 mV, Na^+ channels open, producing a small depolarizing influx current, leading to further opening of the transient "T-type" Ca^{2+} channels, further depolarizing the cell. When reaching approximately -40 mV, the long-lasting "L-type" Ca^{2+} channels open and last until the AP maximum is reached (at $+45 \pm 5$ mV). The further depolarization slope of the pacemaker cells is much more gradual even compared to other, "normal" cardiac cells, since it is dominated by opening of L-type Ca^{2+} channels and closing of T-type Ca^{2+} and K^+. The final repolarization happens due to efflux of K^+ ions (L-type Ca^{2+} channels closed), leading to an extra hyperpolarization, and consequently to activation of the pacemaker channels, and starting the cycle again [103].

This continuous self-inhibition of the action potential at the pacemaker cell, together with ability of signal propagation throughout entire cellular network explains the successiveness of the HL-1 action potentials, typically recorded by both GFETs (see Chapter 5) and GMEAs (see Chapter 6).

The model of the signal propagation is schematically shown in Figure 2.13. The depolarization wave propagates laterally, through gap junctions to trigger an AP in the neighboring cell. When the cell reaches its threshold, voltage-gated ion channels open, inducing influx/efflux of Ca^{2+} and K^+ ions [101]. The corresponding change in membrane potential of this cell, consequently triggers an AP in the next cell, etc.

Chapter 3

Materials and Methods

3.1 CVD Growth of Graphene

Chemical vapor deposition (CVD) is a common method to produce thin layers of materials from gaseous reactants as a result of a chemical reaction. There are different CVD reaction types, such as pyrolysis, reduction, etc. CVD growth of graphene was first reported in 2006 [74] and further evolved into a large-scale and high-quality process [104, 105]. In general, the CVD growth of graphene is a cheap, versatile, and scalable process, which is compatible with CMOS technology, and of comparable quality to the exfoliation process.

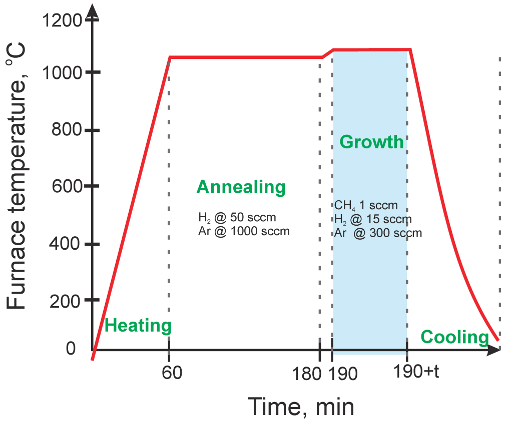

Figure 3.1: Schematics of the CVD growth recipe.

Tha graphene, used in this work, was produced by collaborators in Shanghai Institute of Microsystem and Information Technology [71]. The graphene was CVD-grown on 25 µm thick copper foil for 30 minutes at 1050°C-1070°C and methane gas was used as a carbon source. The process is performed in a quartz tube furnace in presence of Ar/H_2/CH_4 gas mixture (300 sccm, 15 sccm, and 0.5-1.0 sccm respectively) [71]. The overall schematics of the growth is shown in Figure 3.1. Prior to the growth, the copper foils were thoroughly cleaned in hydrogen chloride followed by subsequent acetone and isopropanol rinses. Two hours of annealing at a temperature below the melting point (of copper) in H_2/Ar atmosphere (50 sccm and 1000 sccm, respectively) is performed in the furnace prior to the growth.

The Raman spectra are taken from the CVD grown material and reveal a defect-free continuous monolayer of CVD graphene (See Figure 3.2 for details).

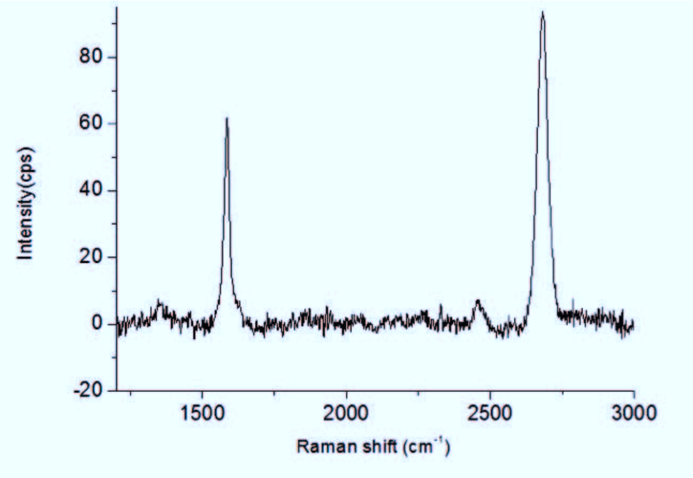

Figure 3.2: Raman spectra of the used graphene.

3.2 Wet Transfer

A thin layer of PMMA (300-500 nm) was spin-coated on top of the graphene-on-copper in order to serve as a support polymer for further transfer. After 5-10 minutes annealing at the glass transition temperature of the PMMA (150°C), the PMMA/graphene/Cu stack was ready for transfer. However, the CVD growth of materials happens on both sides of the copper foil, therefore in order to get more reliable and cleaner material, the backside of the copper foil was exposed to oxygen plasma (0.8 mbar, 100W, 5 min). After that, the PMMA/graphene/Cu stack is moved into copper etchant solution (0.1 M $(NH_4)_2S_2O_8$) for 24 hours and subsequently into several DI water washing cascades. After that, the PMMA/graphene stack can be picked up, or "fished out" by a target substrate (see Figure 3.3).

When the PMMA/graphene stack is fished by the target substrate, it is left for 24 hours under ambient conditions to slowly dry out. After that, in order to improve the graphene-to-substrate adhesion, and re-flow the PMMA, the target substrate with graphene is annealed

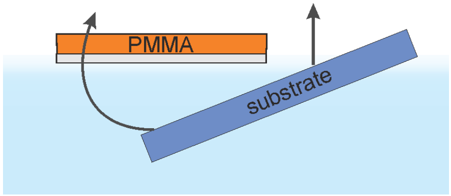

Figure 3.3: Schematics of the "fishing" procedure. PMMA/graphene (Dark orange/silver) stack is floating on the surface of DI water, while the substrate (dark blue) is used to directly pick-up the material stack, resulting in graphene being in direct contact with the substrate.

at 160°C for 10 minutes [106]. When cooled, the PMMA is finally removed with acetone (one hour in 50°C acetone followed by 12 hours in cold acetone), washed with isopropanol and DI water, and dried under nitrogen flow.

However, in order to fabricate the devices on a new method was developed. The so-called high-throughput method is described in Chapter 4.

3.3 Electrical Characterization

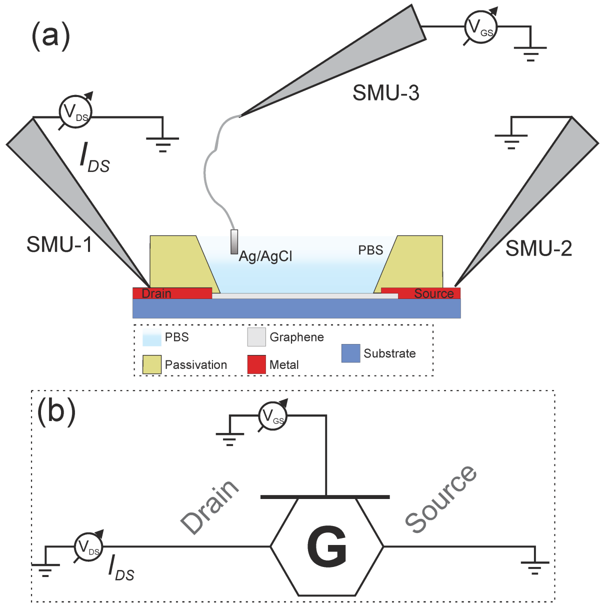

Figure 3.4: (a) Schematic representation of GFET characterization via a Keithley 4200 SCS probe-station. Three SMUs are used to connect source, drain and gate. (b) An equivalent circuit diagram of the measurements. The GFET is shown as a combination of classical transistor representation with hexagonal shape.

3.3.1 I–V Characterization

As soon as fabricated and encapsulated, the devices are characterized by means of a Keithley 4200 SCS probe station. The drain – source potential (V_{DS}) is set to 50 mV or 100 mV, whereas the gate potential (V_{GS}) is swept against a Ag/AgCl pellet electrode from 0 to 800 mV. A phosphate-buffered saline (PBS) solution of ≈160 mM salt concentration, and pH 7.4, was used as electrolyte to be as close to the physiological conditions as possible. As shown in Figure 3.4, three Keithley Source Measure Units (SMUs) are used to connect to a source, drain, and a gate of a GFET. While the source and drain connection is done by needles contacting the contact pads (under a microscope), the third SMU is connected to a Ag/AgCl pellet electrode, which is dipped into the PBS on top of the chip.

3.3.2 Electrical Impedance Spectroscopy

Electrical impedance spectroscopy of GMEAs was performed on a VSP–300 multichannel potentiostat (BioLogic Science Instruments). The spectra were taken using graphene as a working electrode, and a Ag/AgCl pellet as a reference electrode in PBS solution. A 10 mV AC potential was applied and a frequency range between 1 Hz and 1 MHz was scanned.

3.3.3 Noise Characterization

The noise spectra are registered, using a measurement system developed in-house and the Dynamic Signal Analyzer HP 35670A, in the range from 1 Hz to 100 kHz. The intrinsic input–referred thermal noises of the preamplifier and ITHACO amplifier were measured as 2×10^{-18} $\mathrm{V^2Hz^{-1}}$ and 2×10^{-17} $\mathrm{V^2Hz^{-1}}$, respectively [107].

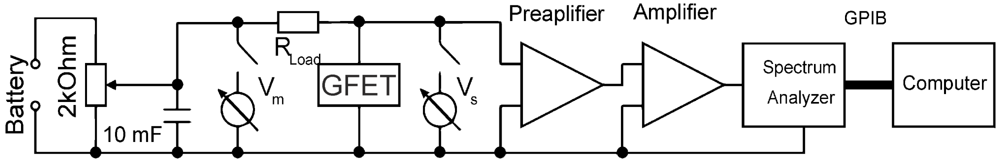

Figure 3.5: Circuit diagram of the noise measurement set-up.

3.3.4 BioMAS

Bioelectronic Mulifunctional Amplifier System (BioMAS) is the in-house developed set-up, aimed for versatile and standardized measurements from different kind devices on a single platform. The platform consists of one main amplifier (1×, 10×, or 100×) and a set of pre-amplifiers (headstages), see Figure 3.6 [108–110]. The headstages are customized to a

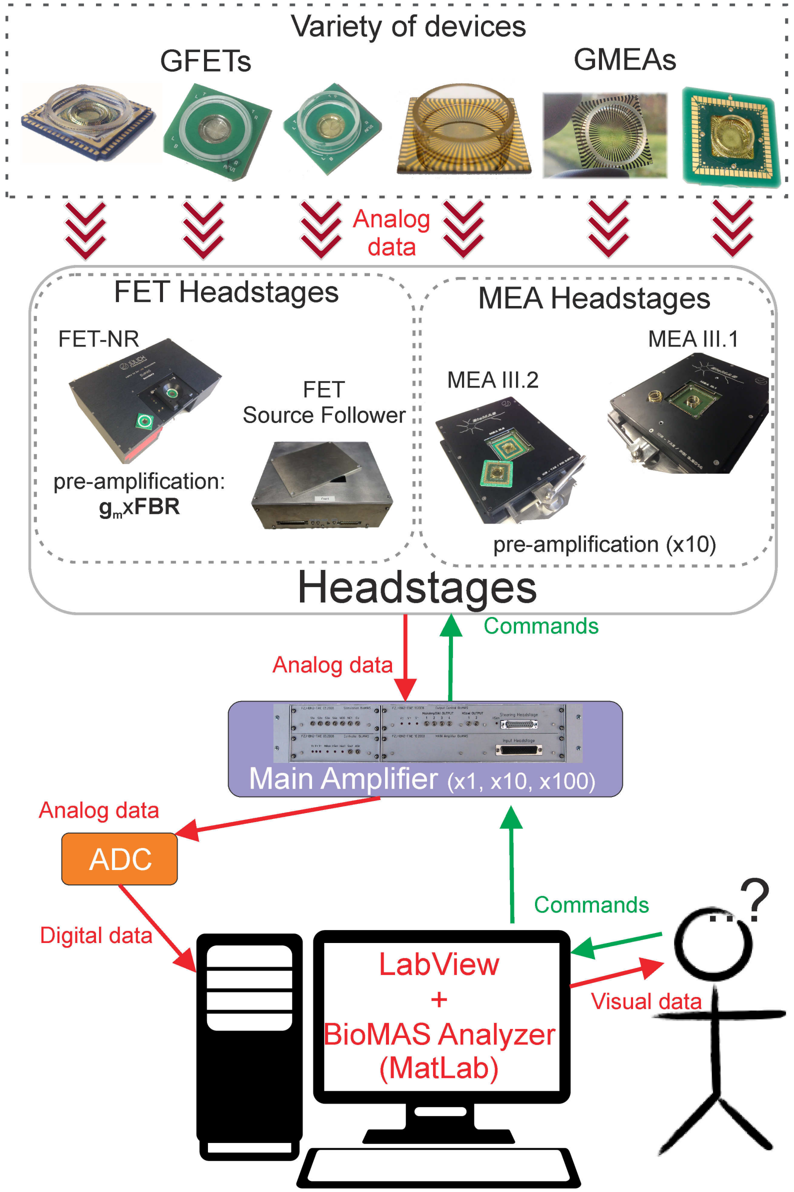

Figure 3.6: The overview of BioMAS hierarchy. The chips (top row) have specific I/Os and mappings. In general, this chips can be split in two parts: GFETs and GMEAs. The second part of the hierarchy is the headstage. The headstages are designed to work with a specific kind of chip (GFETs or GMEAs) and specific operation protocols. The third level is the main amplifier, which can communicate on one side with any headstage, and on the other side with a PC (via an ADC card and LabView based software). After analysis of the data, a user communicates/commands back to the chips via the reversed chain.

specific device types (GFET/GMEA) and geometrical layout of their I/Os, and comprise of a chip holder, operational amplifiers and some control circuits. The main amplifier, apart from amplifying, has other functions: it can generate stimulation signals and has some pre-installed anti-aliasing low-pass filters. The *analog to digital converter* (ADC) unit converts voltages, coming out from the main amplifier, to 16-bit digital values. The ADC has the sampling rate of 1.25×10^6 samples per second on a single channel or 750×10^3 samples per second, if distributed on all channels. The 64-electrode measurements therefore result in a typical sampling frequency of 10 kHz. Control of the measurements is done via LabVIEW-based software, developed in the institute, called *BioMAS NanoRibbon* for FET measurements and *BioMAS MEA* for MEA measurements. In the FET measurement unit, there are usually two modes:

1. Characterization.
2. Timeseries measurements.

Details and technicalities of the measurements are headstage dependent, and therefore given below.

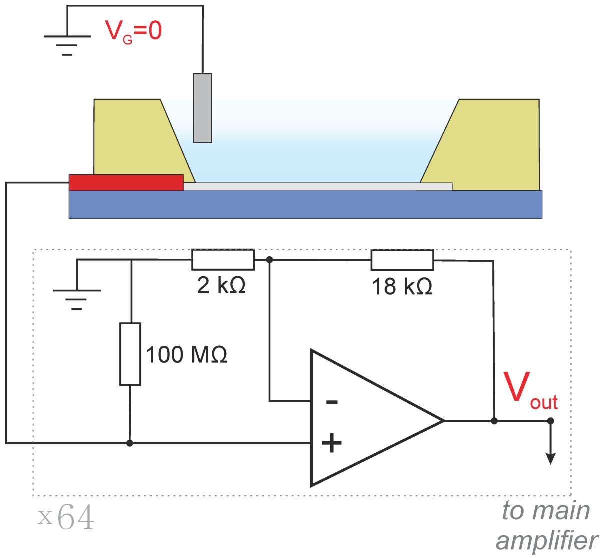

Figure 3.7: Simplified schematics of the MEA measurements. Each of the 64 electrodes is sampled separately but simultaneously and each signal is pre-amplified by a factor of ten.

3.3.4.1 MEA Headstages

MEA headstages are customized to have a 64-channel simultaneous read-out. The headstages perform a first amplification by a factor of 10 and have a socket to contact the

GMEA chip and a Ag/AgCl electrode. As discussed below, there are two kinds of GMEA chips used: one without any carrier, of a size 24×24 mm^2, and another one flip-chipped to a carrier (see Appendix C). MEA hadstage №III.1 is used for the first kind of chips and №III.2 for the later. The further main amplifier has two extra amplification stages (×10 each) and an anti-aliasing high-pass filter. In order to minimize any distortion of the measurements by the environment (mechanical/optical/electrical), the setup is placed in a custom-made Faraday cage on a vibration isolated table.

3.3.4.2 NR-FET headstage

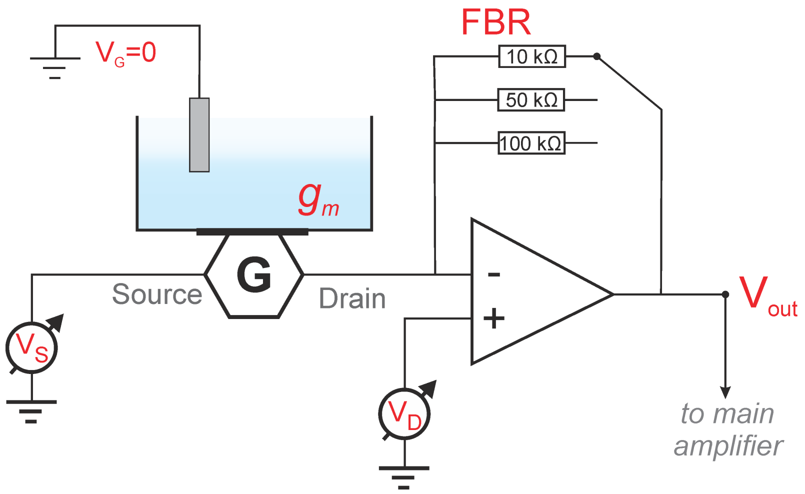

Figure 3.8: Simplified schematics of the NR-FET headstage and GFET measurements. Each of the GFETs has a source and drain potential set accordingly. Gate potential is kept at the ground level, and the V_{GS} potential is set via a special set of V_S and V_D. The 32 transistors are sampled separately but simultaneously. $FBR \times g_m$ represents the pre-amplification factor.

A simple circuit diagram of a FET headstage, so-called *NR-FET* headstage, is given in Figure 3.8. *NR* stands for NanoRibbon, as the headstage was historically made for the purpose of using Silicon-based nanoribbon transistors. Similar to the MEA headstages, the NR-FET headstage has also 64 channels, but due to the requirement of two electrodes per GFET, only 32 GFETs are designed per chip and measured simultaneously. The choice of the feedback resistance (FBR) and the actual transconductane (g$_m$) of the operational point (OP) used results in the pre-amplification factor:

$$V_{out} = V_{gate} \times g_m \times FBR \tag{3.1}$$

.

Afterwards, the signal is passed to the main amplifier, which consists of several post-amplification stages. The FBR should be set to a value in the same range to the actual graphene channel's resistance for the best signal transfer. Prior to the time series measurements, I-V curves are recorded for each GFET and further derived ($\Delta I_{DS}/\Delta V_{DS}$) in order to determine the highest transconductance point. The operational potentials (set of V_{DS} and V_{GS}, at which the transconductance is at its maximum) is further used for timeseries recordings.

3.3.4.3 Source Follower Headstage

A third kind of headstage was designed and made by Tianyu Qiu. The characterization and measurement principle of the headstage is completely different from the headstages presented above. In this case, a sinusoidal V_{GS} potential of a specific amplitude (V_{in}) is applied. At the same time, the V_{DS} potential and the amplitude (V_{out}) is measured and the amplification factor $A_V = V_{out}/V_{in}$ is calculated. The V_D, V_G, and V_S potentials are set semi-automatically in a desired region and the system finds the best amplification point. Like above, the operational point is further used for timeseries measurements, and the amplification factor is used to determine the actual gate potential fluctuations (ΔV_{DS}).

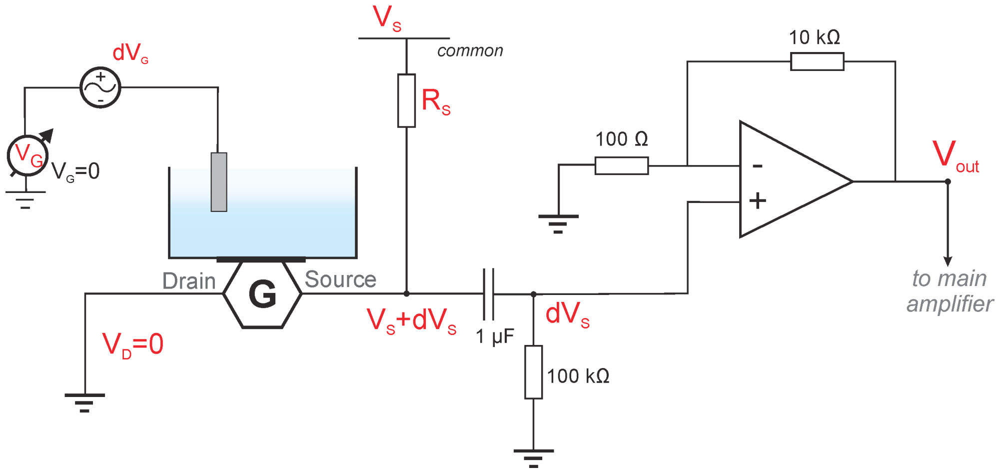

Figure 3.9: Schematics of the Source Follower FET measurements. Here, the V_G is kept at ground level, however there is a dV_G sine signal applied in the characterization step. While the V_S is applied via the R_S, there is a potential ($V_S + dV_S$) formed at the node. While the constant potential (V_S) can be subtracted by the RC element, the perturbations (dV_S) go through and are further amplified and recorded.

3.4 Cell Culture

3.4.1 Heart Tissue Preparation

The heart tissue is prepared by dissecting embryonic tissue E18 from a Wistar rat. The heart of an embryo is quickly isolated, washed in Hank's balanced salt solution (HBSS), then stored and measured in supplemented Claycomb medium (see Appendix H for details).

3.4.2 HL-1 Culture

For the culture of the adherent cardiomyocytes, a fibronectin and gelatin mixture (see Appendix H for details) was used as coating for the chips. The samples were coated for 1h at 37°C, then washed with PBS solution. Afterwards the cells were seeded with a specific concentration (typically 100-200 cells/mm^2) and were cultured for 3 to 4 days (depending on the initial concentration) in an incubator at 37°C and a humidified atmosphere of 5% CO_2 until the cells grow into a confluent and contracting layer, monitored using a light microscope. To guarantee a good cell growth, the supplemented Claycomb medium (see Appendix H for details) was exchanged on a daily basis. Two hours before the measurement the medium was exchanged.

The detailed protocol of the HL-1 culture is given in the Appendix H.

3.4.3 Neuronal Culture

The embryonic primary cortical neurons are isolated from an E18 Wistar rat [111]. Prior to culturing the cells on a chip, a glass ring is mounted to the chip to form a culture container and the surface of the chip is coated with GpECM mixture (see Appendix H for details) for improved cellular adhesion. The cells are diluted and plated on top of the chip with a density of ≈1500 cells/mm^2 and placed in an incubator (37°C and 5% CO_2). Neurobasal medium (see Appendix H for details) is exchanged two hours hour after the plating (100%), then twice per week and one day before the measurements (50%). The neurons were grown until at least 14 days *in vitro* (DIV) to be mature enough to produce action potentials that propagate through the whole network. In average, measurements were performed between DIV 16–25.

The experiments are done with the approval of the Landesumweltamt fur Natur, Umwelt und Verbraucherschutz Nordrhein–Westfalen, Recklinghausen, Germany, number 84-02.04.2015.A173.

The detailed protocol of the neuronal culture is given in the Appendix H.

3.4.4 Live-dead Imaging

Live-dead staining was performed using 1 μg/ml calcein-AM and 2 μM ethidium homodimer in supplemented cell growth medium to stain live and dead cells green and red, respectively. Cells and dyes were incubated for 15 minutes in a 37°C incubator or on a 37°C hotplate if performed after BioMAS measurements. Afterwards, the samples were observed using an Axio Imager Z1 microscope (Carl Zeiss).

3.4.5 Fixation and Imaging

In order to see the topography of the neuronal network, a high-resolution imaging is required. Scanning electron microscopy (SEM) is used in the work to observe outgrowth of the neurites on a surface. It is important to use a special preparation technique in order to image the biological specimens [27, 112]. After the culture, the samples are chemically fixed using a 3.2% glutaraldehyde solution (Sigma) in PBS (1x) for 30 minutes at room temperature. The following dehydration is performed in a series of ethanol washing steps (from 10% to 100% ethanol concentration). The samples are then stored in 100% ethanol until being dried using a critical point dryer (CPD) technique. In order to improve the charge flow, the samples are sputtered with approximately 10nm of platinum/iridium prior to the SEM imaging.

3.4.6 Chip Encapsulation

In order to perform cell cultures on the chips, the samples were encapsulated by attaching a glass ring with an outer diameter of 20 mm (17.8 mm inner diameter) on top of the 24×24 mm^2 chip using PDMS (10:1, Sylgard). The glass ring is 4 mm tall, which provides enough volume for the culture medium but is simultaneously small enough to allow the patch electrode to fit inside on a correct angle. In this way, the cell culture medium, and further the cells, are enclosed in a safe and leak–free environment. Prior to the cell culture, the chips were cleaned with a running DI water, then sterilized with 70% ethanol and transferred into the sterile bench. There, the chips were functionalized with cell–specific proteins (see Section 3.4). The details of chip encapsulation for different kinds of chips are given in Appendix C.

Chapter 4

High-throughput Graphene Transfer

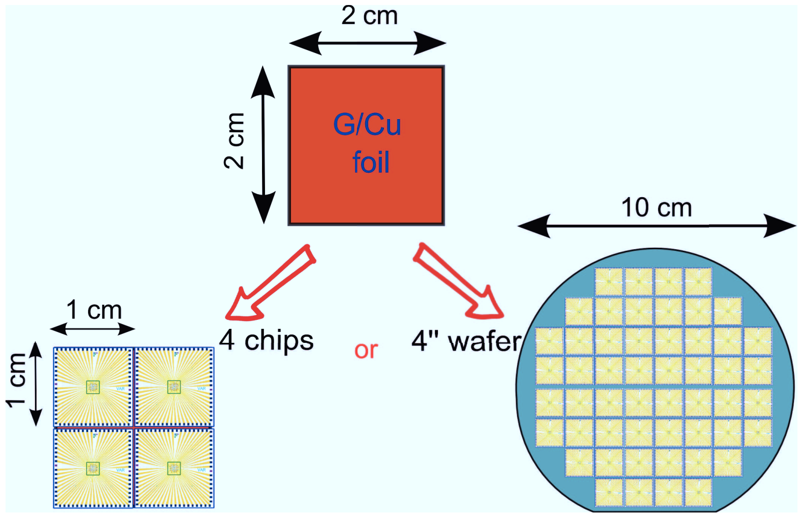

This Chapter was reproduced in part from the published work [55] with permission from Elsevier:

- **Dmitry Kireev**, Dario Sarik, Tianru Wu, Xiaoming Xie, Bernhard Wolfrum, and Andreas Offenhäusser. High throughput transfer technique: save your graphene. *Carbon* **2016**, 107, 319-324.

Research on graphene has been a rapidly growing field in the last decade [113, 114]. A vast amount of research has been conducted on its fabrication and growth [115]. Material qualities of graphene have been exploited very extensively: from low-dimensional and low-temperature physics [116] to studies of its biological [39, 40, 85] and environmental [117] properties. However, in order to fully exploit these properties, one must find an appropriate way of scaling up the graphene-based devices' production rate. This means that micromechanically exfoliated graphene, despite its advantages [116, 118], is not an appropriate material. The chemical vapor deposition (CVD) growth of single-layered graphene is the most common, cheap and scalable technique, as described in detail elsewhere [67, 73, 119, 120]. The CVD-grown graphene is the most applicable material in terms of quality, dimensions and growth parameters. State-of-the-art CVD-grown graphene displays grain sizes up to the millimeter-scale [121–123].

Nevertheless, transfer of the CVD graphene from a metal foil to a working substrate is still the most challenging and crucial step [106, 124, 125] of device production. The most commonly employed transfer procedure is wet–transfer, the so–called "fishing" transfer. However, it was shown that this method leaves many defects and residues [106, 125, 126], resulting in doping and damaging of graphene. A lot of research has been dedicated at modification of this method, e.g. extra annealing steps [127], modified RCA (Radio Corporation of America) cleaning [106], etc. Many different polymers are used as the support layer [125], some of which occasionally result in cleaner and less defective graphene. Nevertheless, still the most commonly used polymer for such a purpose is poly(methyl–methacrylate) (PMMA).

The fishing transfer is very easy for small pieces of graphene, up to one inch maximum. However, while scaling it up to 4–inch, 8–inch or even larger, several problems appear [128]. First, the large PMMA/graphene flake is very difficult to handle, and usually the transfer results in a large number of cracks and folds. Second, even if the large piece is transferred successfully, later, during the fabrication of devices, most of the graphene will be etched away. Just a small amount of the initially transferred graphene is actually used, therefore the used/wasted graphene ratio (UWR) is extremely small. This is an enormous amount of wasted material. One possible solution to the problem would be transferring the dozens of small pieces directly to the sites of interest. But this is impossible by the standard fishing protocol. Transferring even just two graphene pieces on one target substrate precisely on the spots of interest, while keeping precise distance between the pieces, would be impossible via the standard method. Additionally, while drying out, the small pieces tend to move (up to several millimeters) from the initial region, drawn by the tension forces of water.

With the high-throughput method we can transfer graphene precisely onto the spots that will be used. This is done via patterning the substrate into target regions where graphene

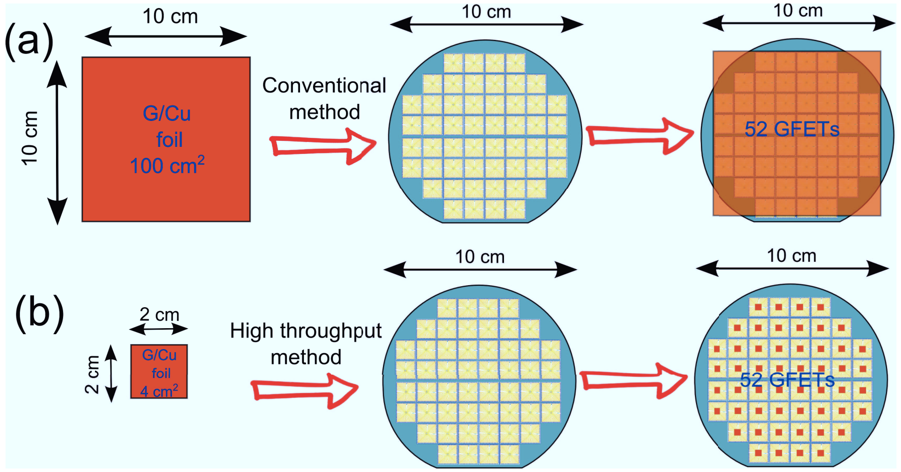

Figure 4.1: The advantage of the high-throughput method (b) compared to a conventional method (a). In a conventional method (a), a large graphene piece, of 100 cm^2 has to be used to fabricate one 4-inch wafer with devices. In the high-throughput method, small piece of the graphene foil, of 4cm^2 is enough to fabricate the same 4-inch wafer with 52 chips.

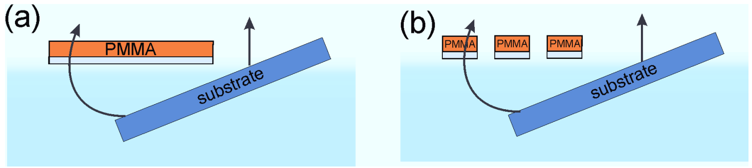

Figure 4.2: Schematics of the typical fishing wet transfer for one (a) flake. And problems with simultaneous fishing of more than 2 pieces at ones (b).

must be and transferring graphene only there, instead of transferring graphene on the whole wafer. The pattern transferred can be chosen according to the substrate design. Then, by means of the proposed method, the graphene pieces of specified size are transferred right into spots of interest. Moreover, the technique prevents the pieces to move away from their spots while drying. Such solution minimizes the material waste, as well as simplifies and accelerates the transfer process for large scale transfer. In our case, from one piece of 2cm×2cm graphene we can fabricate whole 4–inch wafer (with 52 chips), instead of the four chips possible transferring the same area of graphene with the fishing method (see Figure 4.1). We believe the technique can serve as a bridge towards more abundant and rational use of graphene in new state-of-the-art devices.

4.1 Set-up and Preparations

The transfer chamber. We have designed our transfer chamber for wafer sizes up to four inches. The chamber contains six alignment columns, a wafer chuck and pipe connections for pumping liquids through the system. The schematic of the chamber is illustrated in Figure 4.3. The chamber body itself has one main role: to hold the target wafer and align it with the mediator film.

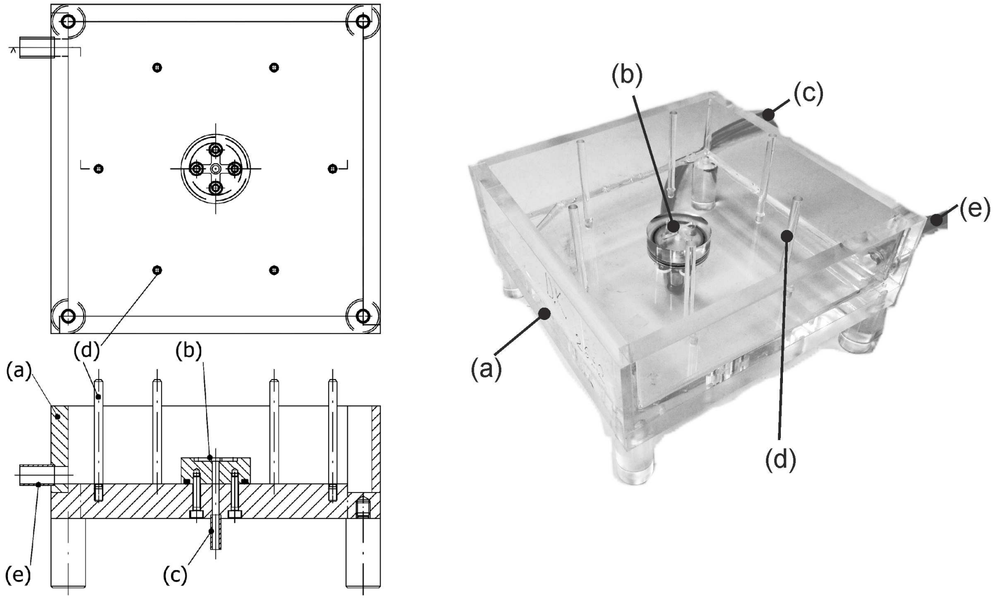

Figure 4.3: The design of our set-up: (a) main body, (b) wafer chuck, (c) vacuum pump outlet, (d) alignment columns, (e) liquid in/out.

Wafer design as a parameter. Knowing the wafer design, the amount of chips, and their position on the wafer, are the important parameters for determining the further transfer steps. For the case of GFETs fabrication, we have determined 52 spots on the 4–inch wafer, since there are 52 chips (Figure 4.4a). Each chip, 11×11 mm^2 in dimensions (Figure 4.4b) has the graphene only in the middle 2×2 mm^2 area (Figure 4.4c). These are the zones where graphene has to be transferred. Each of our chips, subsequently consists of an array of 32 graphene field effect transistors (GFETs) each with a graphene active area of just 20 to 400 μm^2 (Figure 4.4d).

Mediator film. The most important part of the set-up, the mediator film, is fabricated as an identical copy of the wafer design with openings in the aforementioned transfer zones (see Figure 4.5). Openings of an appropriate size are also made for the alignment columns. The thickness of our mediator film is 125 μm. Every modification of the wafer design that changes the locations of requiring graphene necessitates fabrication of a new mediator film.

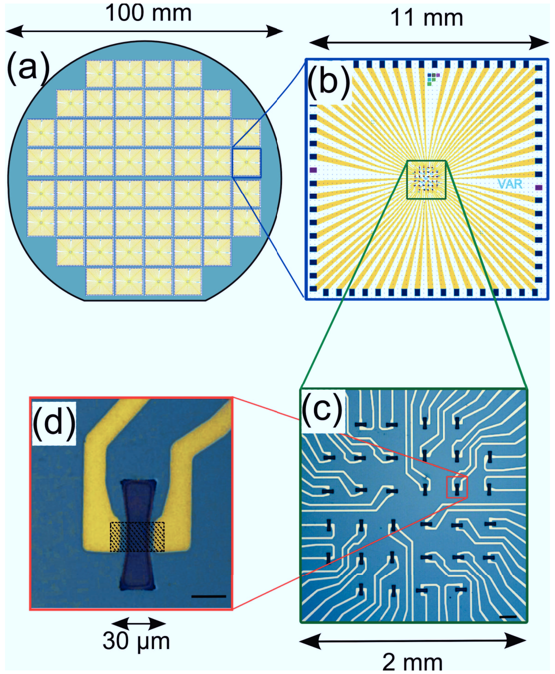

Figure 4.4: (a) the wafer design with 52 chips per wafer; (b) zoom into one chip; (c) close up of the middle 2mm× 2mm of one chip with an array of 32 GFETs; (d) a single completed GFET, graphene covers only the dashed area.

4.2 Transfer Procedure

Pre-treatments of Cu foil. A thin PMMA layer was spin-coated (1000rpm, 30 sec) on top of the Cu foil with graphene (see Figure 4.6a). Then the PMMA was baked at 150°C for five minutes in order to harden the polymer. The resulting thickness of the polymer was between 400 and 500 nm. Afterwards, the backside of the foil was exposed to oxygen plasma (100 W, 5 min, 0.8 mbar O_2) to etch the backside graphene.

Prior to the copper etch, the PMMA/Graphene/Cu foil was mechanically scratched with a blade. Such scratches cut through the PMMA layer in order to simplify and speed the subsequent transfer procedure and to have precisely shaped graphene pieces (see Figure 4.6b). In the next step, the copper foil was etched in 100 mM $(NH_4)_2S_2O_8$ (Sigma Aldrich), and we obtain many small floating PMMA/graphene pieces. After etching, the pieces were washed in a deionized (DI) water cascade before transferring into the main chamber.

As described above, each of the wafers contained 52 chips. Therefore, 52 pieces of graphene have to be transferred precisely at the zones of interest. This is done via combining three main parts:

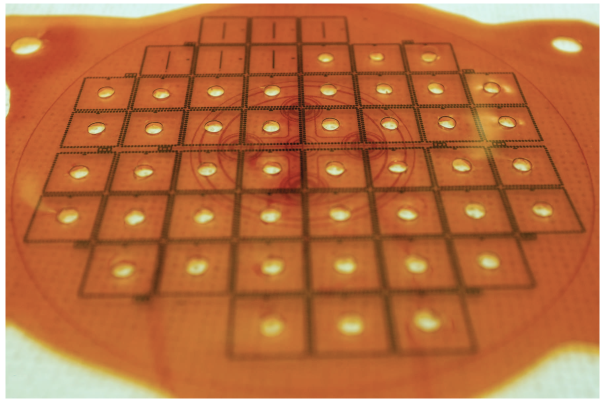

Figure 4.5: The mediator film made of kapton tape with 52 openings for graphene transfer and 6 openings for the alignment columns.

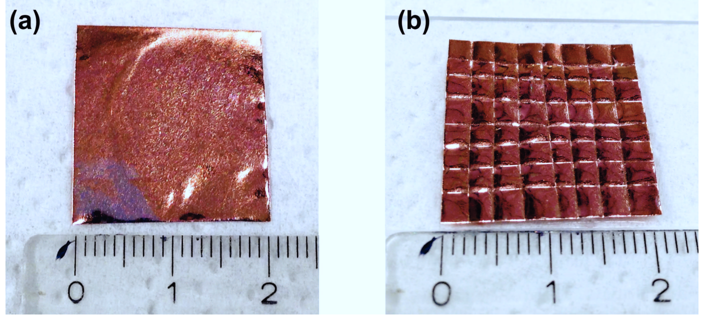

Figure 4.6: Photographs of: (a) as received copper foil with graphene and spin-coated PMMA on top; (b) The copper foil after scratching the PMMA.

1. the special chamber with wafer holder and alignment columns;
2. the mediator film with transfer openings and alignment markers;
3. an accurate control of the graphene flake's size and shape.

During the procedure, the wafer with pre-fabricated alignment markers (Figure 4.7a) is placed on the vacuum chuck. Then, the mediator film is placed on top of the wafer, and precisely aligned to the wafer below. The better the wafer and mediator film are aligned, the better and more reproducible is the result. Afterwards, the chamber is filled with deionized (DI) water to a level of approximately 2–3 cm above the wafer. During this process, the mediator film is lifted together with water level (Figure 4.7b).

For the transfer of graphene, the PMMA/graphene pieces of appropriate size are transferred one-by-one onto each of the openings in the mediator film. The transferred PMMA/graphene pieces were normally floating inside the openings. Then, by opening the outlet valve, the water level slowly decreases until the mediator film comes into contact with the wafer. Since the film and the wafer underneath are precisely aligned with each other, the graphene contacts the wafer exactly at the desired locations.

Next, the wafer is left to dry overnight. As the last step, the mediator film is picked up and the wafer with PMMA/graphene pieces on it undergoes the standard graphene post-transfer treatment. The final result can be seen in Figure 4.7c. The video of the whole process can be found in [55].

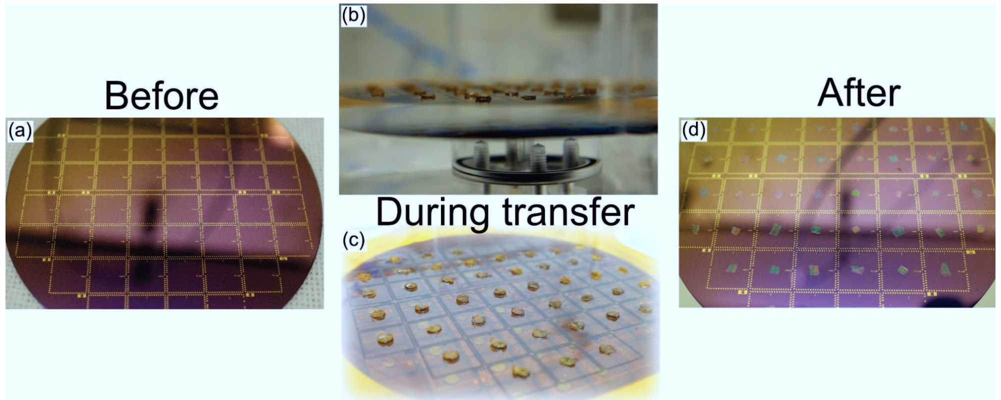

Figure 4.7: Photographs of the wafer before the transfer (a); the wafer and mediator film during the transfer (b); and the resulting wafer after the transfer with graphene pieces dried out in the middle of each chip (c).

Post transfer treatments When the pieces are transferred and dried out overnight, the wafer was annealed at 160°C for 15 minutes in order to improve adhesion and re-flow the PMMA [129]. At last, the wafer was immersed in a warm acetone bath for at least one hour and annealed at 350°C in an oxygen-free atmosphere in order to complete PMMA removal. The further fabrication process is described in detail in the supplementary information.

4.3 Transfer Yield Analysis

The transfer results were analyzed by post-processing of the optical images of the transferred graphene pieces (see Figure 4.8). Microscopic images of each flake were taken. Since the wafers already had some alignment markers (see Figure 4.8a-b), the images were then aligned with the mask design for graphene areas (see Figure 4.8c). Each image was manually analyzed for the amount of failed devices and the different types of failures: misalignment, crack/fold, insufficient flake size, excessive flake size, or broken flake. A flake is considered to be too small if it is not able to geometrically cover the middle area of chip. A flake is considered to be too large if it exceeds the dimensions of the opening in the mediator film,

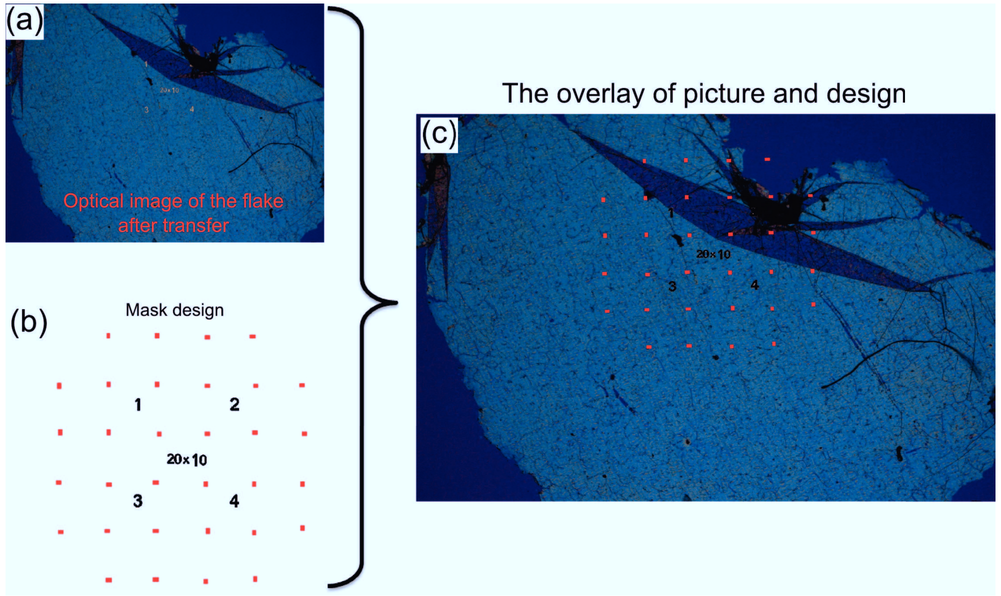

Figure 4.8: (a) Optical image of a transferred flake. (b) The mask design which is used for following graphene active area etching. (c) The two previous pictures are aligned with each other in order for following calculation of transfer yield.

causing it to fold, sandwiching the PMMA in the graphene. See Figure 4.9 for detailed descriptions and examples.

4.4 Results of the Transfer

We have conducted graphene transfers using the method described above on seven wafers (four SiO_2/Si wafers, one HfO_2/Si wafer, one sapphire and one flexible kapton film). Six wafers (not in the above-mentioned order) were processed in order to study the different types of failure that can occur during the transfer. These failures include: misalignments, cracks, folds, “excessive flake”, “insufficient flake” and broken flake. The last wafer, number seven was processed with the knowledge of the previous error types and with precautions to prevent the common transfer failures.

Figure 4.10 shows the total yield of each wafer. As it can be seen, the first six wafers result in approximately 80% yield. However, many of these wafers were fabricated with intention of failures, in order to study their influence. For example, graphene transferred on wafers number 4, 5 and 6 was intentionally cut after the wet etching process. Such cutting resulted in less consistent flake size and shape and consequently a reduced number of functional devices, as can be seen from the distribution (Figure 4.10).

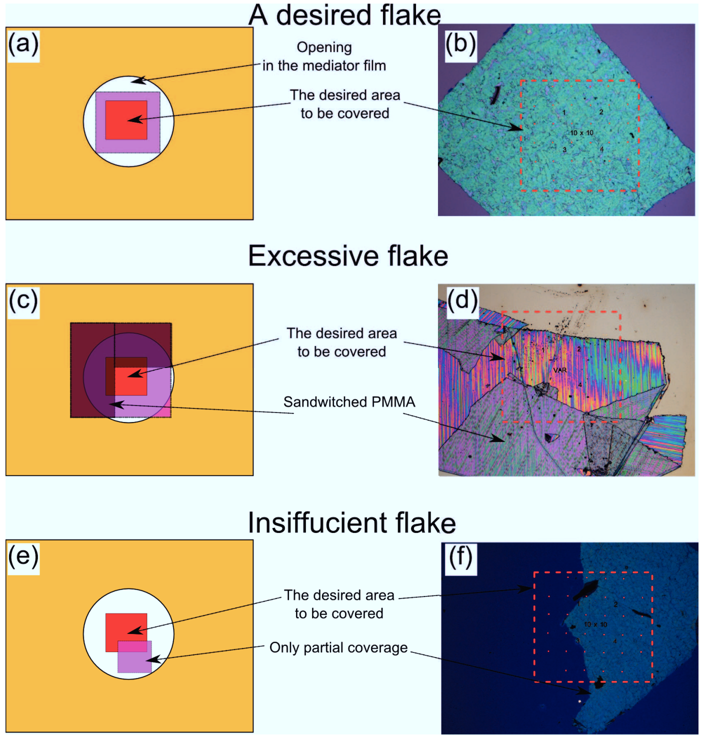

Figure 4.9: A simple nomenclature and description of an excessive and insufficient flake with examples. At the left sides (a, c, e) are given schematics, where kapton tape with openings is shown in orange, desired graphene area in red and graphene flake in purple. At the right sides are given exemplary optical pictures for each flake type (b, d, f).

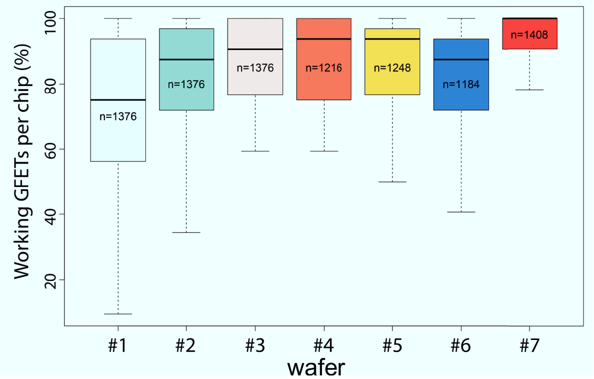

Figure 4.10: The fabrication yield of each wafer as percentage of successfully transferred and aligned flakes resulting in working GFETs.

As it is indicated in Figure 4.11a, the main reason for failure is due to misalignment of the flakes (54% of total failures). The second and third most common failure types are the broken flake (18%) and presence of cracks/folds (15%). The least two frequent failure types are "insufficient flakes" (10.5%) and "excessive flakes" (2.5%). The percentages given above are normalized to the total number of the broken devices. But, if we normalize such counts into failure efficiency (Figure 4.11b), which would be the ratio between the number of the broken devices vs the number of that type of failure. Such a calculation gives quite unexpected results. While the misalignment and cracks/folds are still the main failure classes, they result in the smallest failure efficiencies of 7.83 and 2.8 devices per failure, respectively. The too small flake and the broken flake type failures, surprisingly, have the largest rate of broken FETs per occurrence: 15 and 14.8 respectively.

Therefore, the misalignment and the cracks/folds failures could be counted as unsystematic and be present even in the best cases. At the same time, it seems to be important to keep the flake sizes precisely controlled. As one can see from the above mentioned results (see Figure 4.11b), even the smallest deformation can lead to significant failures.

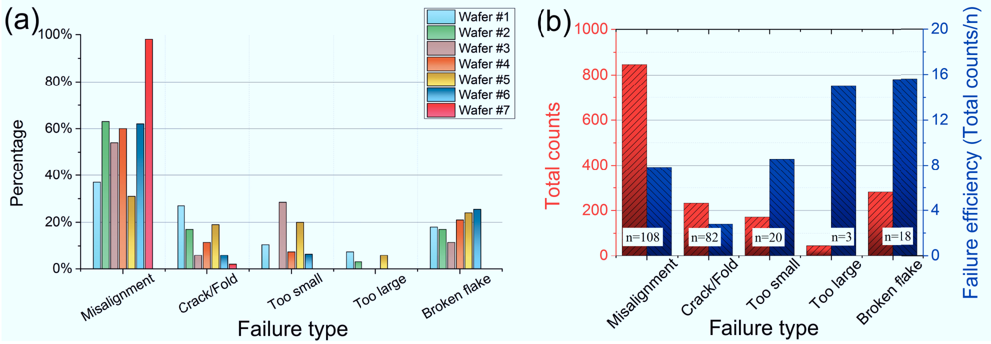

Figure 4.11: (a) The histogram of distribution of different failure types from each wafer. (b) Total counts of the failures of each kind and corresponding failure efficiency as the number of non-working devices per failure type.

Since the slight misalignment seems to be the most common failure reason, it should be visible at the geometrical mapping of the "dead" devices. Figure 4.12 represents the distribution of relative failure probabilities over the GFET array. As one can see, the probability is higher at the edges and lower in the middle. Nevertheless, there is a non-zero failure probability all-over the chip, which is due to random occurrences of other failure types, such as cracks and folds.

As one can see from the example of the last wafer (№7), where all the previous errors had been taken into account, and the only major failure type is the misalignment, the wafer results in over 90% yield. Detailed statistical information on the wafer №7 is presented at the Figure 4.13.

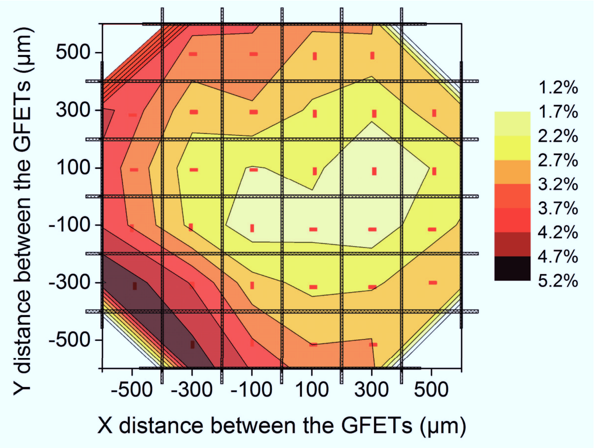

Figure 4.12: The geometrical distribution of the failures showing the predominance of the misalignment failure.

Another straightforward result of such transfer is reducing the amount of PMMA used. As PMMA is one of the main transfer problems, reducing the total volume of the PMMA results in a faster dissolution of the polymer in acetone and lower concentration of PMMA, therefore a lower contamination level. We used four different kinds of substrates for the transfer, and no special wafer-type deviation was found, which makes the method very general and suitable for all kinds of semiconductor substrates. Overall, the time–limiting step of our method is the transfer of the PMMA/graphene pieces onto the opening in the mediator film. For the geometric layout presented here with 52 devices, this process typically requires 30 minutes for an experienced user.

Recently, many new approaches for graphene transfer have appeared in the literature [130] several of which solve the problem of contamination [129], adhesion [131] or interface [132]. Some of them try to solve the problem of the material waste via electrochemical delamination [133, 134], but these methods are unscalable. For that reason, we believe our method can be simply modified with the above mentioned improvements and will result in a generally fault-free, cheap and easy graphene transfer.

4.5 Summary

A high-throughput graphene transfer method had been presented. We have introduced a scalable and simple method for transferring graphene to specific locations on a substrate. Our technique makes use of standard wet-etching in combination with directed transfer based on perforated alignment masks. The described method helps to reduce the amount

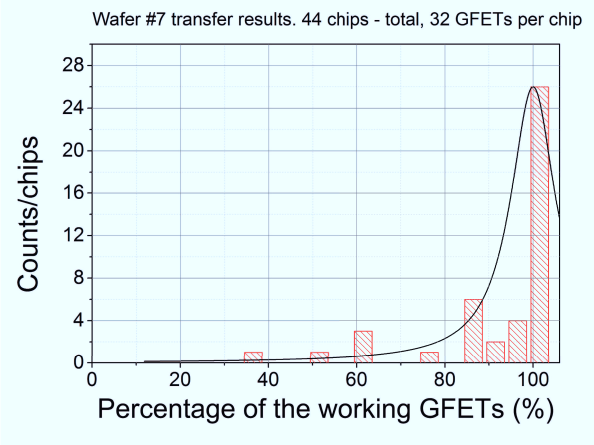

Figure 4.13: The detailed information about the amount of working GFETs per chip from the last wafer, with corrective measures.

of graphene used, together with improving other transfer issues, like PMMA contamination. As soon as all the mistakes and mismatches in the transfer protocol are taken into account, the whole 4–inch wafer can be fabricated with a yield over 90% by using only a 4 cm^2 piece of graphene. Compared to the conventional large piece wet transfer, we result in tremendous improvement of the UWR. In our case the improvement is 34–fold.

Chapter 5

GFETs

The chapter describes fabrication, characterization and use of GFETs for electrophysiological experiments. Rigid GFETs are introduced in the first Section and semi-flexible PIonS-based GFETs in the second Section. A comprehensive modeling of interface capacitance as well as discussion of liquid gated GFETs' mobility is given in the chapter.

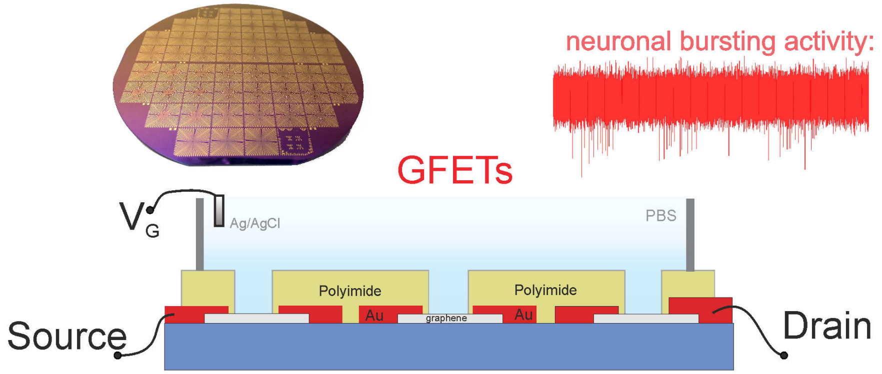

This chapter was reproduced in part from the following works:

- **D. Kireev**, M. Brambach, S. Seyock, V. Maybeck, W. Fu, B. Wolfrum, A. Offenhäusser. Graphene transistors for interfacing with cells: towards a deeper understanding of liquid gating and sensitivity. *Scientific Reports*, **2017**, 7, 6658.
- **D. Kireev**, I. Zadorozhnyi, T. Qiu, D. Sarik, F. Brings, T. Wu, S. Seyock, V. Maybeck, M. Lottner, B.M. Blaschke, J. Garrido, X. Xie, S. Vitusevich, B. Wolfrum and A. Offenhäusser. Graphene field effect transistors for *in vitro* and *ex vivo* recordings. *IEEE Transactions on Nanotechnology*, **2016**, 17, 140-147.

5.1 Rigid GFETs

In the field of bioelectronics, graphene is a promising candidate for very efficient, flexible, biocompatible and implantable sensors [85, 135]. Up to now, most of fabrication routes for graphene-based bioelectronics are still at an early development stage where devices are processed individually or in a small arrays comprising only a few devices.

There have been many attempts in recent years to transfer single-device processing towards wafer-scale fabrication: some are still focused on epitaxially grown graphene, [136, 137] some have made their attempts on using chemical vapor deposition (CVD) graphene [53,138,139]. One of the main problems in this regard was previously given by the quality of CVD-grown graphene [140]. Although, as recently reported, the CVD graphene can be grown on Cu or Cu-Ni foils with grain sizes up to the centimeter scale [71, 121]. However, the graphene still needs to be transferred to device-compatible substrates and the transfer process can introduce defects and in consequence a low yield in functional devices [106, 124].

Moreover, to conduct cellular measurements, in a good quality, one needs to establish a reproducible fabrication process. Most of the graphene field effect transistors (GFETs), or their arrays are still fabricated on a chip-scale [45, 141, 142]. The only wafer-scale biochemically applicable GFETs reported so far, were fabricated with a low density of devices [53]. As shown in the previous Chapter 4, we can use the efficient way of graphene transfer, which requires only 4 cm^2 of the graphene-on-copper for fabrication of one 4–inch wafer with 52 devices per wafer [55]. This, combined with the cm-scale sizes of graphene domains [71], we aim to result in identical performance of the GFETs.

Transistors are very interesting for bioelectronics, since compared to multielectrode arrays (MEAs) [13], they are active elements, and, therefore, more functional and tunable. Moreover, it is possible to decrease the device's size without impairing its performance (if the W/L ratio is preserved), which is not possible with MEAs.

In this work we present a large scale fabrication of the GFETs aimed for bioelectronics applications. Fabricated on 4–inch scale, the process can be further adjusted to 6– and 8–inch processes with similar yield. Altogether we evaluate the performance of the solution-gated GFETs (contact resistance, mobility and transconductance) depending on: (a) processing parameters, including substrate type (SiO_2, HfO_2, sapphire, polyimide), passivation, geometric considerations, and graphene channel size; (b) measurement conditions, including ionic strength of used solution and applied potentials. Bio-experiments, consisting of *ex vivo* (heart tissue) and *in vitro* (HL-1 cardiac cell line and cortical neurons) recordings, prove the applicability of such graphene transistors for bioelectronics.

5.1.1 Fabrication

The device' fabrication is done in the cleanroom, except the graphene transfer step. The complete cleanroom fabrication recipes can be found in the appendices A and B.

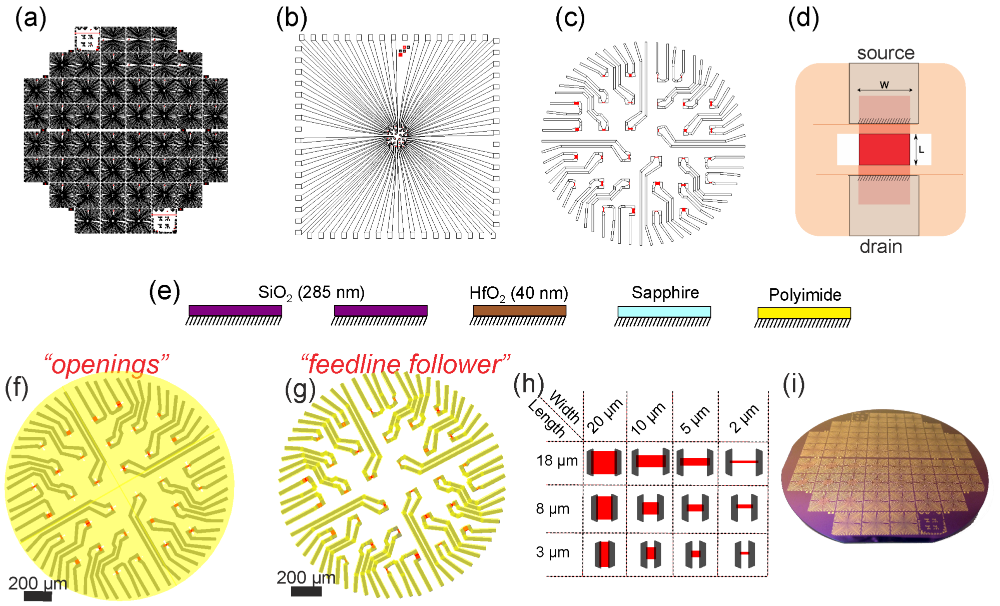

Figure 5.1: Overview of the fabrication process. (a) Mask design for the GFET fabrication of 52 chips on a 4–inch wafer. Zoom into the design layout of one of the chips is shown in (b), with an array of 32 GFETs in the middle area in (c) and zoom into one of the GFETs in (d) Graphene is shown in red, and passivation in sandy brown color. (e) Five different substrates which are analyzed in the scope of this thesis. In (f) and (g) are shown two different passivation methods, analyzed i the scope of this thesis. (h) The sketch shows the 12 variations in width and length of the GFETs, studied in the work. Graphene is shown in red, and passivation in yellow. (i) Photograph of a fabricated wafer.

The graphene was CVD grown on 25 µm thick copper foils as described in Section 3.1. A thin layer of PMMA was used as a support layer during the transfer. In order to not waste large fraction of the graphene layer, we used the modified, high-throughput transfer technique, described in Chapter 4. The graphene is transferred onto the wafer with already pre-fabricated Ti/Au markers for further alignment, patterning and metallization using standard UV-photolithography and oxygen plasma etching (see Appendix A for details). The 10nm Ti and 100nm Au metallization stack was deposited via e-beam assisted evaporation on the wafer with pre-defined structure of LOR-3B and AZ nLOF-2020 photoresists. Photostructurable polyimide (HD-8820, HD Microsystems) was used as the last step of passivation. Spin-coated at 5000 rpm, soft-baked, exposed, developed and annealed with a slow ramp up to 350°C and slow cooling down, the polyimide form a perfect, pinhole-free, 3 μm thick passivation.

In order to provide a comprehensive statistical analysis and extensive cellular recordings study, we fabricate our devices on 4–inch wafers (Figure 5.1a). Each wafer consists of 52 chips with different layouts. The chips (Figure 5.1b) are designed and fabricated in order to fulfill the main task: to measure and track the propagation of extracellular electrical signals through the cellular layer. Therefore it is important to have a structured array of 32 devices (6 by 6 excluding four corners) with inter-device distance of 200 μm (See Figure 5.1b-c). The length of the liquid gate GFETs is further defined by opening in the passivation (see Figure 5.1d). Such devices can be fabricated on any silicon technology compatible wafer. In this section of the thesis we present the experimental data collected from five wafers: two SiO_2/Si (further denoted as Si–I and Si–II), one sapphire (Sap), one HfO_2/Si (Hf), and one polyimide/Si (PI) (see Figure 5.1e). The Si–I, Sap, Hf and PI wafers are fabricated in a top contact method, while the Si–II wafer is fabricated with graphene metallized from two sides.

Two different passivation schematics have been used in the scope of this thesis. First is so-called "passivation openings", where the whole surface of the chip is covered with the passivation layer (polyimide in our case), except the areas of graphene transistors (see Figure 5.1f). The second one is introduced in this work for the first time, so-called "feedline follower", where the passivation covers only the metallic feedlines, leaving a large area of bare substrate open for the liquid environment and interaction with cell culture (see Figure 5.1g). The advantages and disadvantages of the methods are discussed below in the results section. In order to investigate the influence of the graphene area's shape on the final performance of the device, some of the chips we fabricate with varied W/L ratios of graphene, as schematically shown in Figure 5.1h.

5.1.2 Characterization

The electrical characterization of the GFETs are performed using a Keithley 4200 semiconductor characterization system (see section 3.3.1). Drain and source electrodes of a GFET are contacted with tungsten needles and the gate is contacted via an Ag/AgCl pellet electrode inserted into an ionic solution. The characterization of a GFET consists of two steps: current annealing and measurement.

Current annealing. The annealing step is required to bring the transistor into operative state and is important for further accurate analysis of the devices. During the annealing step, the drain-source current, I_{DS}, is recorded, while the gate potential, V_{GS}, is swept against the Ag/AgCl pellet electrode from 0 V to 1 V. First characterization of the GFETs usually results in the situation when the charge neutrality point (Dirac point) is far in the p-doping regime (see Figure 5.2a). Every consecutive measurement is bringing the Dirac point to the left, until a stable position ($V_{Dirac} \sim 350 \pm 100$ mV) is reached (Figure 5.2a and 5.2b). Further measurements do not result in shift of the Dirac point nor in the resistance of the GFETs. Usually, the larger the V_{GS} sweep window is, the faster the curve stabilizes. Previous investigations have reported a similar phenomenon, based on current annealing, which consider the atomic re-structuring of the graphene lattice.[21-23] However, it is unlikely that this effect is responsible for the observation in our case, considering the low current/potential levels, which are not enough to result in such effect. The drain-source current density,[21,22] results in the order of 10^6 A/cm^2, which is not enough to actually anneal the graphene lattice, especially considering the liquid environment.

Moreover, when reducing the drain-source potential to 1mV, the effect remains although the actual channel current density is decreased to an order of 10^4 A/cm^2. The gate leakage current I_{GS} is increasing with the gate source voltage V_{GS}. This effect becomes more pronounced after each annealing step (Figure 5.2c).

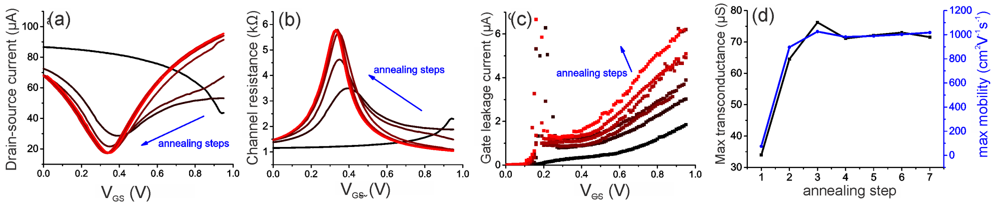

Figure 5.2: The evolution of the I_{DS}–V_{GS} (a) and R–V_{GS} (b) curves over the consecutive annealing steps. Visible, the device's performance stabilizes over the measurements. (c) The leakage current dependency on the V_{GS}. (d) The evolution in the transconductance and mobility of the GFET over the annealing cycles.

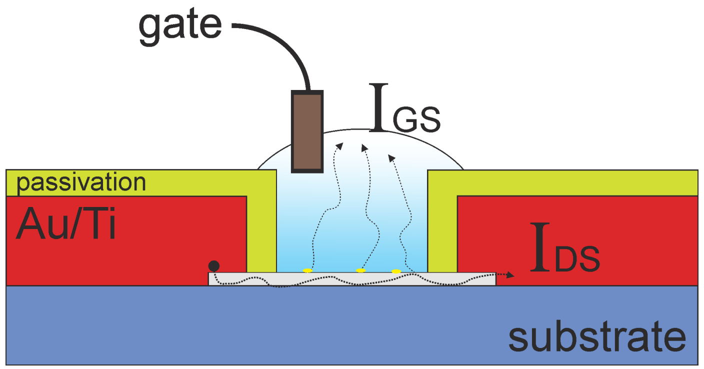

Figure 5.3: The proposed schematics of current-induced annealing of the graphene sheet under liquid physiological conditions. While the I_{GS} current is comparably small, it can flow through the point defects in graphene, therefore anneal it.

This is an interesting phenomenon, which has not been previously reported in literature to the best of our knowledge. We suggest that the effect originates from the removal of the cleanroom process contaminants (which p-dope the graphene) via a simple electrochemistry either due to out-of-plane leakage current (I_{GS}, see the proposed schematics in Figure 5.3). Application of high V_{GS} potentials up to 1.4V vs a Ag/AgCl electrode, increases the gate leakage current up to tens of nA (see Figure 5.2c). The cleaning from contaminants can result in an intermediate step, when a local doping creates a second conduction minima (pseudo Dirac point). Every consecutive measurement reduces the second conduction minima, finally resulting in a normal Dirac-wise I-V curve (see Figure 5.4). Evolution of the transconductance and mobility of the devices over the annealing cycles is given at the Figure 5.2d. The data show that the first transfer curve, is not an appropriate indicator for further data processing, but it already stabilizes after the 3rd measurement (in this case).

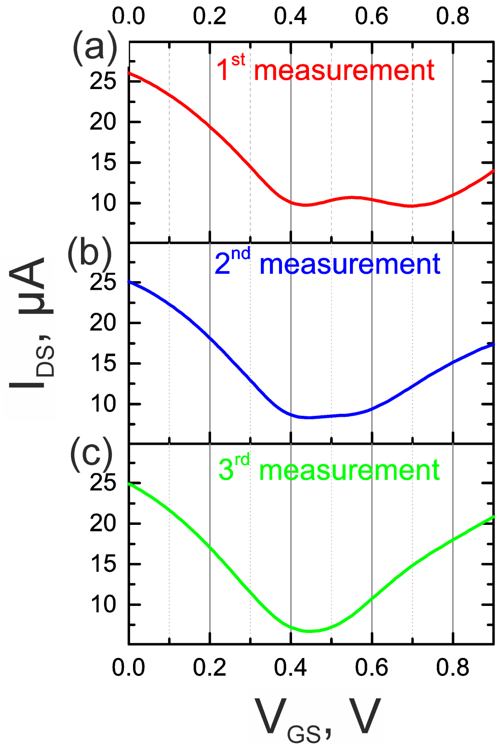

Figure 5.4: The three I-V curves from one GFET recorded consecutively one after each other. While the first recording (a) shows a double Dirac behavior, it starts to disappear in the second recording (b) and is completely gone after the third measurement (c).

I-V measurements. Once annealed, the graphene transistors are characterized (V_{GS} sweeping 0V– 0.8V; $V_{DS} = 0.1$V) and analyzed for their performance, including maximum transconductance (g_m), mobility (μ), Dirac resistance (V_{Dirac}), contact resistance (R_C), and sheet resistance (R_S) (see Figure 5.5 for detailed plots). The first two, namely maximum value of transconductance, g_m, and a maximum value of field effect mobility,μ_{max} are usually taken into the consideration for comparison with other materials and works [143]. In order to calculate and plot the mobility values (such as shown in Figure 5.5d), knowledge of interface capacitance is important, as introduced in Section 2.2 and discussed further in this chapter. Remarkably, some of the other values, like sheet resistance, R_S, can be used for rough evaluation of the GFET's quality, while values of mobility have to be carefully examined in order to provide a correct and valuable comparison.

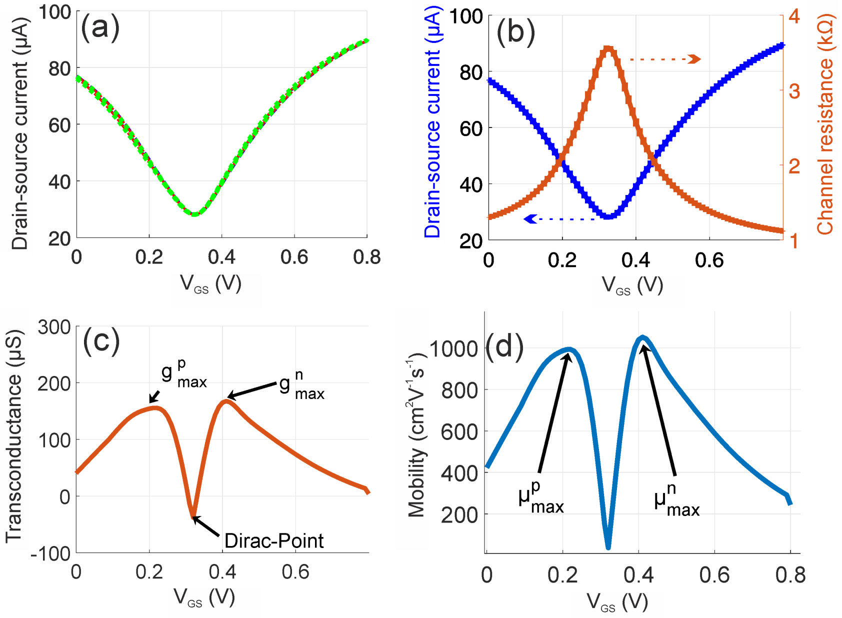

Figure 5.5: (a) An I–V curve from a GFET in stable operation mode. (b) The same I–V curve (blue) plus Resistance plot (brown). (c) The derived transconductance plot, smoothed to get correct max transconductance values and their positions. (d) Mobility plot with two max values for electron and hole conductance valleys.

Capacitance, ionic strength, mobility and transconductance. From the equation for a transistor in a linear regime (see Section 2.2 and ref. [82]):

$$I_{DS} = \frac{W}{L} \cdot \mu \cdot C_{interface} \cdot (V_{GS} - V_{Dirac}) \cdot V_{DS} \tag{5.1}$$

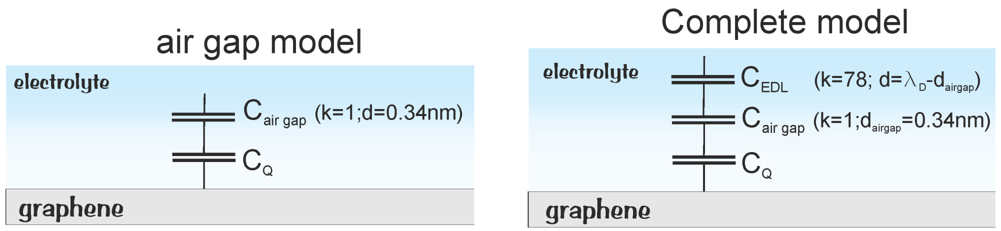

Figure 5.6: The two models of interfacial capacitance. Air gap model - a simplified version, and can be used for a high ionic strength electrolytes. A complete model - taking into account EDL for low ionic strengths solutions.

we can calculate the mobility:

$$\mu = \frac{L}{W} \cdot \frac{g}{C_{interface} \cdot V_{DS}} \tag{5.2}$$

where

$$g = \frac{\partial I_{DS}}{\partial V_{GS}} \tag{5.3}$$

where $C_{interface}$ is equal to C_{total}, and is given in equation 2.14.

Transconductance is simply the 1st order derivative from the I-V curve and the most important and direct value of a transistor's sensitivity. Mobility, on the other hand, is a more complex value, which requires knowledge of the interface capacitance. Specifically, it is known that graphene devices, biased via a liquid gate, undergo a very complicated phenomena. For a proper modeling one has to consider the electric double layer (EDL) capacitance, C_{EDL}, and the quantum capacitance, C_Q of the graphene itself (Figure 5.7a) [44, 86–88]. While the C_{EDL} is a simple parallel-plate capacitor, the C_Q is an intrinsic property of graphene and depends on the charge carrier concentration, $n_G = \left(\frac{eV_{GS}}{\hbar v_F \sqrt{\pi}}\right)^2$ induced by gate potential and n^*, induced by charge impurities (varies from 1×10^{11} to 1×10^{12} cm^{-2}) [86]. An extra term, so called “air gap” capacitance, C_{airgap}, was proposed later and is valid for the cases of hydrophobic materials (such as graphene) and high ionic concentrations, when the usual method would assume a non-physical approach of ions coming too close to the graphene surface [44,45,144]. For details of the calculations, please see the section 2.2 in fundamentals.

The “air gap” parameter in general takes the place of the Stern layer in our model (see discussion on EDL in Section 2.3) [144]. Finally we combine all three terms (see equation 2.14). In order to provide a comprehensive analysis, we measured six GFETs in a series of PBS diluted solutions (from 10x down to 0.001x). 10x PBS is a solution with ionic strength of 1.62M, which would result in a Debye length of 0.24 nm, such values are not physically possible [144], therefore for the highly concentrated salt solutions, the “air-gap” simplified

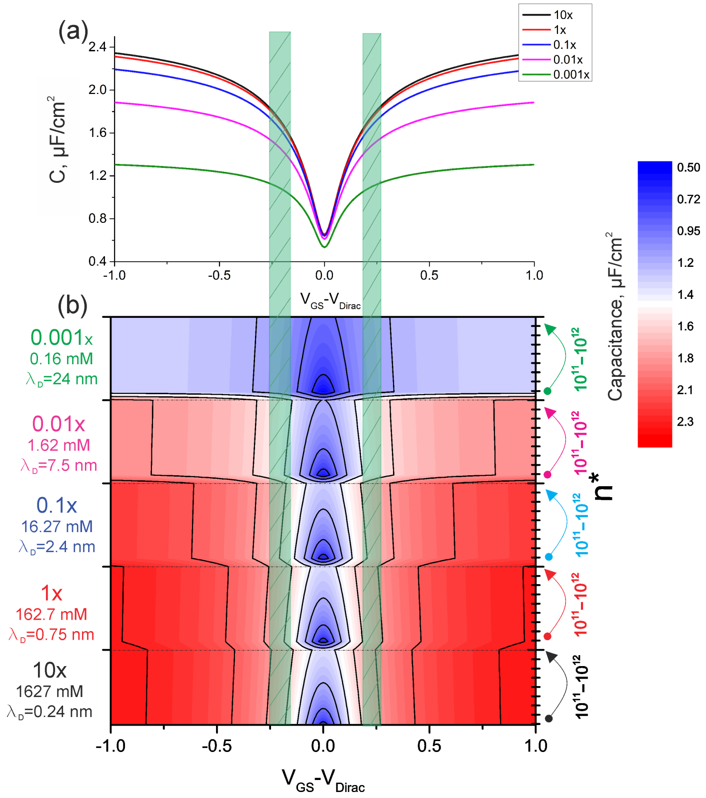

Figure 5.7: (a) The $C_{interface} - V_{GS}$ plots derived from the corresponding models (see Figure 5.6), $n^* = 1 \times 10^{11}$ cm^{-2}. Calculations are given in the fundamentals 2.2. (b) The more detailed color plot of capacitance over V_{GS}, while varying both ionic strength of the solution and n^* during modeling. The green dashed areas represent the areas of maximum transconductance/mobility.

model is used for the capacitance calculations. Therefore the model for the diffuse layer breaks down for high concentrations and steric repulsion has to be considered. Nevertheless as the capacitance is anyhow dominated by the "air gap" or Stern layer in this case, we use the simpler model, just taking into account the quantum and "air gap" capacitances (see Figure 5.7b). For further PBS concentrations we use a more complicated model, which additionally takes into account the capacitance of the diffuse double layer (see Figure 5.7a). Since the quantum capacitance of the graphene depends on the number of charge carriers induced by gate potential, the overall capacitance of the liquid-gated graphene transistor depends on the V_{GS} potential. The overall $C_{total} - V_{GS}$ plot for different PBS concentrations is given in Figure 5.7a. The plot, given in Figure 5.7b is modeled, considering $n^* = 1 \times 10^{11}$ cm^{-2}. In order to understand the significance of the n* we have plotted the calculated capacitance over 5 values of PBS concentration while changing the n* from 1×10^{11} cm^{-2}

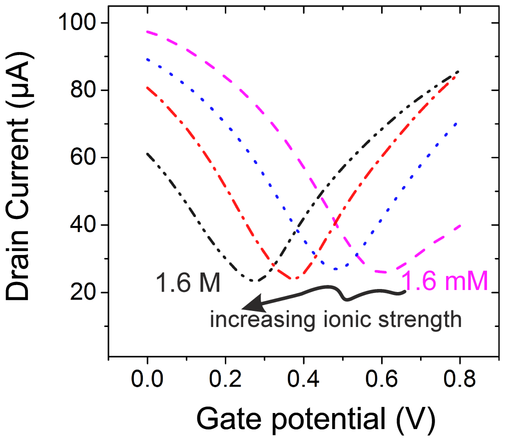

Figure 5.8: The I-V curves for a GFET measured with solutions of different ionic strength. The shift of the Dirac point to the left is due to chemical potential change.

and 1×10^{12} cm^{-2} (see Figure 5.7b and 2.7 for a more detailed plot). Resulting behavior shows that increase of n^* value increases the overall capacitance value. Nevertheless the changes are only valuable close to Dirac point (±100mV), but can be neglected in the regions of maximum transconductance/mobility (green dashed areas in Figure 5.7a-b).

Transfer curves from one of the GFETs are given in the Figure 5.8. Dirac point position of the GFET shifts depending on the used ionic strength of solution, as visible in Figure 5.8. This dependency can be explained by the change of the chemical potential of the solution when changing its molarity/ionic strength. The Dirac point shift is –83±17 mV/decade, from which the 60 mV/decade of the response must be subtracted due to changes in the chloride concentration when diluting the PBS buffers. The Dirac point shift of -23±17 mV per decade is comparably small to previous report [53], suggesting an advantageously cleaner surface [51].

In the Figure 5.9 is given the summary of the GFET's performance in different PBS solutions: while Dirac points shifts due to change in chemical potential, the transconductance and correctly estimated mobility values are not significantly different.

Effect of substrate and geometry on GFET's performance. Further analysis of device performance is done regarding the processing parameters, i.e. substrate, width and length of the graphene area and type of the contacts. For this purpose, over 500 GFETs from different wafers (Si–I, Si–II, Hf, Sap, PI) with different lengths and widths are measured and analyzed. The ionic solution and V_{DS} potential are kept constant for every measurement. The outcome result is that transconductance is linearly depend on width-to-length (W/L) ratio of the device (see Figures 5.11a-c). Figure 5.11d is showing the transconductance

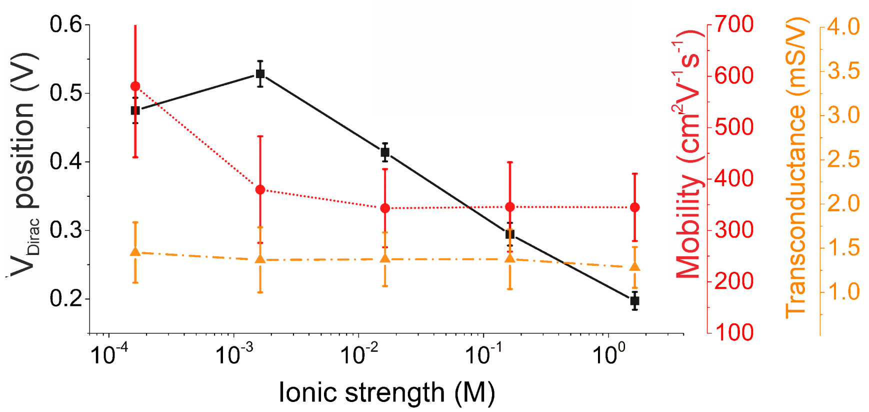

Figure 5.9: The evolution of the three main GFET parameters: position of the Dirac point, mobility and transconductance over the ionic strength of the used solution. Each data point is calculated for five devices. Error bars represent differences in transistor performance and not measurement error.

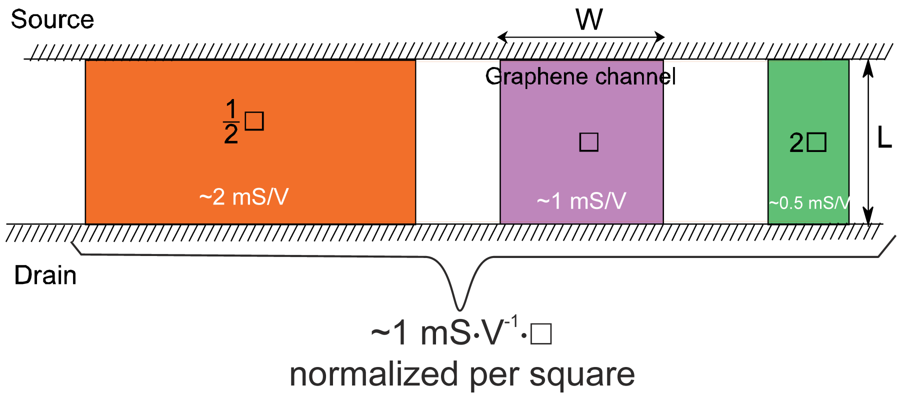

Figure 5.10: A sketch for understanding the geometrical value of a square (□) in the performance of the GFETs.

values for devices from one wafer (Si–I) for each width and length and represent the same above-described trend. Therefore, hereby we would like to propose the normalization of the transconductance to a number of squares (one square (□) is when W/L=1, see Figure 5.10). Such normalization will bring more comparable understanding of device's intrinsic properties.

Interestingly to note, the mean values of the normalized transconductance, as plotted in Figure 5.11c, do not depend drastically on the underlying substrate. The mean values of transconductance, normalized on V_{DS} and number of squares (□), for all five wafers are in

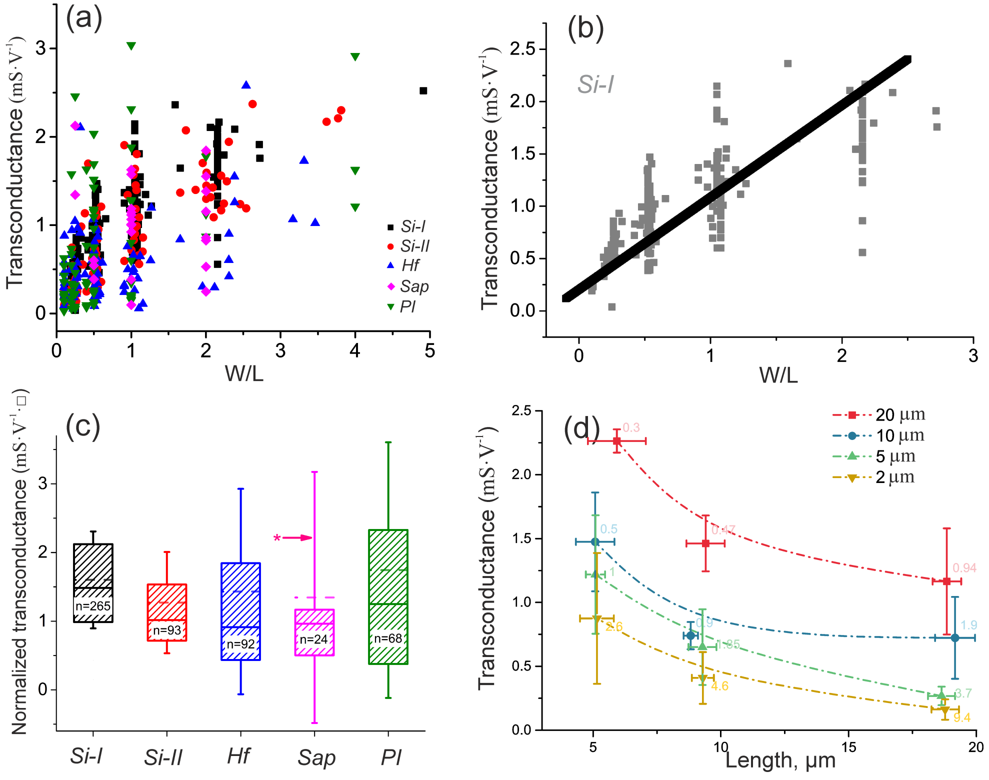

Figure 5.11: (a) The scatter plot of the transconductances for the 542 devices from five different wafers, somewhat resembling the linear dependency towards W/L ratio. In (b) are given the scatter values of the transconductances of the wafer Si–I, and a simple linear correlation, with a correlation coefficient of 81%. In (c) are given the statistical distributions of the normalized transconductance for each wafer type. The transconductance here is normalized per V_{DS} and number of squares. The box is 25%, 50%, and 75%, and the outlines are standard deviation, the dashed line shows mean. In (d) are shown the data points for wafer Si–II, split for each width and length. The width here is kept constant (20 µm, 10 µm, 5 µm, and 2 µm), while length is varied.

the range of 1-2 mS V^{-1} □.

In order to understand the values of field effect mobilities (measured and calculated with ionic strength of 162.7 mM), they are averaged for each wafer (see Figure 5.12a). The same CVD grown graphene was used for all five wafers, and the mobilities are quite similar for all wafers and in the range of 500-1000 cm^2 V^{-1} s^{-1}. However, one can see that there are rare occurrences of extra-large mobility values especially for the HfO_2, sapphire, and polyimide substrates (Figure 5.12b). In order to understand the origin of such large mobilities we plot the data for each transistor for each wafer over the area of graphene channel (Figure 5.12a). There it becomes clear that the extremely high mobility values

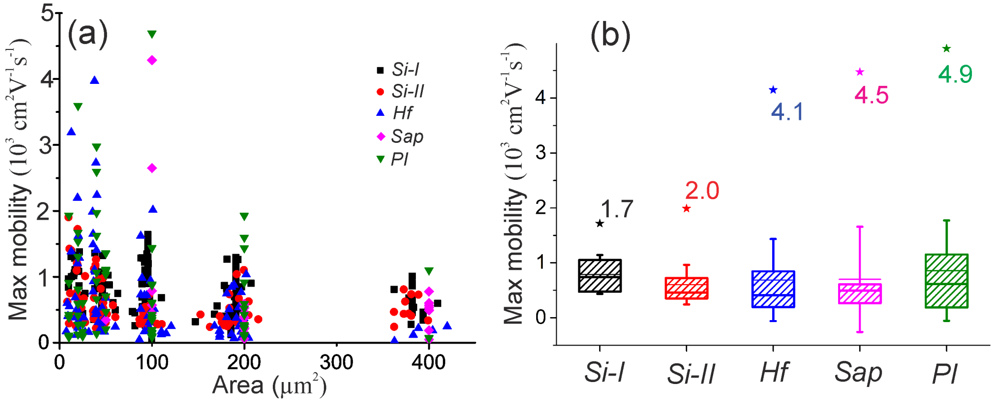

Figure 5.12: (a) The scatter plot of all mobility values over the area of the graphene for each wafer. One can see a general guideline that most of the devices' performance does not depend on the area, except for the smallest devices. (b) The statistical distribution of the mobility values and their maximum values. The box is 25%, 50% and 75%, and the outlines are SD, the solid line shows the mean.

only happen in devices with very small channel area (below 100 µm^2). We believe this is due to crystallinity of the graphene and the number of substrate-induced scattering. Although the devices on SiO_2 substrate have the largest mobility in average (750±350 cm^2 V^{-1} s^{-1}), the SiO_2 substrate results in a suppression of the mobility, compared to HfO_2, sapphire and polyimide substrates, where the value can reach up to $4.9{\times}10^3$ cm^2 V^{-1} s^{-1}.

The last two parameters, important for characterization of the GFETs are the contact resistance, R_C and transfer length $\mathrm{L_T}$. The transfer length is the path a charge carrier has to travel underneath the contact area before transfer to the feedline. Decreasing the transfer length is important for further miniaturization of the devices. The transmission line measurement technique (TLMT) has been used to determine the parameters [145]. We analyzed the difference in the contact resistance for wafer Si–I (top contacted, Figure 5.13a) and Si–II (double contacted, Figure 5.13b). The mean value of both wafers' sheet resistances are: $R_{S,Si-I} = 1550{\pm}820\ \Omega$ and $R_{S,Si-II} = 1210{\pm}1040\ \Omega$. These two values are compatible within two standard deviations from each other. The computed overall transfer length for the wafers are:$L_{T,Si-I} = 8.5 \pm 2.2$ µm and $L_{T,Si-II} = 3.6 \pm 2.2$ µm. This shows that the transfer length could be reduced by more than factor 2 using double contacted graphene.

Table 5.1, at the end of this chapter is provided in order to directly compare our data to the data from previously published works [44,45,53,141,146–148], recalculated with the geometrical and environmental factors taken into account. Interesting to see, first of all that just voltage normalized transconductance values can be misleading, and the values are extremely over/under estimated. When the values are further normalized per number

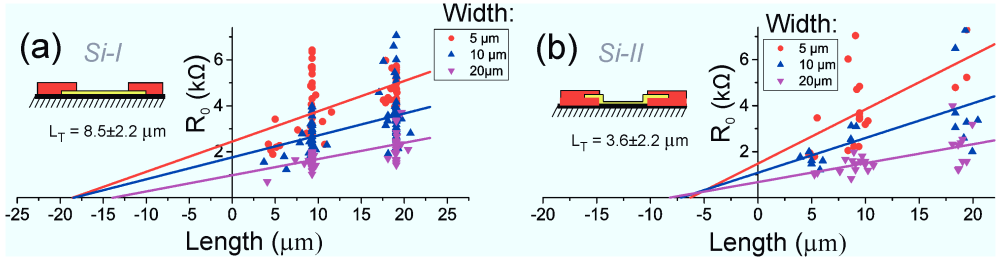

Figure 5.13: (a) and (b) Are the TLM plots for wafers with single (Si–I, $n = 265$) and double (Si–II, $n = 93$) contacted graphene respectively.

of squares, the final performance show similar trend.

5.1.3 Extracellular Measurements

5.1.3.1 HL-1

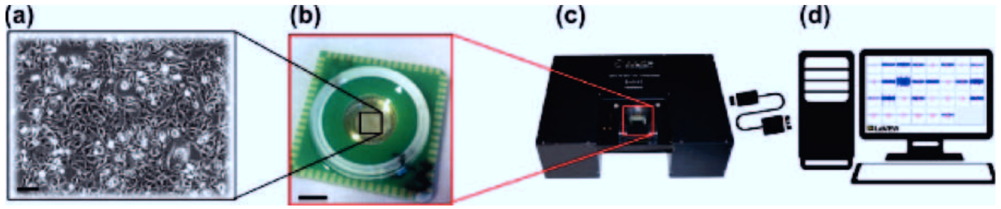

Figure 5.14: The schematics of the *in vitro* experiments: (a) a transmitted light optical image of the HL-1 cell culture. Scale bar, 20 µm. (b) Photograph of the chip, bonded to the carrier and encapsulated with PDMS and glass rings for medium storage. Scale bar, 5 mm. (c) A multichannel measurement headstage, manipulated via PC (d) with LabView based software.

Cardiomyocyte cells (HL–1 cell line), are further cultured on the chips' surface (see Figure 5.15a). A typical timetrace recording from one GFET from the chip with cardiac action potentials is shown in Figure 5.15b. The cells are "beating" (producing repetitive APs through the membrane of the whole cellular layer, as described in Section 2.4 of this thesis) with rate of 23±3 *beats per minute* (bpm) and amplitude of 1.2±0.2 mV. Considering the 2×MAD noise level of 200 µV, the overall SNR is 6±1 which is in the same sensitivity range as reported previously [147, 149]. The shape of the APs is shown in Figure 5.15c, where over 115 consecutive spikes are averaged and the average AP is shown in blue. The shape of the action potential, as in agreement with previous works represent a very good sealing between a cell and transistor [150, 151].

Further reported, more comprehensive HL-1 recordings were done on sapphire–based GFETs, fabricated by the collaborators at the Technical University of Munchen (TUM), see references [43, 45] for details. The *in vitro* measurements are done on the sapphire

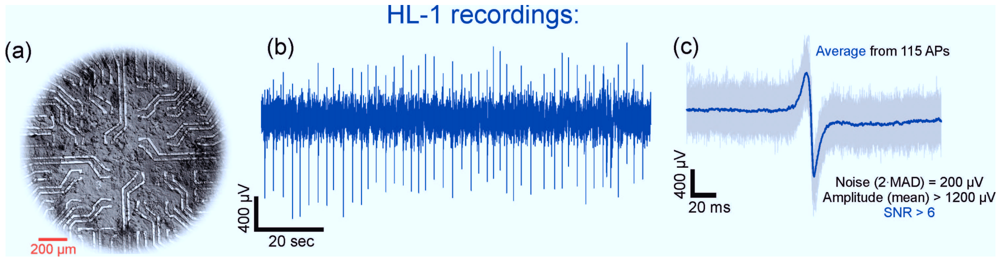

Figure 5.15: (a) An optical micrograph of an HL-1 cell culture on top of a GFET chip. (b) A typical time trace recording of HL-1 activity recorded with a graphene transistor. (c) The averaged HL-1 spikes (blue) from 115 individual consecutive spikes from the chip.

chips, which show comparably high transconductance values, and at the same time, low noise performance. HL-1 cell culture is chosen as the test cell culture, since the confluent cell layer leads to good cell-device coupling and APs are spontaneously generated by pacemaker cells. These APs are repetitive and propagate through the whole cellular layer [106, 144]. Furthermore, the associated cell contraction can be monitored to determine the maturity of the culture and therefore the appropriate time to measure electrical signals. The cells (see Figure 5.14a) are cultured on the encapsulated chips (see Figure 5.14b) until they form a confluent layer. As soon as the cells reach a confluent state, and form gap junctions, they start beating, therefore producing the extracellular potentials. Considering that HL-1 cells form a syncytium, the signals propagate geometrically along the tissue (see Section 2.4.2.2 for details). Since measuring of all the devices per chip is done simultaneously via the specially fabricated multichannel measurement system (see Section 3.3.4 and Figure 5.14c) and controlled by the LabView–based software (Figure 5.14d), it is possible to post-process the recorded signals in order to locate the pacemaker cell position as well as to calculate the signal propagation velocity.

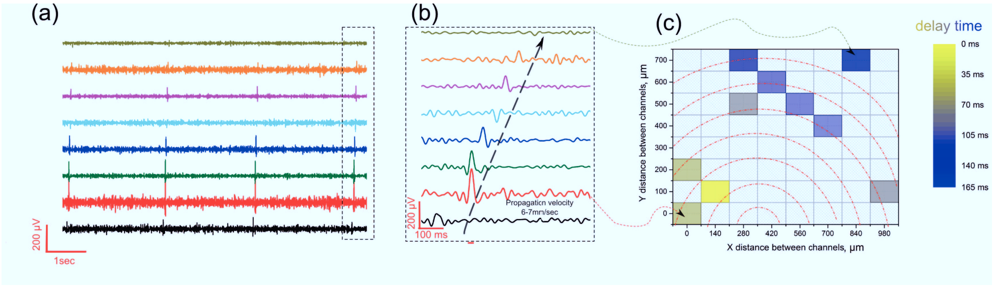

Figure 5.16: The *in vitro* recordings from sapphire-based GFETs: (a) Eight seconds long time traces of 8 channels with recorded APs. (b) A zoom-in into one of the APs, signal delay between the channels means that signal propagates through the chip. (c) The heat plot of the signal propagation, considering the geometrical locations of the recorded channels.

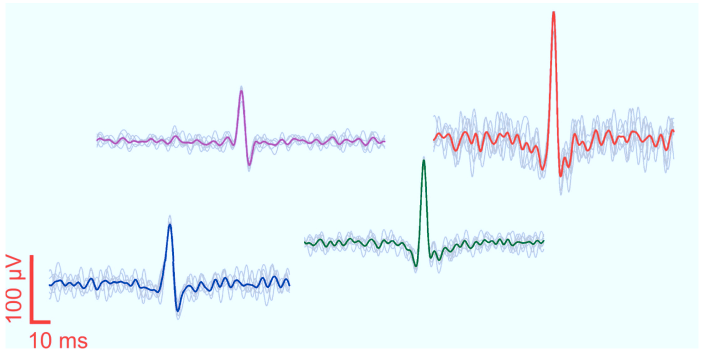

Figure 5.17: APs from 4 different channels (correspondingly to red, green, blue and magenta time traces in Figure 5.16a-b) are shown in gray with the averaged signal as an overlay.

With the sapphire-based GFETs we have been able to record the cellular activity from several channels (devices) on a chip. Some of the timetraces are plotted in Figure 5.16a. If zoomed into one of the APs (Figure 5.16b), the time delay between different channels is visible. Which means that the signal is propagating through the cellular layer on top of the chip. Considering that over 10 channels per chip have recorded action potentials, we calculated the spatial propagation of the signal (Figure 5.16c). We extrapolated the pacemaker's location to the middle bottom of the chip. The signal propagates radially, which would be more visible if more working devices picked-up the signals. The signal propagation velocity (upper bound) is estimated to be around 6–7 mm/s, which is in satisfactory agreement with literature values [45, 101, 152].

The signal-to-noise ratio (SNR) of the recorded potentials varies from a GFET to a GFET and spans from 4 (the best one) to 1.5 (hardly visible). The noise is considered here and in the following as 2×median absolute deviation (MAD, see Appendix G for discussion). The differences in the SNR and in the signal shape (Figure 5.17) can be attributed to the difference in the transconductance values for different GFETs on a single chip, as described above, and the quality of sealing between a cell and a device. Whereas the first parameter can be controlled via a more robust and fault–free fabrication procedure, the second one can only be addressed with the type of cellular culture, surface treatment of the device for cell adhesion, etc [100].

In order to prove the biological origin of the signals, another experiment was performed on a similar sapphire–based GFET chip (Figure 5.18). While recording the time traces from the chip, norepinephrine (NorA), a well-known drug for heart rate stimulation, is added to the medium. Increase of the NorA concentration from 0.1 mM to 0.2–0.3 mM in the medium, doubles the beating frequency (Figure 5.18 insets), as expected [153]. After that, a concentrated sodium dodecyl sulfate (SDS, a surfactant) solution was added to the same culture. The SDS perforates the cellular layer and removes it from the chip's surface. This results in frequent but evanescent beatings which disappear completely after a couple of minutes.

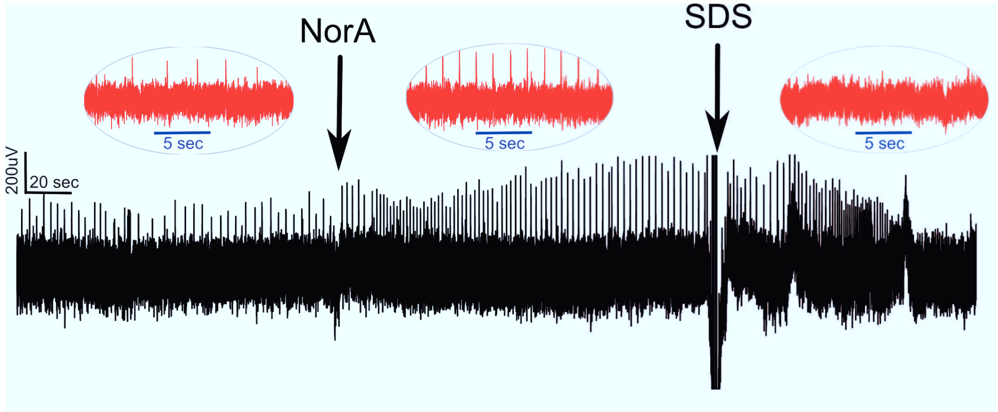

Figure 5.18: Raw recording, over 10 minutes long, from another culture where initially APs are seen firing at a frequency of ∼ 0.3 Hz (first inset), whereas addition of NorA into the culture medium almost doubles the frequency (∼ 0.5 Hz, second inset), and SDS starts to perforate and dissolve the cellular layer, decreasing the amplitude and eventually ceasing the APs (third inset). All three insets are 20 seconds long and have the same y–scale.

5.1.3.2 Heart Tissue

Following, an embryonic heart tissue is placed right on top of the chip's surface (see Figure 5.19a). A Ag/AgCl pellet electrode is placed as close to the tissue as possible in order to provide a stable potential through a low amount of ionic solution (supplementary medium). The timetrace recording from one of the channels (GFETs) is presented at Figure 5.19b showing repetitive spikes up to 7 mV with a rate of 30-40 beats per minute (bpm). When the action potentials (APs) from one channel are extracted and averaged, they result in a very nice shape with visible Q, R, S and slight T regions of a typical electrocardiogram (Figure 5.19c). The heart tissue measurements show an excellent applicability of the GFETs for *ex vivo* bioelectronics. The overall signal-to-noise ratio (SNR) of the measurements is up to 14, considering noise as twice the MAD.

5.1.3.3 Neuronal Networks

Further, cortical neurons are cultured on top of the chips (details are given in Appendix H) with an approximate density of 1500 cells/mm^2. The neuronal network is cultured and grown until mature: usually after DIV14 the cultured neurons produce spontaneous

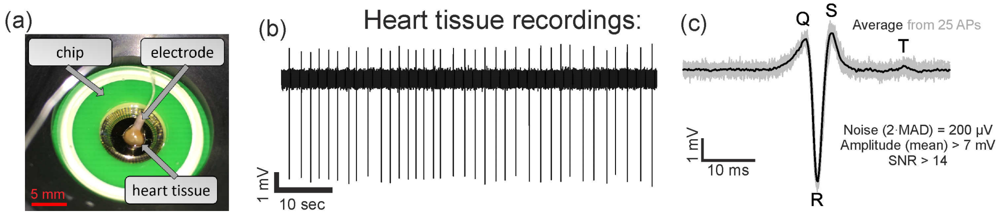

Figure 5.19: (a) A photograph of the heart tissue on top of the chip's surface while recording. (b) The time trace from one of the GFETs showing larger (up to 7–8 mVamplitude) and frequent (0.3–0.4Hz) APs. (c) The averaged AP with visible Q, R, S and T modes.

and large amplitude action potentials which propagate through the network. As expected, neuronal extracellular action potentials are one to two orders of magnitude smaller than that of heart tissue [6]. Nevertheless, we were able to record the APs and even bursting activities of a neuronal network grown on the GFETs array (see Figure 5.20a). The DIC and live-dead fluorescence images of the cell culture after recordings can be seen in Figures 5.20c-d. Such neuronal bursting activity recordings on graphene transistors are reported for the first time as up to our knowledge. The overall timetrace of almost five minutes in duration is shown in Figure 5.20e, showing that after cleaning the cells with Terg-A-Zyme (pink timetrace in Figure 5.20e), no APs are visible. The averaged action potential ($n = 77$) is presented at Figure 5.20b, showing the average amplitude around 630 μV. The noise, calculated as 2×MAD results in the value of 200 μV. Therefore the resulting signal to noise ratio (SNR) is above 3. Important to consider that in all our SNR measurements we use 2×MAD value instead of root mean square (RMS) value used for the noise consideration and no additional filters (only a 50 Hz filter) applied to the recordings (see Appendix G for discussion). An appropriate filter and RMS value usage would result in the SNR estimation up to 10 for neuronal recordings, 20 for HL-1s and 40 for the heart tissue.

Understanding the shape and amplitude of the recorded neuronal action potentials is a complex task, considering that different parts of a neuronal networks produce different kinds of potentials [154]. Moreover, the final signal shape depends on the signal transport from a cellular membrane to a transistor. Here the important factor is so-called cell–chip coupling [100]. Since the cells are a living organism, the coupling might be different from culture to culture and from chip to a chip [31,100,149,151,155]. Nevertheless, our neuronal recordings of graphene transistors are in a good accordance with the previously published data [141].

5.1.3.4 Passivation geometry for improved neuronal interfacing

A discussion we would like to address at the end of the work is importance of the passivation. We believe that using the new passivation technique, "feedline follower" helps to create a

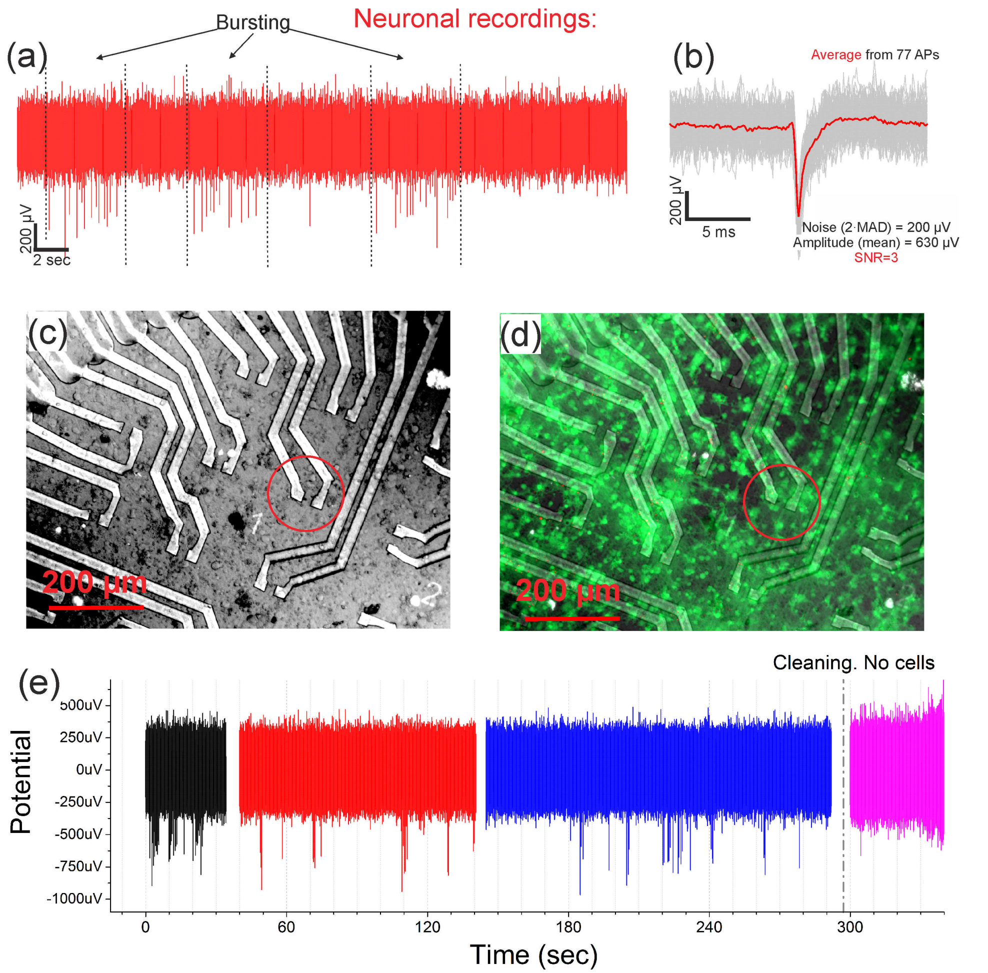

Figure 5.20: (a)The timetrace of a neuronal recording with inherent neuronal feature of bursting, when the neurons fire the action potential during several seconds, then stop for a while, and burst again. (b) The averaged AP (red) from 77 individual APs (gray) from the timeseries. (c) and (d) are the DIC and live-dead images of the chips. In red circle depicted the graphene channel which had recorded the neuronal action potentials. In the live-dead image it is visible that a bundle of the neurites are going through the graphene area of the GFET. In (e) is given the adjusted timetrace of the recordings. First three recordings (black, red and blue) are consecutive and around 5 minutes long in total. The last part of the timetrace is recorded after the chip was cleaned (Terg-A-Zyme overnight, see Appendix G) in order to eliminate any passive influence. Indeed after the cleaning no APs are visible.

better interface between graphene and neuron (Figure 5.21). While in a case of “openings”, which is up to now is the most common kind of passivation, HL-1s form a full cover of the passivation opening, so even if the gap distance from cell to device is large the volume is sealed. Since neurons do not cover the entire passivation opening the large gap distance is compounded by unsealed areas at the cell edges. The feedline follower passivation prevents membrane bending stresses as the cell approaches the graphene and therefore reduces the gap distance between the neuron and the gate (Figure 5.21).

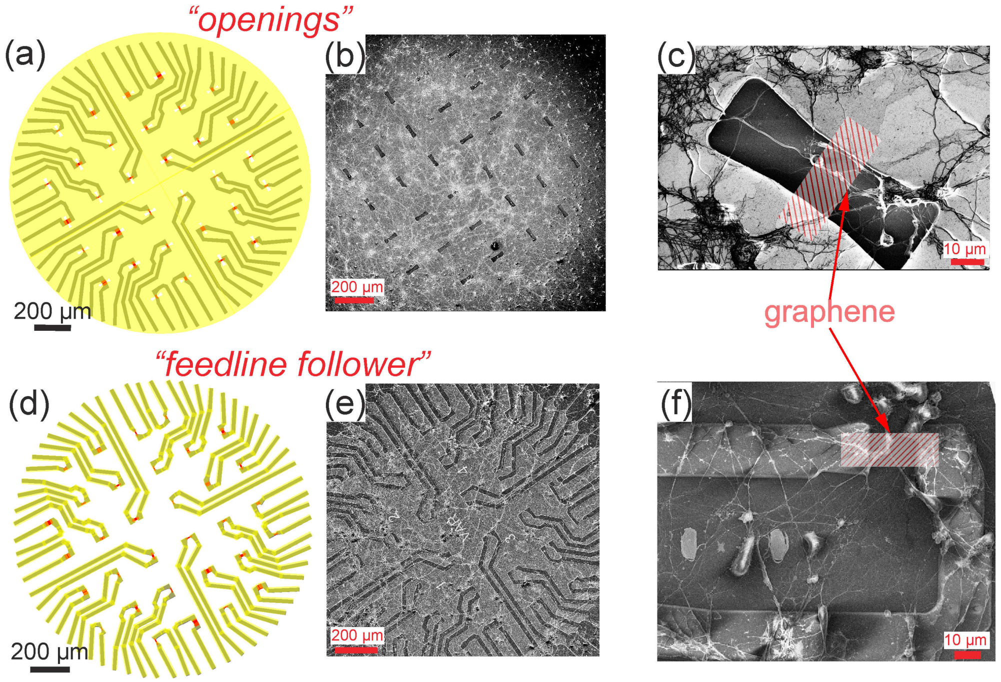

Figure 5.21: (a) and (d) represent the passivation openings and feedline follower passivation routines, respectively. The passivation is shown in yellow, openings/substrate in white, and graphene in red. (b) and (e) represent SEM images of a these kinds of chips with a neuronal network cultured on top and zoom-ins into one GFET area are given in (c) and (f). Details on fixation and imaging are given in Section 3.4.5. Due to sputtered layer of Pt (required to visualize non-conducting neurons and dielectrics), graphene is not visible. In (b) and (c), due to a large layer of passivation, the openings look dark in the SEM image, while opposite situation in (e) and (f), where passivation covers the metal feedlines and represented darker.

The most common way of passivating the transistors for bioelectronics consists of covering the whole chip's surface except the active area (Figure 5.21). In this work we focused on a new kind of passivation, which we call "feedline follower", where the passivation covers only the area over the metallic feedlines. Whilst the former type of the passivation has been in use and been proven to be important to create the seal and therefore increase the sensitivity [13]. However, the openings might be useful for recording from such cells, like HL-1s [25], which form a large confluent layer all-over the surface [156]. Neuronal networks, in opposite, do not form confluency, but try to grow a large network of neurites. The cell body sizes of neurons are much smaller than the openings themselves. The "feedline follower" passivation seems to be optimal for neuronal interfacing, as discussed later in this Chapter (See Figure 5.22 for more SEM images).

Moreover, there is always a trade-off between low-noise recording interface and good cell–sensor coupling. Considering that the GFET's multichannel measurement set-up exhibit already large noise, we can't afford to increase the noise even larger by creating bad sealing. At the same time, graphene is a purely two–dimensional material and it is important to bring the cell body as close to the graphene's surface as possible. We believe that such new passivation is more suitable for the graphene–based devices, since the neuronal culture then prefers to grow on the chip's surface.

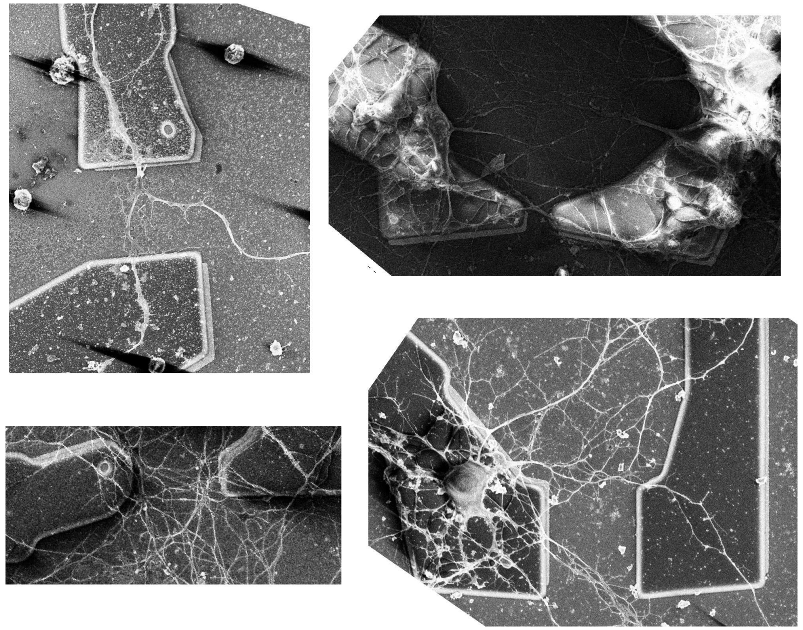

Figure 5.22: More SEM images of the neuron growing on top of "feedline follower" passivated GFET chips.

5.1.4 Summary

In conclusion, we compare the performance of the GFETs, fabricated on different substrates (SiO_2/Si, HfO_2, sapphire, and polyimide), with different (single/two side) contacts, and in liquid environment with different ionic strength. Normalized transconductance is found to be the most relevant and comparable value for the characterization of the liquid-gated GFETs. Interestingly, we did not observe a clear difference for GFETs fabricated on different substrates. Fabrication scheme with double contacting the graphene decreases the transfer length and contact resistance, however does not improve the overall transconductance of the GFETs. Heart tissue action potentials, recorded *ex vivo*, HL-1 and neuronal APs, recorded *in vitro* prove the excellent match of graphene transistors and bioelectronics. Polyimide substrate provides promises towards flexible devices and further *in vivo* recordings.

5.2 Flexible GFETs

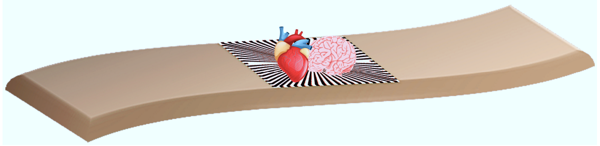

In this part of the thesis, the graphene field effect transistors (GFETs) are fabricated on controllably flexible polyimide-on-steel (PIonS) substrates, and their performance is compared to those reported previously. Polyimide (PI), a flexible and biocompatible polymer, is being widely used as a substrate in biosensing applications due to its great properties. The robust structure, chemical, mechanical and biological stability [54], and absence of dangling bonds make it a great substrate for interfacing with graphene. Our analysis, showing that the PIonS based GFETs exhibit performance, better than SiO_2/Si.

5.2.1 Fabrication

The PIonS substrates are fabricated by spin-coating two thick layers of polyimide (PI 2611) on top of a steel substrate, followed by baking at 350°C for complete imidization. The double PI layer is required to reduce the surface roughness. The final PI thickness is approximately 10 µm. Following fabrication steps, including graphene transfer, etching, metallization and passivation are performed as explained is Section 5.1.1 and detailed description is given in Appendix B of this thesis. However, in this case, the fabrication is done not on a wafer-scale, but on a chip-scale.

5.2.2 Characterization

The PIonS-based devices are initially measured at the probe station in order to get the I-V characteristics. The behavior of these devices is similar to others, reported above. Following the characterization, the I-V curves are derived in order to find the values of maximum transconductance. Notably, as usual for all of our devices, the hole conductivity and transconductance are usually slightly larger than that of electrons. This feature is of special interest for further *in vivo* applications, since it allows us to work with V_{GS} potentials close to 0V.

Solution gating and sensitivity The best PIonS-based device shows a transconductance value of 11 mS V^{-1}(1.1 mS, V_{DS}=100 mV, W=20 µm, L=3 µm, W/L=6.66), normalization to one square (one □ is when W/L=1, see Figure 5.10) results in 1.65 mS V^{-1} □. The device

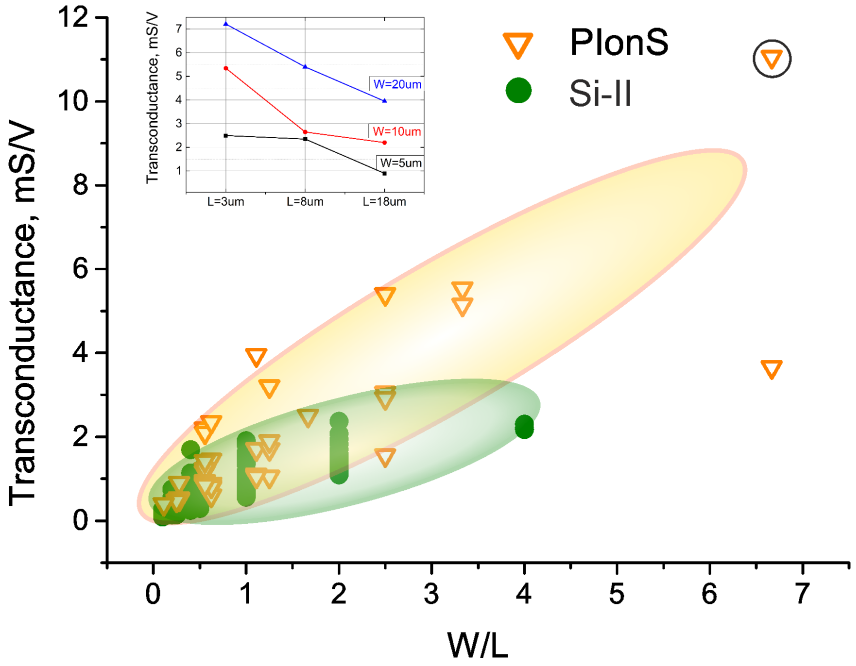

Figure 5.23: A comparison plot of the voltage normalized transconductance distribution for GFETs of different W/L ratios and substrates. Orange triangles represent the PIonS based GFETs, and green circles the GFETs from wafer Si-II. The semitransparent yellow and green ovals are given as eye guidelines to see the slopes. The black circle shows the largest value of 11 mS V^{-1} for a PIonS–based device. Inset: the plot of mean transconductance values for GFETs with constant width and different lengths.

is shown with a black circle in Figure 5.23. The linearized trend of all working PIonS GFETs ($n = 40$) gives an average value of 1.9±0.9 mS V^{-1} □. This is the highest transconductance values of liquid-gated GFETs ever reported. Peculiarly, the flexible devices show distinct improvement of their behavior compared to the rigid devices, which can be explained by the inertness of the polyimide surface [54,157] absence of dangling bonds and charge impurities, unlike in SiO_2/Si [158–161].

The SiO_2/Si and Sapphire-based GFETs are taken for comparison from the data reported previously (wafers “Si-II” and “Sap”, see section 5.1 for details). The silicon-based GFETs usually have a large distribution of the values, that could be attributed to the dangling bonds of the silicon dioxide itself [159], making the fabrication of the GFETs on SiO_2/Si substrates less reproducible than on sapphire or polyimide. This is the main problem with combining graphene and silicon technology, and the reason why we decided not to use the chips for further cellular measurements. The sapphire substrates usually show better performance than SiO_2/Si, mostly due to high thermal conductivity and high energy of polar optical phonons, therefore the substrate-limited mobility is much higher than in SiO_2/Si [162]. The best reported [45] sapphire-based GFETs transconductance value is 2 mS V^{-1} □.

Noise analysis There are many different parameters which can be used to describe the noise of a system, including values of voltage spectral density (S_V), current spectral density (S_I) [142] or their normalized values (S_V/V^2 or S_I/I^2) [44, 163]. Here, we focus on the S_I and S_I/I^2 noise spectra for PIonS and sapphire chips (see Figure 5.24a-b). The values are still difficult to compare. Another, more reliable and comparable parameter is the effective gate noise, calculated similarly to [44] and plotted in Figure 5.25b. The values, calculated for the frequency range from 1 Hz to 100 kHz, have a peak at the Dirac point due to the minima of the transconductance (Figure 5.25b). In order to provide a correct comparison, the further noise values are taken from the point of maximum transconductance in the p-doping regime. The position is marked as a star in the Figure 5.25a and Figure 5.25b. The value is in the range of 40 µV for PIonS devices and 25 µV for sapphire devices. The best reported sapphire-based devices [43, 45] show the effective gate noise value of 12 µV at a similar gate potential.

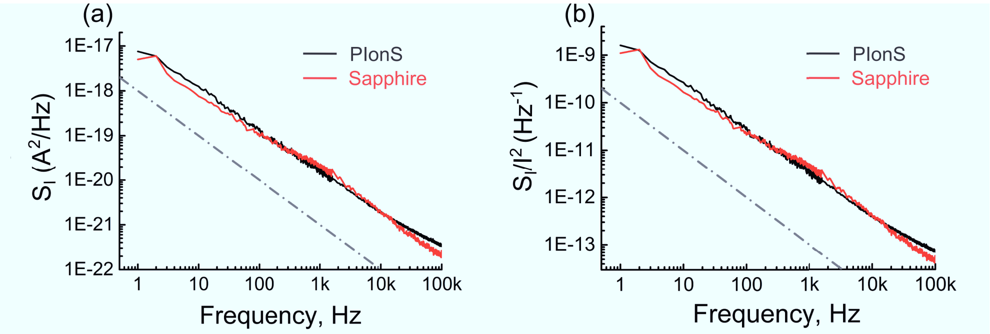

Figure 5.24: The exemplary noise power spectral density S_I (a) and S_I/I^2 (b) plots for a PIonS device (in black). The spectra are taken at the V_{gate} position marked as star in Figure 5.25. A gray dashed line is given as a 1/f guideline. W=20 µm, L= 10 µm for sapphire device and W=20 µm, L=8 µm for the PIonS device.

Bending In order to test the mechanical stability of the PIonS devices, we performed two kinds of bending tests. The first test consisted of a step-wise bending of the PIonS chip and concurrent measurement of the transfer curve at each bending angle (Figure 5.27). After a step of 500 µm, we measure the device and then continue bending, consequently measuring after each step. We found no significant changes in the R_D (resistance at the Dirac point) nor in the transconductance due to the bending.

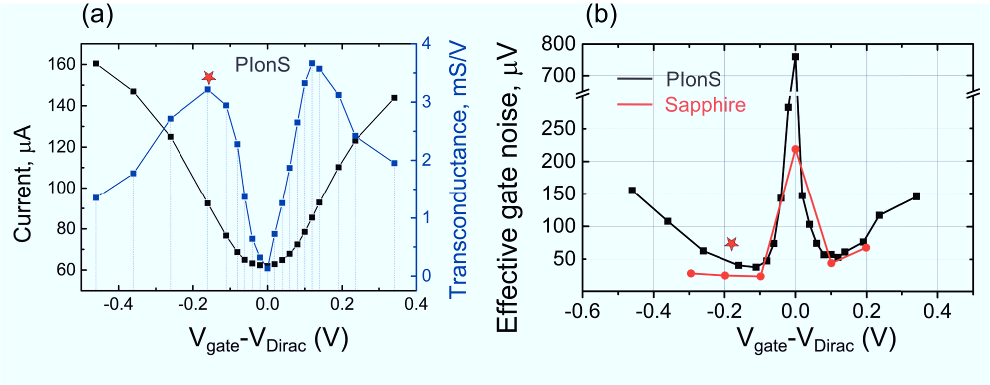

Figure 5.25: (a) The I-V curve of a PIonS GFET (black) and corresponding transconductance plot (blue). In (b) is the plot of effective gate noise; black for PIonS device, red for sapphire device. The distinct peaks at the Dirac point position are due to transconductance minima and are also regularly noted in other works [43, 44]. W=20 µm, L= 10 µm for sapphire device and W=20 µm, L=8 µm for the PIonS device. V_{Dirac} refers to the point of minimal current, i.e. Dirac point.

The second test was performed, continuously bending the chip for 10, 100, 300, and 1000 times up and down to the maximum tensile stress of 0.2%. The whole array of the GFETs is measured after each iteration. None of the GFETs, oriented perpendicular to the bending axis were broken or exhibited reduced performance. Nevertheless, some GFETs, oriented along the bending axis, got broken between the 300th and 1000th cycle. We speculate that this is the effect of the source-drain contacts to the graphene, since the tensile stress of 0.2% is not large enough to change internal properties of the graphene itself [135].

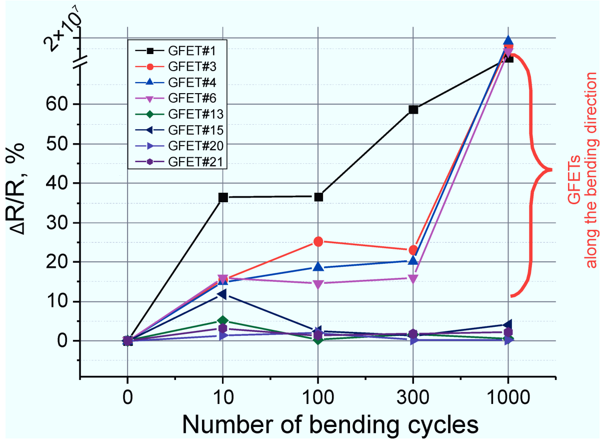

Figure 5.26: Plot of relative resistance ($\Delta R/R$) changes upon bending cycles for 8 GFETs, half of which are oriented along the bending axis.

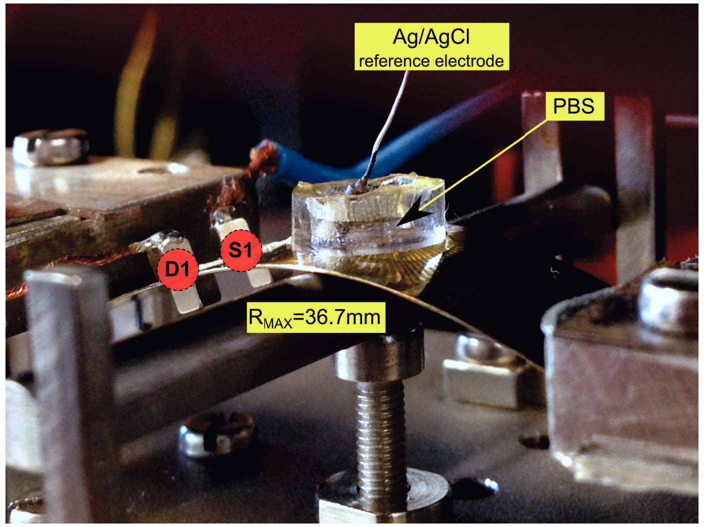

Figure 5.27: A picture of the bending set-up. The pushing rod is at its maximum height of 5 mm and total bending radius of 36.7 mm. S and D mark the conducting magnets, used for manual and stable connections while bending. PDMS ring works as the reservoir for the electrolyte solution, gated via Ag/AgCl pellet electrode.

5.2.3 Extracellular Measurements

5.2.3.1 Heart Tissue

As an intermediate step towards *in vivo* measurements, we performed *ex vivo* recordings of embryonic heart tissue (extracted from E18 Wistar rat, see details in Section 3.4.1) on a PIonS chip. The heart tissue was carefully placed directly in the middle of the chip (Figure 5.28a), source and drain were connected via conducting magnets, as described in the Appendix C. A Ag/AgCl pellet electrode is placed right on top of the tissue, and a large enough drop of electrolyte applied in order to transfer the gate potential, but small enough to not lift the tissue up from the surface.

The timeseries recordings, of almost two minutes long (see Figure 5.28b), show very remarkable peaks. The SNR of the measurement is estimated around 10.5±0.5, considering the 930 µV noise (estimated as 2×MAD, see Appendix G) and the cellular signal amplitude of 9.75 ± 0.5 mV. The peak's FWHM (Figure 5.28c) is 6–7 ms which corresponds to the ion-channel current and not to the mechanical movement [164]. The extremely large noise values can be attributed to the suboptimal connections on the PIonS chips, necessary to allow both bending and *ex vivo* measurements. In order to provide noise values comparable to devices on stiff substrates, the same device was used for a dummy time series recording with more stable needle contacts, the result is plotted in red in Figure 5.28b for comparison.

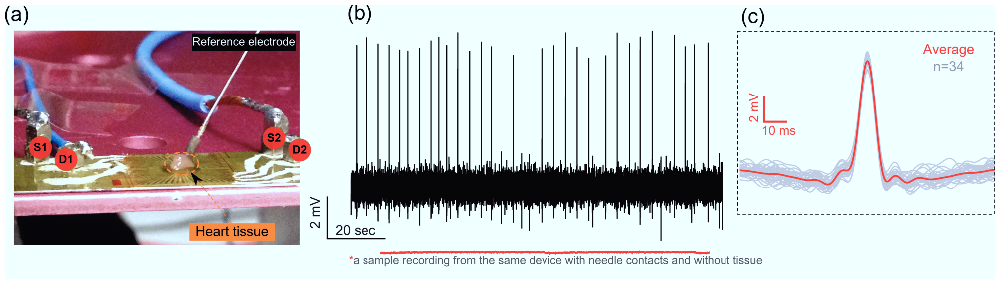

Figure 5.28: (a) A photo of the *ex vivo* experiment on the flexible and controllably bendable GFETs chip, with heart tissue right on top of the chip. (b) The heart tissue measurement time trace; the red line is a time trace of the same device but with needle contacts and measured at the shielded setup used for the noise characterization, without heart tissue. (c) The averaged (shown in red) action potentials ($n = 34$, shown in gray) from one recorded channel.

5.2.4 Summary

In summary, the controllably flexible, PIonS-based GFETs were fabricated and investigated for their performance. The PIonS-based GFETs exhibit an extremely large transconductance values, with an average of 1.9 ± 0.9 mS $\mathrm{V}^{-1}\,\square$ and mobility as high as 1750 $\mathrm{cm}^2\,\mathrm{V}^{-1}\,\mathrm{s}^{-1}$. Bending tests and *ex vivo* measurements prove the reliability of the devices. Releasing the underlying steel substrate would allow the devices to be easily implementable for *in vivo* applications. The combination of excellent transconductance values, combined with considerably low noise level, open up the road for *in vivo* applications of fully flexible GFETs on polyimide.

5.3 GFETs Conclusions and Outlook

In summary, several kinds of GFETs have been fabricated in the span of this thesis: from classical silicon and sapphire wafers to flexible polyimide. Performance of the GFETs has been studied in details and found new features, such as dependency of transconductance on the W/L ratio and electrochemical annealing.

The devices have been further used for *in vitro* monitoring of cardiomyocyte activity and exhibit SNR over 6. The controllably flexible PIonS-based GFETs exhibit an extremely large transconductance values, with average of 1.9±0.9 mS V^{-1} □ and mobility as high as 1750 cm^2 V^{-1} s^{-1}. Neuronal activity has been also recorded with the GFETs with a typical SNR of 3.

These experiments show that such devices fit perfectly into the field of *in vitro* measurements, drug–screening, and recording of action potential propagation, as described previously. Future devices envision the GFETs on PI without any metal support.

An overall comparison of our GFETs to the state-of-the-art is given in the Table 5.1.

Table 5.1: An overview of liquid gated graphene transistors used in literature.

	Graphene	**Substrate**	**Ionic solution**	**Ionic strength, mM**	**W**, μm	**L**, μm	**W/L**	g_m, μS	g_m, μS V^{-1}	$g_{m\ norm}$, μS V^{-1} □	μ_{max}, $\times 10^3$ cm^2 V^{-1} s^{-1}	V_{DS}, mV
Viera et al. [53]	CVD	SiO2	PBS	NA	75 75 75	6.25 12.5 25	12 6 3	1.25 0.75 0.5	6250 3750 2500	520 625 833	0.75 1.1 1.8	0.2 0.2 0.2
Cheng et al. [141]	CVD	PI	PBS	N/A	60	40	1.5	512	2560$^{d)}$	1705	N/A	200
Hess et al. [45]	CVD	Sapphire	PBS+NaCl	50	40	20	2	420	4200$^{d)}$	2100	1.7$^{d)}$	100
Dankerl et al. [44]	Exfoliated	SiC	PBS	N/A	40	20	2	46	460	230	0.4	100
Ohno et al. [146]	Exfoliated	SiO2	KHP	10	<10	<10	<2	36	N/A	>180 $^{a)}$	N/A	N/A
Blaschke et al. [147]	CVD	PI	PBS	5	20	10	2	400	4000	2000	N/A	100
Brown et al. [148]	CVD	SiO2	PBS+NaCl	10+100	40	40	1		4500	4500$^{c)}$	7$^{c)}$	N/A
This work 1 [52]	CVD	PIonS	PBS	100	20	3	6.66	1100	11000	1650$^{b)}$	1.75$^{d)}$	100
This work 2 [58]	CVD	SiO2 HfO2 PI Sapphire	PBS	0.16…1627	2-5-10-20	5-10-20	Varied	Varied	Varied	1600$^{b)}$ 1430$^{b)}$ 1340$^{b)}$ 1750$^{b)}$	0.8$^{b)}$ (2.0)$^{d)}$ 0.7$^{b)}$ (4.1)$^{d)}$ 0.7$^{b)}$ (4.5)$^{d)}$ 0.85$^{b)}$ (4.9)$^{d)}$	100

$^{a)}$ Calculated with assumption of $V_{DS} = 100$ mV; $^{b)}$ given the mean values only; $^{c)}$ Hall bar structure; $^{d)}$ given the maximum value recorded for one of the devices.

Chapter 6

GMEAs

Graphene multielectrode arrays (GMEAs), presented in this chapter are used for cardiac and neuronal recordings. The advantages of graphene as part of the multielectrode arrays are numerous: from a general flexibility and biocompatibility to the local transparency. The biocompatibility of the devices was shown via long-term culturing and measurements of both neuronal and HL-1 cell cultures. The action potentials have been recorded from HL-1 cells, neuronal cultures and *ex vivo* heart tissue.

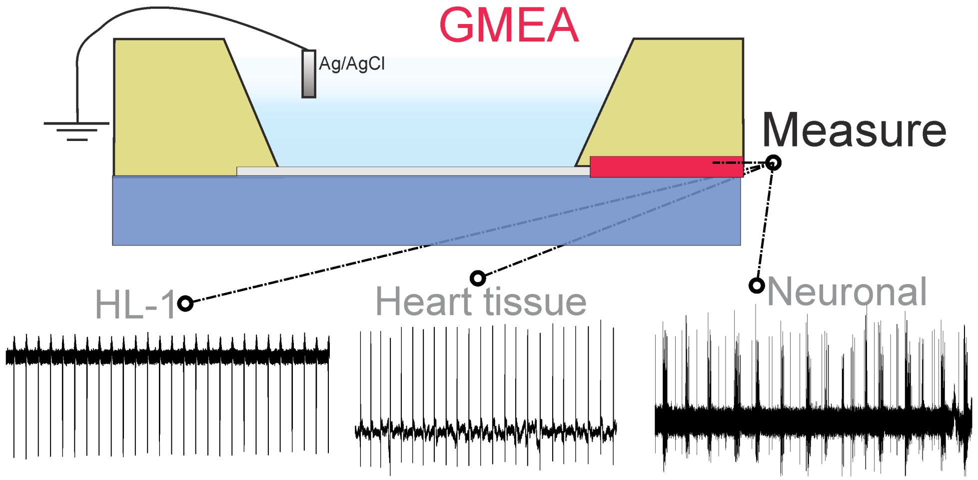

This chapter was reproduced in part from the following works:

1. **D. Kireev**, S. Seyock, J. Lewen, V. Maybeck, B. Wolfrum, and A. Offenhäusser. Graphene Multielectrode Arrays as a Versatile Tool for Extracellular Measurements. *Advanced Healthcare Materials* **2017**, 6, 1601433.
2. **D. Kireev**, S. Seyock, M. Ernst, V. Maybeck, B. Wolfrum and A. Offenhäusser. Versatile flexible graphene multielectrode arrays. *Biosensors* **2017**, 7, 1.

While the GFETs, presented in previous Chapter, require at least two feedlines per devices and a complicated read-out system, in the case of GMEAs, there is just one feedline per device is required. Moreover, the GMEAs are comparable easy in fabrication, characterization and use. Local the transparency of the GMEAs makes them a powerful tool for optogenetics, while general flexibility and biostability makes the GMEAs fundamentally interesting for *in vivo* sensors.

6.1 Rigid GMEAs

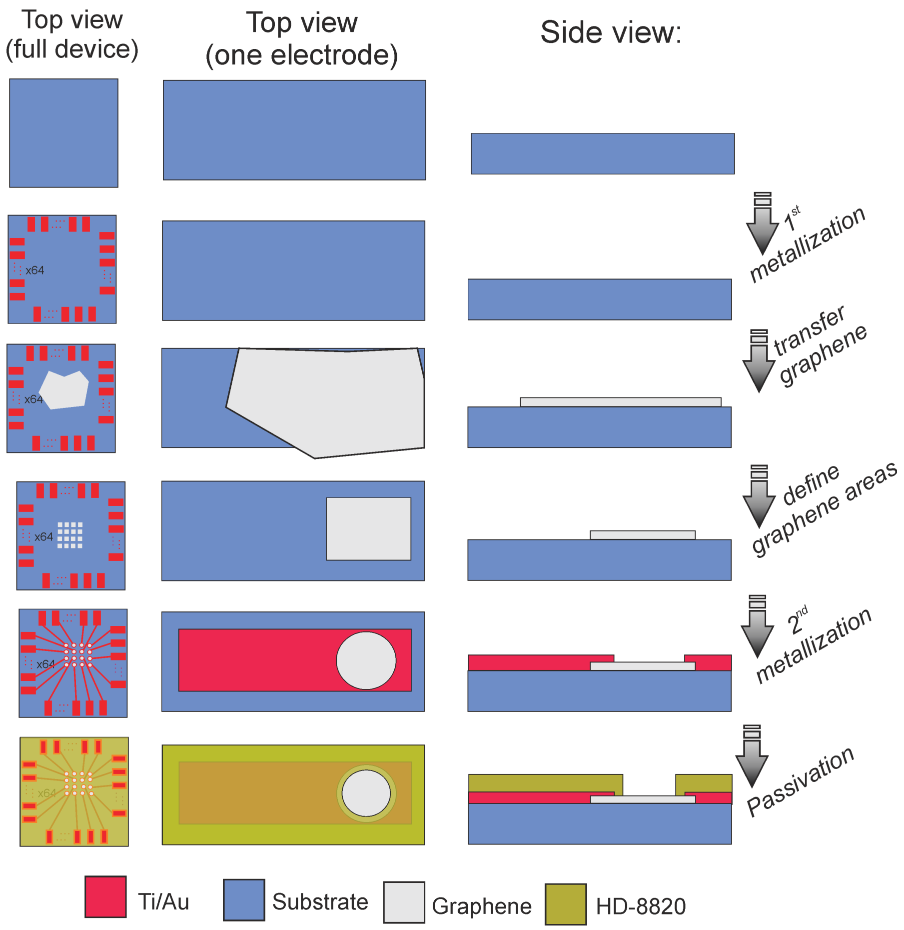

Figure 6.1: The overall fabrication flow of the rigid GMEA devices with a view of a whole chip, top view on one electrode and cross section of one electrode.

Planar microelectrode arrays (MEAs), which are nowadays standard, normally used for such purposes like drug screening, usually based on metals [10]. Gold, Titanium and Platinum are the most common electrode materials [15–17, 19]. Their performance was studied for decades, many modification in the compositions, topography and structure have been made [13]. Nevertheless there are two main disadvantages, which could never be filled by using the metals: non-transparency and inflexibility.

6.1.1 Fabrication

The graphene multielectrode arrays are fabricated on a 4-inch wafer using a CMOS-based technology. Borofloat glass and SiO_2/Si substrates were used for the device fabrication. Silicon-oxide wafers were used in order to allow an optical check of the fabrication steps, specially allowing visualization of graphene monolayers [165]. Borofloat wafers were used because of their transparency, which helps to monitor the cell cultures in a long term, as well as complements graphene's transparency.

The complete fabrication recipe is given in Appendix B, and schematically shown in Figure 6.2. The first metallization of Ti and Au was done in order to fabricate alignment markers. Further, the CVD grown graphene was transferred on the wafer by the high-throughput transfer technique described in Chapter 4. AZ-5214e photoresist was used for protecting graphene active areas while exposure to oxygen plasma (see Appendix A for details). The 10 nm Ti and 100 nm Au metallization stack was deposited via e-beam assisted evaporation on the wafer with pre-defined structure of LOR-3B and AZ nLOF-2020 photoresists. Photostructurable polyimide (HD-8820, HD Microsystems) was used as the last step of passivation. Spin-coated at 5000 rpm, soft-baked, exposed, developed and annealed with a slow ramp (see Appendix A for details), the polyimide forms a perfect, pinhole free, 3-4 μm thick passivation.

Each wafer results in 9 chips with an array of 64 electrodes, 24×24 mm^2 in size (see Figure 6.2a). In the middle 1.4×1.4 mm^2 area, 64 electrodes are arranged in eight rows and eight columns (see Figure 6.2b). From the 64 electrodes per chip, only 58 are graphene-based. Out of the 9 chips, four are with graphene electrode openings of 10 μm, and five with openings of 20 μm diameter. Photographs of the chips before and after encapsulation are given in the Figures 6.2d-e.

6.1.2 Characterization

The GMEAs were analyzed using impedance spectroscopy (see Figure 6.3). In comparison to gold electrodes (where 40 μF/cm^2 is expected [89]) of the same dimensions, the graphene-based electrodes exhibit slightly larger impedance: for 10 μm electrode openings, the interface capacitance is estimated to be 32 ± 1 pF ($\approx$31.4 pF for Au); for 20 μm is

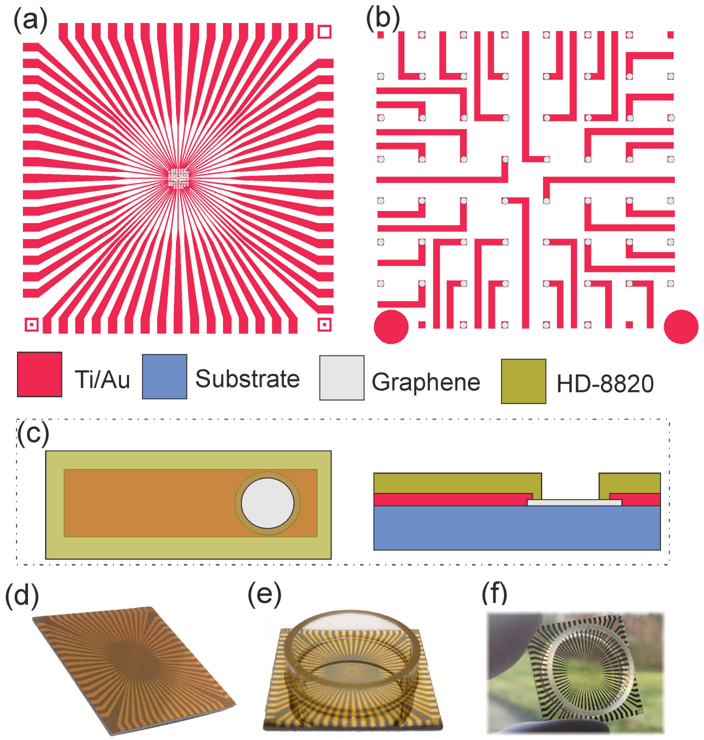

Figure 6.2: Fabrication overview. (a) The design of a GMEA chip, 24×24 mm^2 in size. (b) Zoom in into the GMEA array, of 1.4×1.4 mm^2 in size. (c) Top and side views on a schematics of one fabricated graphene electrode. (d) An optical image of a fabricated GMEA chip (Si-based). (e) An optical image of a Si-based GMEA chip after encapsulation. (f) An optical image of a borofloat-based GMEA chip after encapsulation.

around 104 ± 1 pF ($\approx$125.7 pF for Au). Parasitic effects through the passivation at 3 µm thickness would amount to approximately 8.5 pF that have to be subtracted from those values. As also seen from Figure 6.3, the impedance values are comparably large (3-4 MΩ at 1 kHz), however they are in the range of previously reported impedance values for graphene-based electrodes in the literature [46, 47].

6.1.3 Extracellular Measurements

6.1.3.1 HL-1

The chips, after encapsulation (see Appendix C), were used for monitoring the cellular activity. First, the HL-1 were cultured on top of the encapsulated chips (See Figure 6.4a). HL-1s were chosen since it is commonly used as a test culture: as cardiac cells, they grow fast (double their amount per day) and when reaching the mature state, usually at the

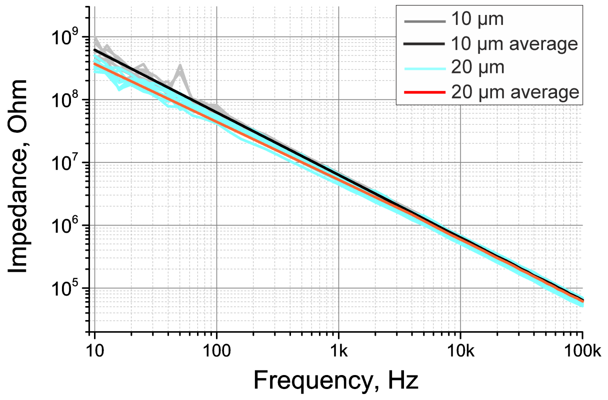

Figure 6.3: EIS data of the GMEAs of 10 (black) and 20 (red) µm diameter.

days *in vitro* (DIV) 3-4, depending on the amount of initial cells, they form a confluent layer (see Figure 6.4a). The HL-1 APs usually have a large amplitude, up to 1 mV (see Figure 6.4b).

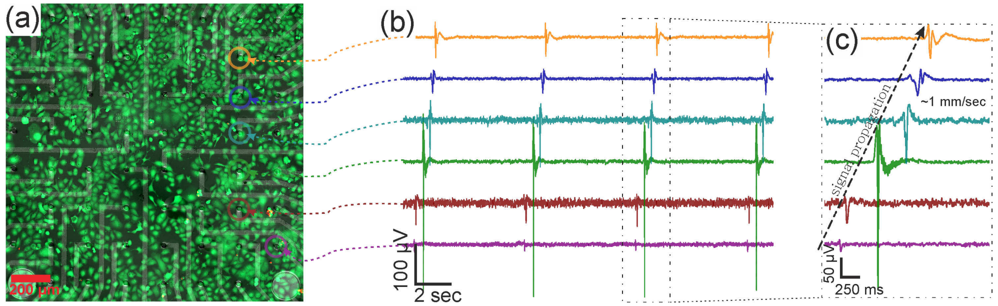

Figure 6.4: (a) A picture of calcein/ethidium homodimer stained HL-1 culture on the GMEA chips. Live cells fluoresce green, dead cells fluoresce red. (b) Timeseries recording from different channels from one GMEA chip, showing repetitiveness of the spikes and a clear propagation of the signal (time-delay between APs in different channels). (c) A zoom into one of the APs to see the spatial propagation of the AP between the channels.

The multichannel measurement set-up (as explained in details in Section 3.3.4) allows us to measure the signal propagation throughout the cell layer with large time resolution. An example of the signal propagation map is illustrated at the Figure 6.5, where the situation is rather complicated, and the signal is either propagates in U-shaped way or there are two separate pathways, which is also possible if there are two pacemakers per culture.

The recoded beating frequency is in the range of 1 ± 0.5 Hz, which is understandable since the value actually depends on such parameters as maturity of the culture, environment temperature and drug exposure. The recorded action potential amplitudes and their shapes vary from chip to chip (culture effect) and from electrode to electrode (sealing effect) [13].

Figure 6.5: A complicated HL-1 signal propagation map, showing that either the signal is propagating in a U-shape (possibly due to reduced or lack of gap junctions in the middle of the cell layer), see blue dotted path; or there are two pacemakers, depicted as two separate black solid paths. In the latter case, the boundary between the two beating regions is located the middle of the chip, and the left side has a signal flow top to bottom, while the right side flows from bottom to top.

Over 13000 HL-1 action potentials from 595 recorded timeseries were analyzed in order to compare them with the experimental and simulated data [13, 100, 147, 151, 152, 166, 167]. Regardless of the impedance of the electrode itself, there are other related physical and physiological parameters that affect the way the signal will be recorded and seen. First of all, the more mature the culture, the larger and more stable are the APs [168]. Second is the sealing: sealing between the cellular layer and the electrode is probable the most important factor to focus on [151].

For a comprehensive analysis and spike-sorting we analyzed the data from an overall of 104 timetraces. Each timetrace is a recording from one GMEA chip, consequently comprised of 64 channels. The overall number of culture–chip–electrode combinations (channels) with successfully recorded APs is 595. However, for further analysis we operate on the assumption that each culture-to-electrode coupling is not altered during the recording, and the signal shape is unchangeable. Therefore only 116 unique combinations (culture–chip–electrode) were selected for further spike shape analysis. The final shape distribution can be found in Figure 6.6b, with types A and B being the majority (see Appendix F for full spectrum of the spikes). Accordingly to previously simulated data [151], spikes of type A have a large seal resistance, large sodium peak and a large amplitude. The spikes of type A occurred almost in a third of the recorded APs. The differences in pre– and post–spikes, their amplitude and duration can be, in general, modeled by junction resistances and current flows of Na, Ca, and K ions [7, 150, 151]. Spikes of type B, C and D are not significantly different, and the variations of the absence/presence of the post and pre–spike overshoot can me described by difference in sealing, therefore some ion flow may be leaking, therefore not detectable. The last, type E, which occurred the rarest, has a very slow negative component, which, accordingly to [150] can be dominated by Ca^{2+} component of the action potential. The “other” types of spikes, mostly consist of a very uncertain shapes, like double or triple peaks, and usually are the result of a pinhole in the passivation or other defects.

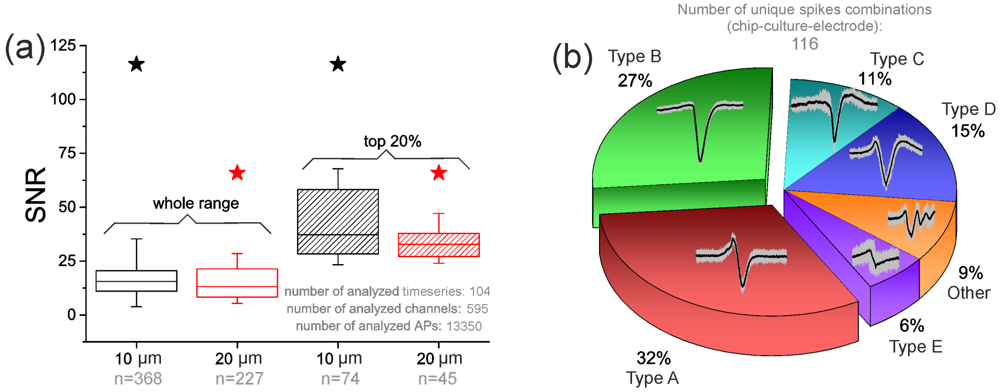

Figure 6.6: The result of analysis of over 13k recorded APs. In total, from 595 channels with recorded AP trains, 116 unique combinations (culture-chip-channel) were selected and the shape of the APs are analyzed. In (a) is given the statistics of SNR of the recordings with separated 10 and 20 µm channels, showing that in general there is no obvious difference between the devices, except if only top 20% of the APs are analyzed. Also, the max value of the SNR ratio is higher for the smaller devices. In (b) are given the frequency of appearance of each spike type.

Signal to nose ratios of the recordings were analyzed for each channel ($n = 595$). The noise values (twice the median average distribution, 2×MAD) were extracted for each channel, as well as action potentials were extracted and their average amplitude (peak–to–peak) values and were used for the calculations. After that, the data was grouped depending on the electrode diameter, and the statistical SNR values were calculated separately for small (10 µm) and large (20 µm) electrodes. The noise values for the two electrode types, surprisingly do not vary too much (10.26±4.8 µV for small and 10.7±7.2 µV for large electrodes) which could be attributed to the effect of quantum capacitance of the graphene [86,169]. Moreover, since CVD-grown graphene is multi-crystalline, there is a higher chance of having a grain boundary in the electrode opening for the large devices, resulting in a large variation in the impedance. Additionally, in the case of larger electrodes, there is a larger area of passive graphene, which is covered with protective passivation layer, providing additional passive resistance and noise.

The average SNR for 10 μm electrodes is 20±15, and for 20 μm electrodes is 17±10. The variation is very large, presumably due to variations in the culture and the coupling. In particular, we did not group detected APs according to the cell shape and position on the electrode. In order to present the performance in the best case scenario of coupling, culture health, and cell position, the top 20% of signals are presented in a separate analysis. These were selected by ranking taking the highest 20% of peak to peak AP values. The signal to noise ratio, selected in this way is still larger for the small electrodes (45±22), compared to 35±12 of large electrodes (See Figure 6.6a and Table 6.2). We attribute such behavior to the factor that a smaller electrode has a better chance of a good sealing, which results in a better SNR. For the small electrodes we have encountered a SNR up to 116, while the large electrodes do not exceed 65. We would like to point out, that no extra filters (except a 50 Hz comb filter) were applied to the recorded timetraces in order to keep the signal as undisturbed as possible.

6.1.3.2 Neuronal Networks

Further, embryonic cortical neurons were cultured with density of 800 cells/mm^2 (200×10^3 per chip (17.8 mm) $\approx$ 200000 cells/250 mm^2). The neurons were kept in the incubator (37°C, 5% CO_2) until the culture growth enough to form a strong network (Figure 6.7a). At DIV 21–25, the culture is mature enough to produce spontaneous electrical activity through the network. This is when the measurements were performed. The usual spontaneous spiking-bursting activity, recorded with our GMEA chips is visible in Figure 6.7b, where 8 channels from one chip picked-up the bursting activity, which propagates through the entire network. As introduced by Droge et al. in 1986, a criteria for defining bursting is the following: the interburst intervals should exceed the inter-spike intervals [170]. Different kinds of bursting patterns have been recorded, and can be found in Figures 6.12 and 6.13. In average the bursts happen every 5 to 15 seconds, depends on a culture, resulting in a small series of very high amplitude spikes (up to 800 μV) followed by a series of quickly evanescent spikes. The results are in a good accordance with the previously published data [4, 5, 20, 171–173]. In between the bursting, most of the channels have some non-bursting, random APs of smaller amplitude (50-150 μV, see Figure 6.8b,d).

It is difficult to follow the propagation of the neuronal signal in a comprehensive way, since the networks are complex and rather random, compared to the electrical syncytium of HL–1 cells. Moreover, the signal may pass through multiple neurons between two recording points. The signal delay is then a combination of the propagation velocity through a single neuron and the synaptic delay encountered each time the signal is transferred from cell to cell [95, 174]. In Figure 6.8a is shown a 70-second long timetrace from one channel with recorded spontaneous bursting-spiking activity, with bursting patterns happen every

∼10 seconds. Every such burst (Figure 6.8b) consists of three quick spikes with a large amplitude (up to 300 μV, see Figure 6.8c), followed by a series of quickly diminishing spikes. Following the definition, the recording in Figure 6.8a can be described as a regular bursting. In between the bursts, there are some other randomly bursting APs, see Figure 6.8b,d for examples. The patterns, as well as number and frequency of the bursting and non-bursting spikes vary from culture to culture. In Figure 6.9 are given four other averaged APs from another chip and another culture, representing two most common non-bursting AP shape. In the Figures 6.12 and 6.13 are given the variety of patterns recorded with the GMEAs.

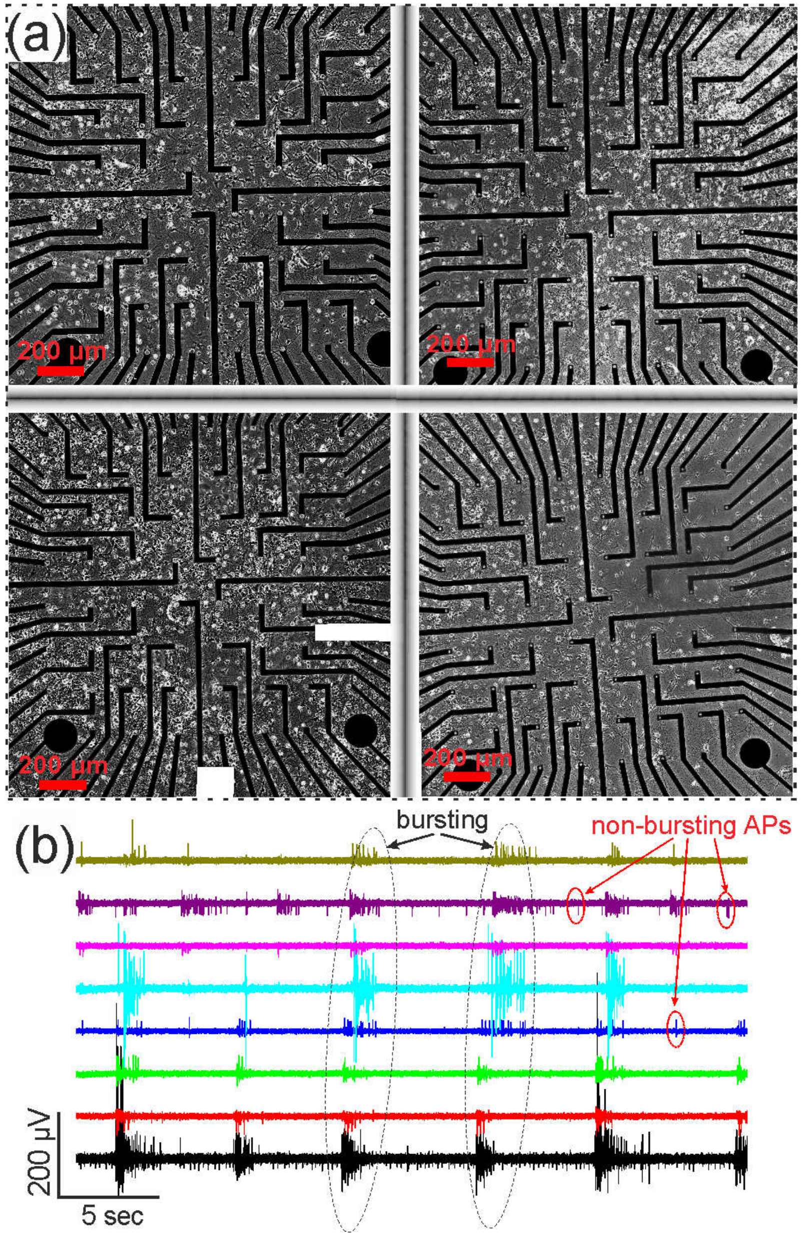

Figure 6.7: (a) Microscope panorama images of four different neuronal cultures on GMEA chips. (b) A timeseries recording showing excellent spiking-bursting activity on different channels.

The variations in the shape and amplitude of the recorded APs is much larger compared to HL-1 spikes [166, 175, 176]. This can be explained by the fact that now it is not only coupling and device performance that influence the recording, but also the morphology: it is important to distinguish between APs produced by a soma, neurite, axon, or their overlay (if the electrodes are larger than the measured organisms) [177]. Of course, the larger the electrode, the larger the chance to record something, but the smaller the ability to distinguish where the signal actually comes from.

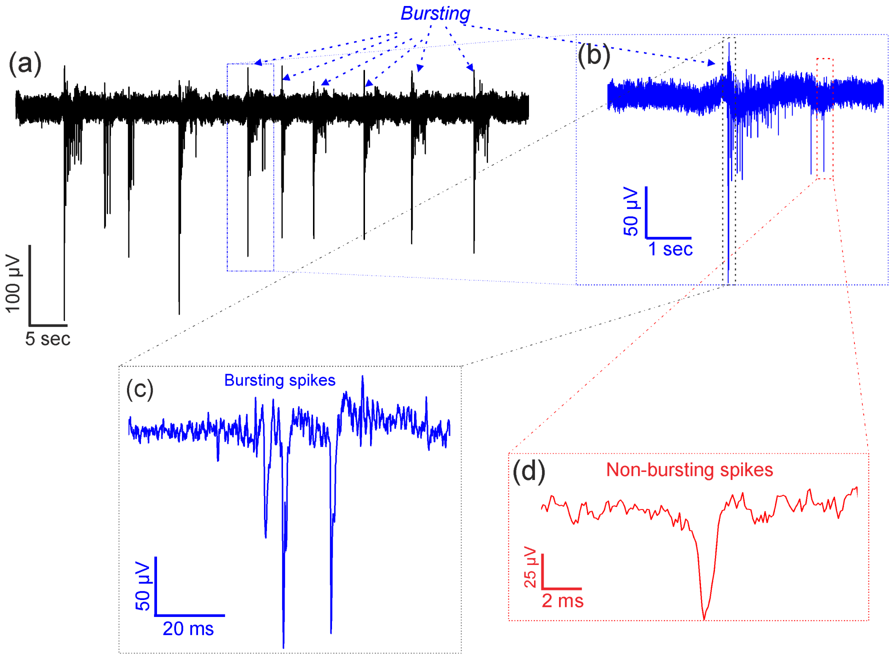

Figure 6.8: (a) A typical neuronal recording from a single channel, with clear repetitive spike-bursting activity; (b) is a zoom into one of the patterns, showing that each time there is a small number of very large spikes, consisting a burst (c), followed by a series of spikes with gradually decreased amplitude. In (d) is given a single non-bursting spike.

Lastly, in order to prove the biological origin of the signals, we have conducted a series of experiments. We treated the cultures on different chips with different chemicals, which, as suggested by literature can induce/reduce the firing rate or even kill the whole culture. Sodium dodecyl sulfate (SDS), potassium chloride (KCl), and tetrodotoxin (TTX) were used for this purpose. We would like to point out that the experiments were not performed as a specifically designed drug tests, but rather as a proof of principle that the GMEAs are able to record the effects and survive these treatments. The effect of the above-mentioned chemicals on neuronal culture was observed in real–time measurement of the GMEAs (see Figure 6.10). SDS, a surfactant, permeabilizes the cell membrane and dissolves cell material

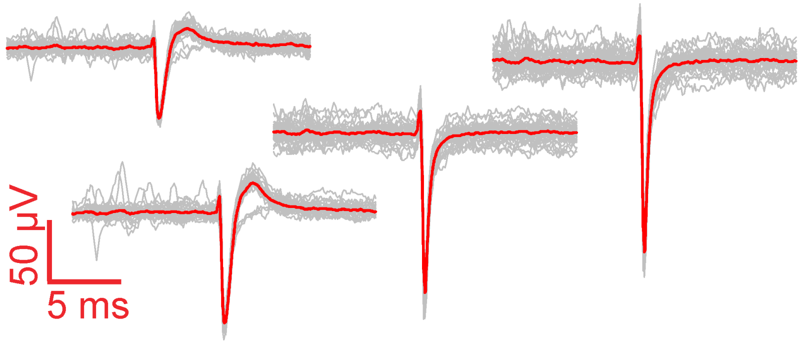

Figure 6.9: More non-bursting spikes, extracted (n=30 for each, gray lines) from other chip and other culture and averaged (red).

from the surface. Exchange (50%) of the supplemented medium with a saturated solution of SDS results in a fast (less than 20 seconds) and irreversible detachment of the cellular layer (see Figure 6.10a). In another culture, potassium chloride, was added to the medium to reach a final concentration of around 10–20 µM. This elevation of extracellular potassium concentration depolarizes the cell. Such concentration is enough to depolarize the cell above threshold and prevent re-polarization (see Figure 6.10b). This results in the cells firing and then remaining in the depolarization block. A fluorescent live-dead picture was taken afterwards showing that the cells survive this treatment (data not shown). TTX, on the other hand, is a neurotoxin which blocks voltage-gated sodium channels (Na_V). Upon addition to the cell culture, at the concentration of 0.7 µM, the APs amplitude, as well as their frequency slowly decrease as the toxin binds to more and more channels preventing their function, until no more signals are seen (Figure 6.10c). The effect is different in time for different channels, which shows complexity of the whole neuronal network (see Figure 6.11).

6.1.4 Summary

At the end I would like to point out two important issues. First, the same GMEAs were used to record several cultures of HL–1 cells (over 10, 3–4 DIV each) and several cortical neuronal cultures (over 5, 14–25 DIV each) with a cleaning step (in 1% Terg-A-Zyme, see Appendix H) in between. Quality of the electrodes does not seem to be deteriorated by the cultures or cleaning, proving the stability of the devices. Second, all the presented above values of SNR and APs were calculated using limited noise filtering. Only 50 Hz noise and its harmonics together with linear slopes were removed by post-processing. Further filtering can disturb the actual shapes of the potential, but theoretically can improve all SNR values by 30-40%.

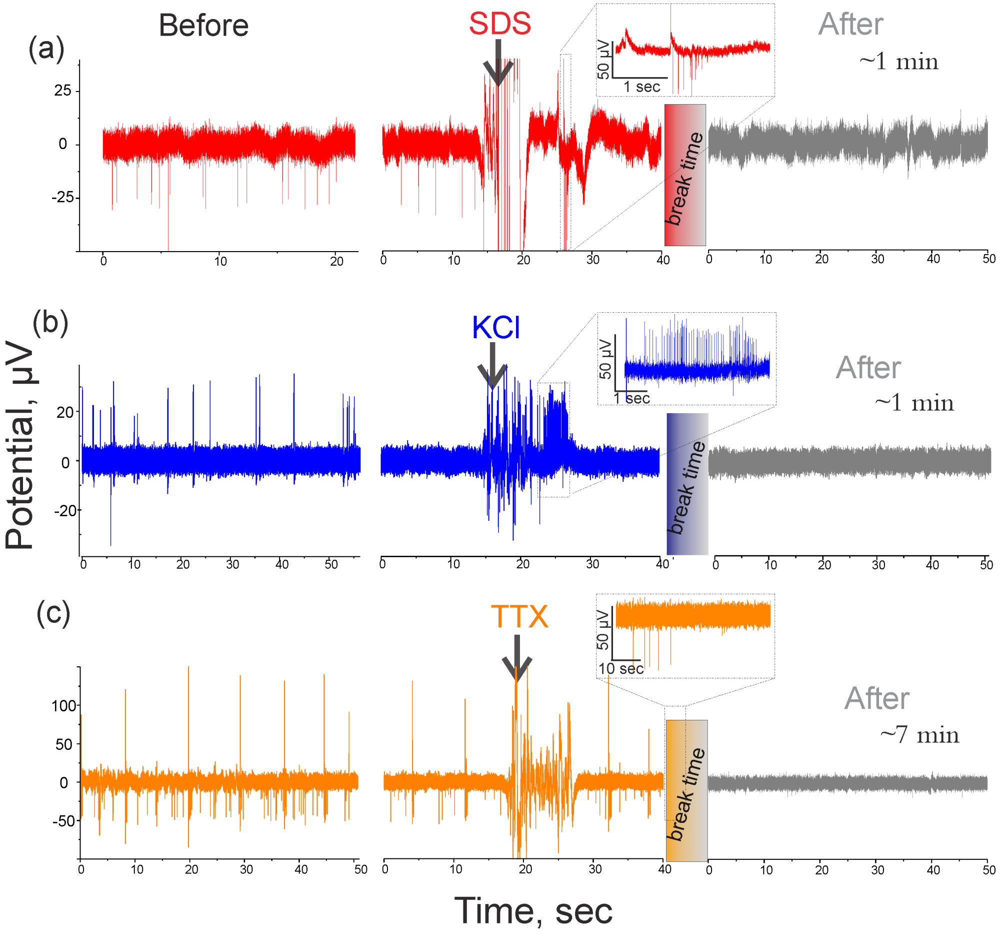

Figure 6.10: Chemical treatments of the neuronal networks with SDS (a), KCl (b) and TTX (c). The left panels are the recordings before any treatment. The right panels are recordings of one minute (for SDS and KCl), and 7 minutes (for TTX) after the treatments. In the middle are the 40 seconds of the timetraces when the chemical was added into the medium. Small insets show the immediate effects when the chemicals alter the normal neuronal bursting-spiking activity.

In summary, with the rigid GMEAs is it possible to detect HL-1 spikes with a great consistency and reliable SNR without any filtering. APs are nicely distinguishable for different cases of sealing. The spontaneous neuronal action potentials can also be nicely recorded with the GMEAs, and the measured APs are in a good accordance with the results observed by the other group [178].

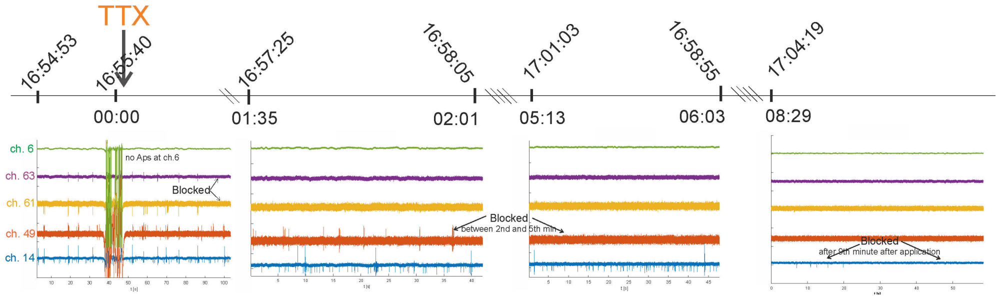

Figure 6.11: Full arrangement of the timetraces recordings from one experiment with the addition of TTX. In the first graph, approximately 40 seconds from the beginning of the recordings, TTX was added to a final concentration around 0.7 µM. The moment when TTX was added is taken as a reference point. Approximately 40–50 seconds after the TTX addition, two channels (№61 and №63) had stopped firing action potentials. The neurons on channel №49 stop firing between the 2nd and 5th minute after TTX addition (no recording during this time). Interestingly, the spiking on channel №14 were dissaperaing very slowly: First the bursting frequency decreased, and the total spiking activity stops only after the 9th minute.

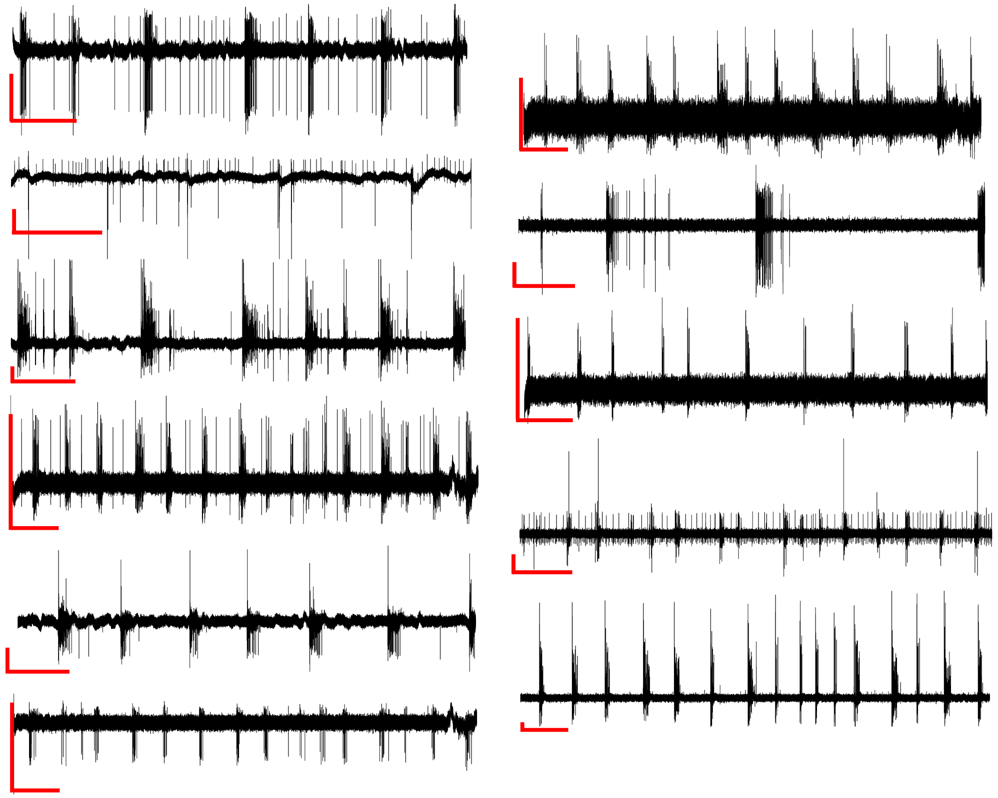

Figure 6.12: Some of the different patterns of bursting-spiking activity from neuronal networks recorded by the GMEAs. The scale bars given for each recording are 50 µV on the vertical and 10 sec on the horizontal.

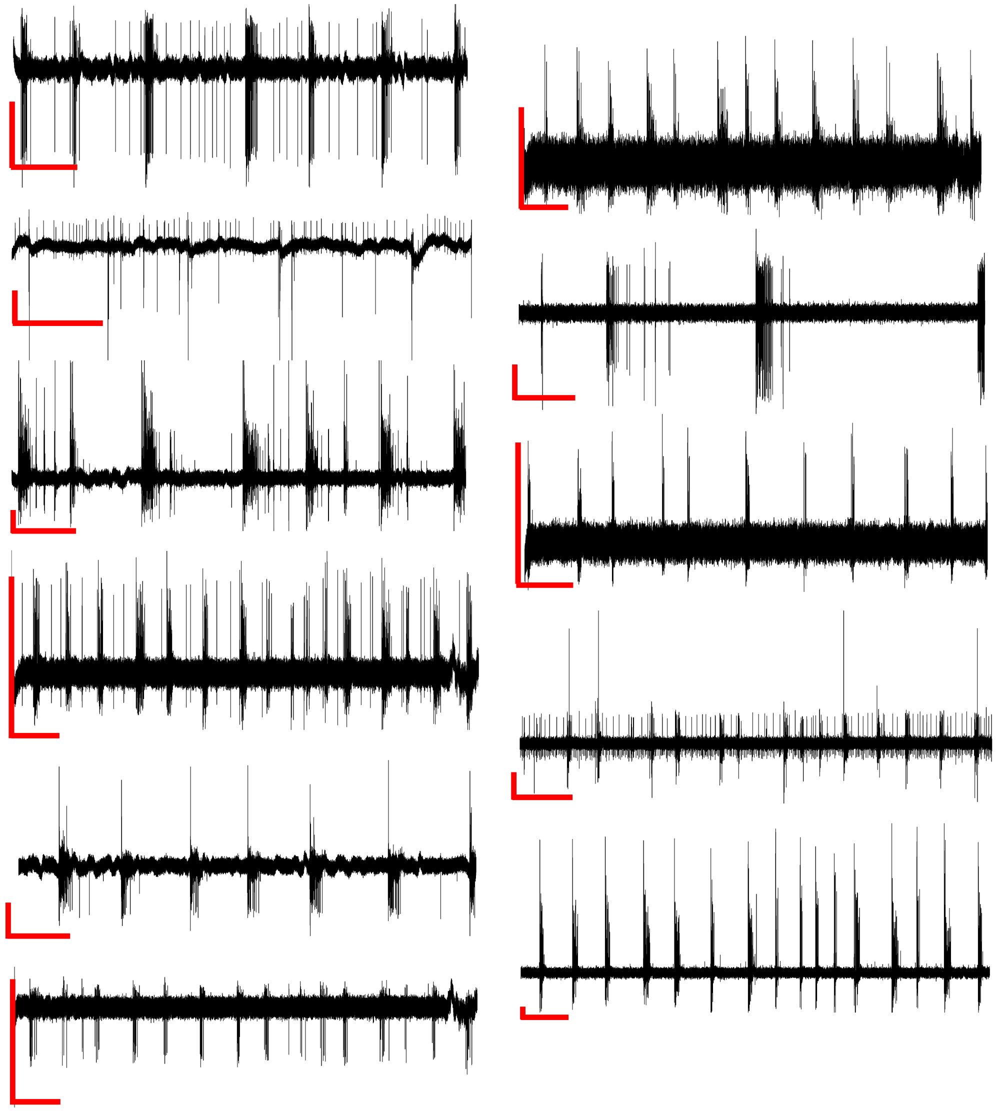

Figure 6.13: Some of the different patterns of bursting-spiking activity from neuronal networks recorded by the GMEAs. The scale bars given for each recording are 50 µV on the vertical and 10 sec on the horizontal axis.

6.2 Flexible GMEAs

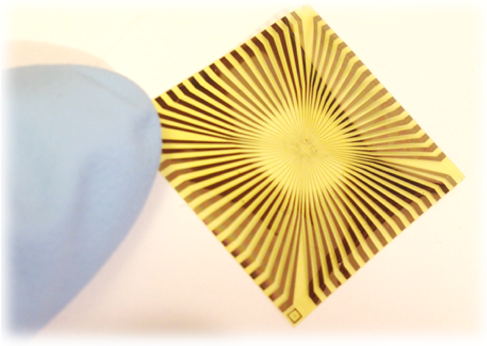

The combination of MEAs and flexible substrates has gained much attention recently, specifically when combined with carbon-based materials, like carbon nanotubes (CNT), which exhibit extreme performance and flexibility [179, 180]. Graphene, in this regard, also has many promising features, such as biocompatibility [49, 50], excellent electrical properties [63, 68], and intrinsic flexibility. Biocompatibility of the graphene used in this work was also studied specifically and it was shown that neurons prefer to grow on graphene. The details can be found in Appendix E of this thesis.

In this section of the thesis I describe fabrication of flexible and robust graphene-based microelectrode arrays on the biocompatible polyimide substrate. The devices, even after a severe mechanical deformations, were used for *in vitro* and *ex vivo* extracellular recordings multiple times, providing low noise and high signal-to-noise ratio recordings.

6.2.1 Fabrication

The graphene multielectrode arrays were fabricated using standard photolithography (see Figure 6.14 for the fabrication steps and Appendix B for details). In order to create a flexible chip, a sacrificial layer of Cr/Au/Cr (10/100/50 nm) was evaporated on top of a Si wafer prior to the fabrication. Then, two layers of PI-2611 (HD Microsystems) were spin-coated on top of the wafer to result in an approximately 10 μm thick polyimide film after the hard-bake (at 350°C). The following fabrication consisted of:

1. Evaporation of a metallization layer (Ti/Au, 10/50 nm) using a LOR-3B and AZ nLOF-2020 photoresist stack for lift off;
2. Graphene transfer, using a high-throughput technique (see Chapter 4);
3. Defining graphene areas using AZ-5214e photoresist and oxygen plasma (see details in Appendix A);

4. A second metallization to sandwich the graphene and provide a lower contact resistance;
5. A final passivation with photostructurable polyimide HD-8820, resulting in an approximately 3 μm thick layer;

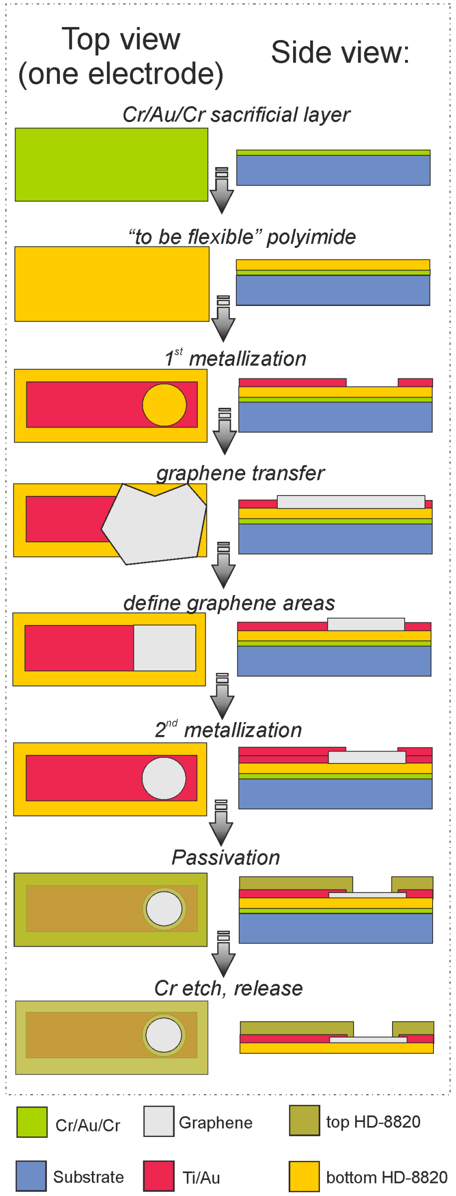

Figure 6.14: The flexible GMEAs fabrication flow.

After fabrication, the chips were immersed into chromium etchant for approximately 24 hours to remove the chromium sacrificial layer [25].

The fabricated devices are 24×24 mm^2 in size, and approximately 13 μm thick with a polyimide base and polyimide passivation. The chip's layout is the same as for rigid GMEAs (see Figures 6.2a-b with the feedlines aiming into the middle of the chip. The middle array of the chip (of 1.4×1.4 mm^2 in size, is where the metal feedlines have an opening and graphene underneath (see Figure 6.14). The passivation (polyimide) layer is developed in a way that only graphene parts are exposed to the liquid. The final GMEAs have circular recording apertures of 20 μm in diameter.

Once the devices are fabricated, the sacrificial layer is etched, releasing the flexible chips (see Figure 6.15b), which are further connected to a carrier for *in vitro* studies (see Figure 6.15). This is an important step towards stable characterization and cell culture measurements. Due to the flexibility of the devices, a standard measurement process would be difficult or even impossible to perform. Therefore the chips were soldered to a carrier, as shown in brief in Figure 6.15 fixes the chip on a carrier and helps to improve the *in vitro* compatibility of the devices and the long-term stability. The flexible chip is flattened on top of a glass slide (with a drop of ethanol for adhesion), see Figure 6.15c. Special carriers (see

Figure 6.15d) were prepared, with the inner contact pads matching the exact geometry of contact pads on the chip. The carrier was placed on a hotplate (180°C), and a soldering paste (42Sn/58Bi alloy) was dispersed around the contact pads. When the flux was evaporated and the excess alloy was removed, only small amounts of alloy were left on top of the carrier's contact pads. Afterwards, the flexible chip was simply placed on top of the carrier and aligned under the microscope (see Figure 6.15e). When cooled down, any remaining flux was removed in ethanol, and the back side of the chip was glued with medical epoxy (EPO-TEK 302–3M). Two glass rings were glued (with polydimethylsiloxane (PDMS)) on top of the chip to provide containment for *in vitro* and *ex vivo* tests (see Figure 6.15f). The suspended chip is not taut across the hole in the carrier and can still be mechanically deformed small distances. Robustness of the chips was tested by completely crumpling one of the chips prior to encapsulation (See Figure 6.18b).

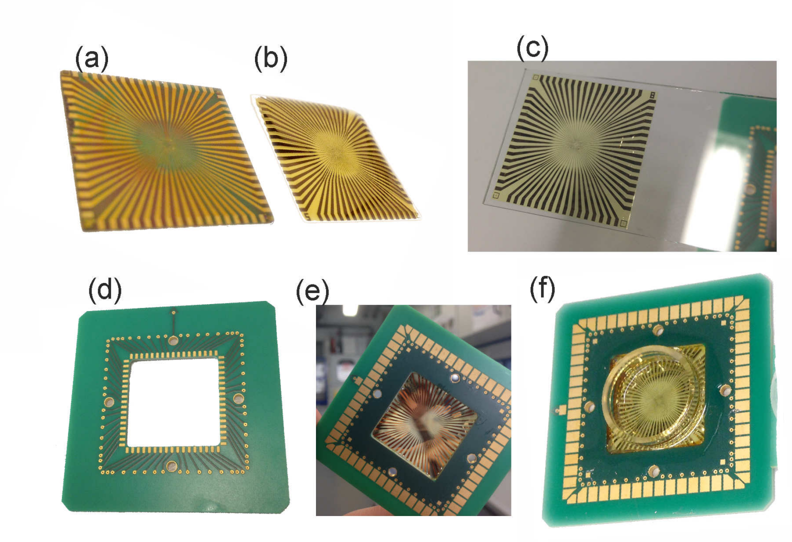

Figure 6.15: The Flexible GMEA bonding procedure. The as-fabricated chip (a) is dipped into Cr-etch solution, suspending the device (b). A drop of ethanol is applied on the glass slide in order to facilitate the capillary force to keep the device straight (c). A special alloy (see Appendix C for details) is applied on the contact pads of the carrier (d). When the chip and the carrier are glued/contacted via the solder paste (e), the chip is further sealed with epoxy and encapsulated with glass ring and PDMS (e).

6.2.2 Characterization

An exemplary electrical impedance spectroscopy bode plot from a GMEA is given in Figure 6.16. Impedance of the GMEAs, of 20 µm in diameter, measured at 1 kHz is around

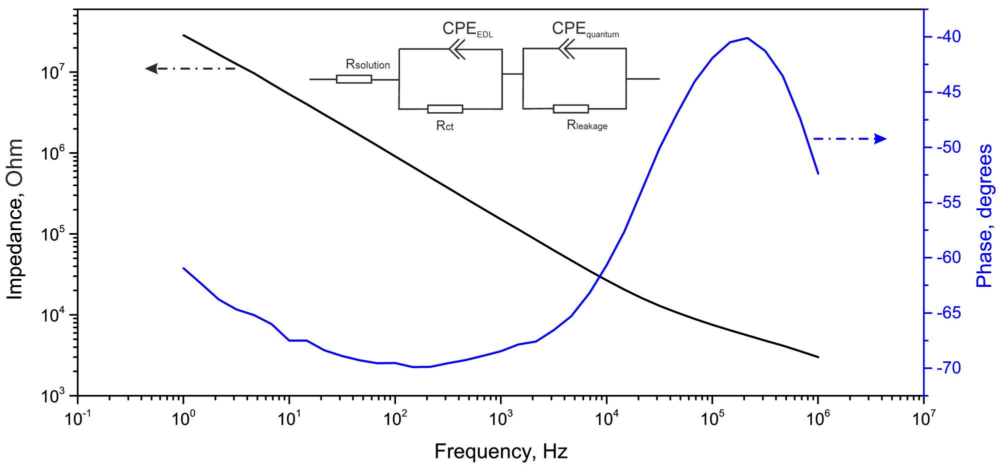

Figure 6.16: Bode plot of a GMEA, electrode diameter of 20 µm. A linear dependency of the impedance at lower frequencies is a typical graphene electrode behavior. The inset gives the model used for fitting the data.

$(1 \pm 0.5) \times 10^5\ \Omega$, which is in the range of previously reported values [46, 47, 169, 178]. In order to fit the GMEAs' behavior one has to consider another constant phase element (compared to metal electrodes), representing graphene's quantum capacitance [86,87,181]. The general equivalent circuit used in this thesis is shown in the inset of Figure 6.16. The two constant phase elements represent the electrical double layer and the quantum capacitance. In the previous works [46,178], a Warburg element was used to model a linear diffusion. However, in our case, the electrode diameter is too small to be described by linear diffusion, therefore the Warburg element is not used in our calculations. The used equivalent circuit fitting values are represented in Table 6.1 together with comparison to previously published works.

Table 6.1: Fitting results for EIS measurements and their comparison to previously published works.

	Used model	R_S (kΩ)	$C_{CPE\text{-}1}$ $(S \times s^n)$		R_S(Ω)	Z_W $(S \times s^{1/2})$	$C_{CPE\text{-}1}$ $(S \times s^n)$		R_L(Ω)	Area
			Q	n			Q	n		
This work [56]	$R_S + Q_2/R_2 + Q_3/R_3$	0.8	5.0×10^{-9}	0.68	5.8k	—	7.36×10^{-9}	0.78	140M	314 µm^2
Kuzum et al. [46]	$R_S + Q_2/(R_2 + W_2)$	—	5.6×10^{-9}	0.67	85M	17.36×10^{-9}	–	–	—	2500 µm^2
Du et al. [178]	$R_S + Q_2/(R_2 + W_2) + Q_3/R_3$	0.17	5.75×10^{-7}	0.67	3k	8.12×10^{-6}	5.55×10^{-7}	0.9	23.4M	7000 µm^2

6.2.3 Extracellular Measurements

6.2.3.1 Heart Tissue

Embryonic heart tissue, extracted as described in the Section 3.4, was placed on top of a GMEA chip. No adhesion promoter was used, but only a small drop of a supplemented medium (30 µL) is dispersed on top and around the tissue in order to provide physiological conditions. A Ag/AgCl reference electrode is placed on top of the liquid and as close to the tissue as possible to yield a stable reference potential. The heart's electrical activity is detected on more than 80% of all electrodes on the GMEA as shown in the spatial diagram (see Figure 6.17a). Shape of the recorded potentials (see an average APs in Figure 6.17b and 6.17c) clearly resembles the P, Q, R, S, and T regions of an electrocardiogram [164,182,183].

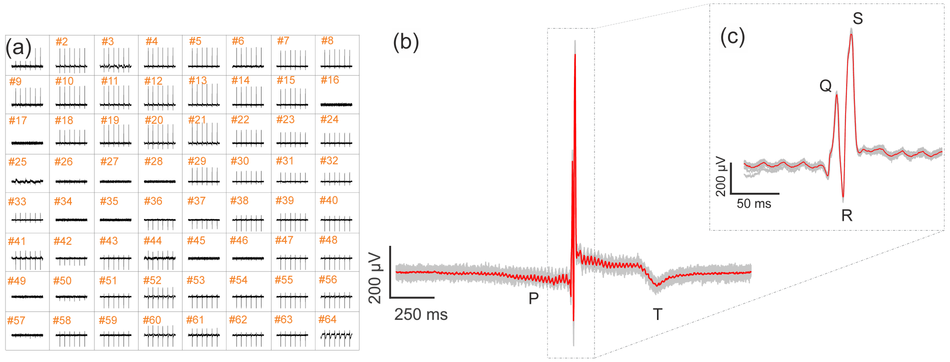

Figure 6.17: (a) The spatial resolution map of heart tissue recordings from a GMEA device. The distance between the electrodes is 200 µm in each direction. (b)-(c) The zoom-in into one action potential of 2 seconds and 200 ms long are given for a clear observation of P, Q, R, S and T regions.

The average heart tissue spike amplitudes recorded here are in the range of 1 ± 0.2 mV, while noise is in the range of 20 ± 6 µV(2×MAD, see Appendix G for discussion). The final signal-to-noise ratio (SNR) of the acute heart tissue recordings done by the flexible GMEAs, is in the range of 50 ± 15, which is comparable to previous work [164].

6.2.3.2 HL-1

Prior to the HL-1 cell culture, one of the GMEA chips was tested for its mechanical stability: the flexible chip was crumpled severely (see Figures 6.18a-b) before soldering. Nonetheless, the chip has been soldered and encapsulated with the same procedure as described in experimental section (see Figure 6.18c). HL-1 cells were plated, as described

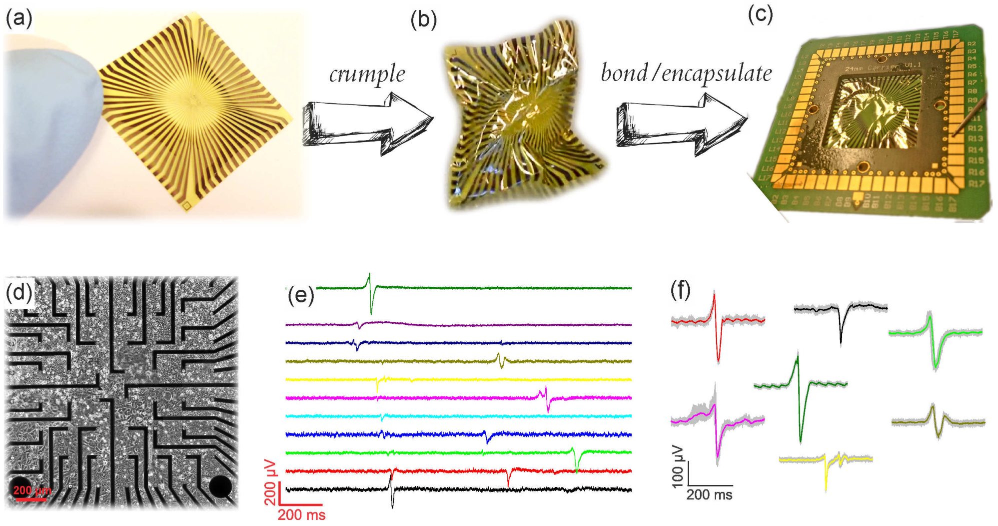

Figure 6.18: (a) One flexible chip, which was crumpled (b), then bonded and encapsulated (c). (d) A DIC picture of HL-1 cells grown on top of a GMEA surface. (e) Time trace recordings of HL-1 cells from eleven channels on one GMEA chip showing a time delay in recording of different electrodes that reflects spatial propagation. (f) The variety of different HL-1 action potential shapes recorded with the GMEA due to differences in cell–chip coupling.

in the experimental section, and incubated until confluent and contracting. As a cardiac muscle cell line, they tend to form a continuous layer while growing on a surface. An optical image of such a continuous cellular layer on top of a GMEA chip is shown in Figure 6.18d. Action potentials (APs), which can be described as a change in the cellular membrane potential, are produced repeatedly, continuously and through the whole layer. In Figure 6.18e, eleven traces recorded from different channels (electrodes) on the same chip are shown. The figure shows that there is a shift between the occurrences of the APs at different channels, which shows that the electrical signal propagates through the cellular layer [24]. As the signal is picked up by different electrodes with some time delay, it is evident that the spikes are not caused by noise or electronic artifacts. The AP's amplitude, width and shape can be different from channel to channel, but stays persistent in one channel. The main reason for different AP shapes is cell-chip coupling, which, in the case of HL-1 cells, is a more relevant parameter, compared to the above-reported heart tissue signals. While growing, HL-1s cells form a continuous layer of electrically active cells, connected via gap junctions [151, 184, 185]. Sizes of connected cell layers exceed millimeters and can be even centimeters if the monolayer is completely uniform. In such ideal case, all electrodes might have similar coupling. Nonetheless, in most experiments, the coupling varies from electrode to electrode [24, 151]. Moreover, the position of the electrode completely under a cell or under the border between cells contributes to the variation in spike shape. The main waveforms of the APs are represented in Figure 6.18f, and the results are in accordance to the previously published works [24, 147, 152, 175].

Lastly, signal-to-noise ratios were calculated for the HL-1 recordings. Since the cardiac cells' recorded spike amplitudes typically did not exceeding 300 μV, the overall SNR for such recordings is 20 ± 10.

6.2.4 Summary

The presented GMEA devices show extracellular recordings with excellent signal-to-noise ratios up to 65 ± 15. The use of graphene's extraordinary properties for fabrication of electrode arrays on a biocompatible polyimide substrate results in good cell-interface properties and is promising for further applications. Due to the transparency of our devices, the concept can be extended for optogenetic experiments. Furthermore, the fabrication technique, explored in the thesis can be adjusted for the design of *in vivo* devices as bioimplants.

6.3 GMEAs Conclusions and Outlook

In conclusion, the graphene-based MEAs, fabricated in the span of the thesis on both rigid and flexible substrates, show excellent properties, which have been used for extracellular recordings. A numerous recordings from HL-1 cells, as well as neuronal networks, have been performed *in vitro* via the same GMEAs, showing their excellent stability and durability. Furthermore, the SNRs of the recorded signal are up to 116 for cardiac and 100 for neuronal spontaneous activity. To our knowledge, this is also the first time spontaneous neuronal spiking-bursting activity is recorded by graphene-based electrodes *in vitro*.

In order to give a comprehensive overview and comparison of our results to the state-of-the-art, Table 6.2 is given.

Table 6.2: An overview of liquid gated graphene transistors used in literature.

	Active material	Substrate	Electrode diameter	Noise, µV	Tissue type	SNR
This work 1 [57]	Graphene	SiO$_2$/Si and Borofloat	10 µm 20 µm	10.26±4.6$^{a)}$ 10.7±7.2$^{a)}$	HL-1	45±22$^{b)}$ (max - 116) 35±12$^{b)}$ (max - 65)
This work 2 [56]	Graphene	Polyimide	20 µm	20±6$^{a)}$	Heart tissue	65±15
This work 3 [56]	Graphene	Polyimide	20 µm	20±6$^{a)}$	HL-1	20±10
This work 4 [57]	Graphene	Borofloat	20µm	10.7±7.2$^{a)}$	Neurons	Bursting: 48±26 (max-100) Spontaneous: 16±6 (max-33)
Du et al. [178]	Graphene	Quartz	20 µm	15±5	Neurons	10.3± 1.2
James et al. [19]	Au planar Pt non-planar	Fused silica	12 µm	15±5$^{d)}$	Neurons	15±10
Kim et al. [18]	Au flakes	Glass	5-50 µm	N/A	Neurons	20±10
Berdondini et al. [20]	Pt	SiO$_2$/Si Pyrex7740	30 µm 22 µm	8.2 6.5	Neurons	N/A
Bruggemann et al. [17]	Gold planar	SiO$_2$/Si	10 µm 20 µm	7 6.5	HL-1	57$^{c)}$ 141$^{c)}$
Hofmann et al. [24]	Au nanocavity	SiO$_2$/Si	10 µm	9.5±0.5$^{c)}$	HL-1	158± 8
Nick et al. [186]	Au planar TiN rough	Quartz	30 µm	N/A	Chicken cardiomyocytes	10$^{e)}$ 207$^{e)}$

$^{a)}$ Estimated as 2×MAD; $^{b)}$ Calculated from the top 20% of the recorded data; $^{c)}$ Estimated as 1×RMS; $^{d)}$ Estimated as peak-to-peak values; $^{e)}$ Estimated as $(\nu_{peak}/\sigma_{noise})^2$.

Chapter 7

In vivo Probes

This chapter will introduce a new strategy for fabrication of the flexible graphene-based MEAs and FET arrays designed specifically for *in vivo* applications.

7.1 Motivation

While *in vitro* studies give us a general understanding of the ionic channels and cellular firing on a deep, even sub-cellular level, a further study of whole organs (e.g. brain or eye) activity is required in order to understand their functions and dysfunctions. The *in vivo* studies can lead to a higher level of understanding of the brains work, as well as to find treatments to such neurological diseases as Parkinson's. Understanding retinal functions can lead to fabrication of artificial retinal implants or even whole artificial eye replacements in the near future. These are the two main applications, our *in vivo* probes are designed for.

However, *in vivo* insertion of a chip/device/carrier inside the body, requires extra long feedlines, extra connectors and difficulties in the fabrication. As it has been shown in Chapters 5 and 6, we succeeded in fabrication of stable graphene-based devices of polyimide substrate. The devices in general are biocompatible, as polyimide is [54, 157], as well as graphene [48–50]. Biocompatibility of the graphene used in this work was also studied specifically and it was shown that neurons prefer to grow on graphene. The details can be found in Appendix E of this thesis. However the geometry of the devices could not be simply used for an *in vivo* prosthesis. Therefore a new fabrication design has been established in order to fulfill all of the requirements for such *in vivo* probes:

- Thin and flexible. Less than 10 µm in thickness in our case.
- Sensitive and multifunctional. We have both: GFET and GMEA-based probes.
- Geometrical dimensions should fit into a specific application (tissue or organ). We have four different designs fabricated on one wafer, see details below.

- Measurements should be quick and reproducible. We are currently establishing a way to measure the probes via BioMAS technique, presented in section 3.3.4.

7.2 Design

As described before, the fabrication is done on 4-inch wafers. The mask is designed such that each of the wafers consists of the 4 different probes. All of the GMEA probes have two extra variations: "metal feedline" and "graphene feedline". In the first case, the devices are fabricated classically, where, as can be seen from Figure 7.1, graphene is confined only in these areas of passivation openings. While in the latter case, the metal feedlies end before the middle parts of the devices and graphene feedlines extend to the measurement area (see Figure 7.1). In this case, the middle regions of the probes (where active sites are) are completely transparent, giving new opportunities for optogenetics (see Figure 7.1).

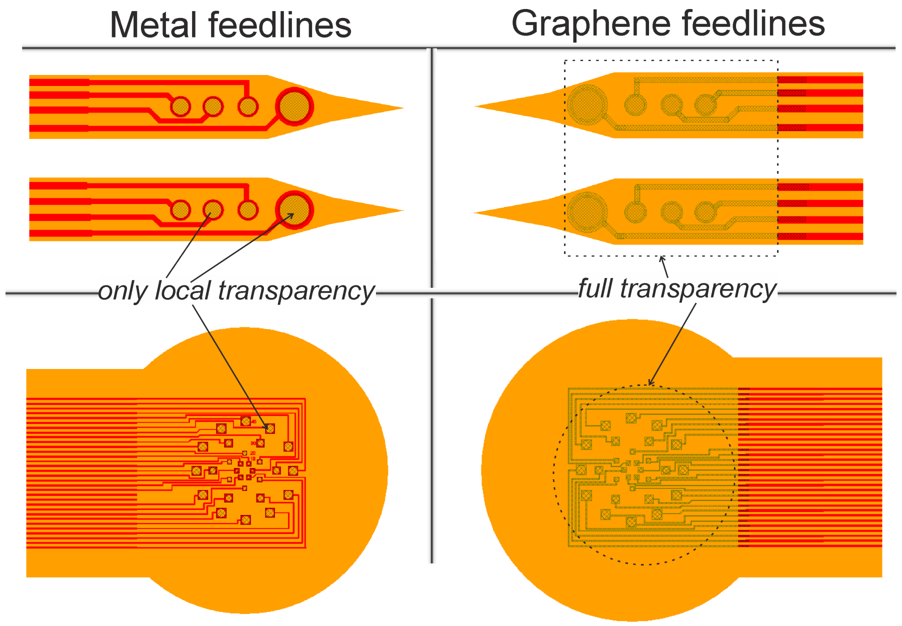

Figure 7.1: The difference between "metal feedline" and "graphene feedline" modifications.

Details and overall dimensions of the probes are given in Figure 7.2 and the details are described below:

- **Probe 1. General *in vivo* GFETs.** This layout consists of 16 GFETs per probe (see Figure 7.2a).

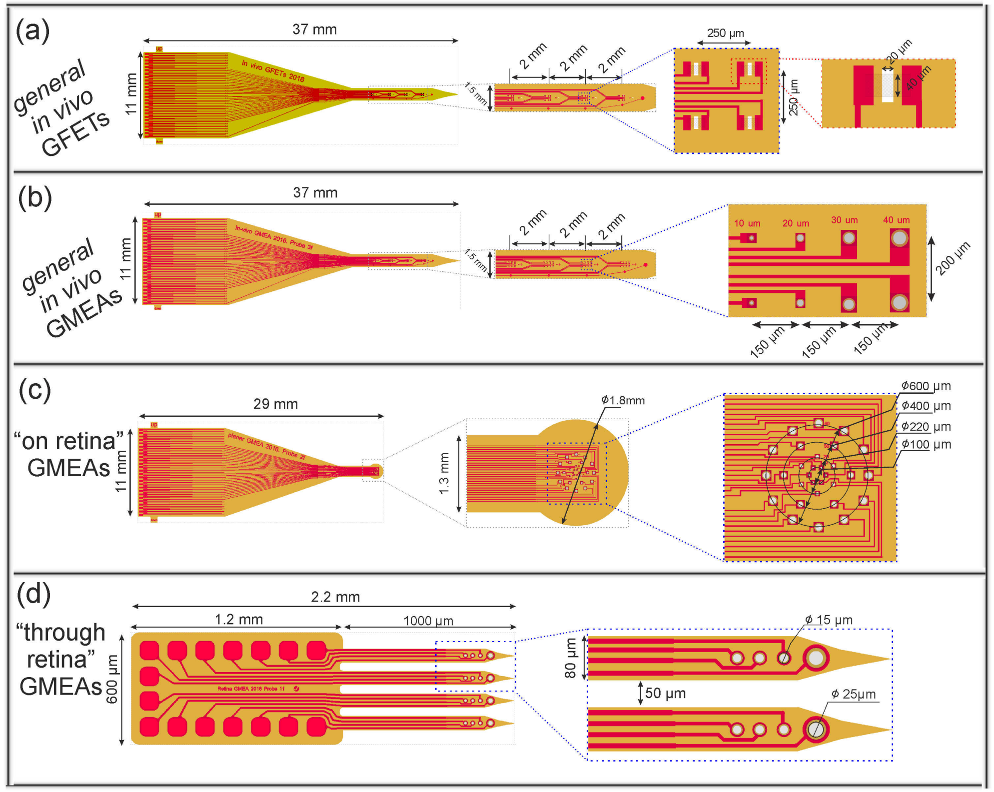

Figure 7.2: Overview of the four main *in vivo* probes. (a) The general *in vivo* GFETs; (b) - general in *vivo GMEAs.* These probes are rather large and consist of one shank that ends with a pointed tip for penetration into a tissue. (c) - "on retina" GMEAs. The electrodes are arranged radially in order to resemble retina's shape. (d) - "through retina" GMEAs, with four small shanks with pointed tips for penetration through retinal layers and to record and stimulate from these different layers of the retina.

- **Probe 2. General *in vivo* GMEAs.** This layout consists of 32 electrodes per probe (see Figure 7.2b).

The general *in vivo* GFETs and general *in vivo* GMEAs probes are schematically similar, and designed with a general task of measuring *in vivo* brain activity. The total width of the probe is 11 mm at wide part and the length is 37 mm (see Figure 7.2a-b). Since the final goal has not been identified precisely, there is only one long (10 mm) and narrow (1.5 mm) shank and four measurement sites, separated 2 mm away from each other to ensure measurements from different depth of insertion. In the case of GFET probes, there are four GFETs per each site, and total of 16 GFETs. The GFETs have a fixed width of 40 µm and length of 20 µm. In the case of GMEA probes, there are eight electrodes per site, and a total of 32 electrodes. At each site there are two electrodes of 10 µm, 20 µm, 30 µm, and 40 µm in diameter in order to study the signal-to-noise ratio of the *in vivo* recordings, which might be different in terms of signal amplitude and coupling. The shank is tipped at the end of the probe to ensure penetration into a tissue.

- **Probe 3. "On retina" GMEAs.** The probe is intended to be used on top of a retina to perform recordings from ganglion cells. This layout (see Figure 7.2c) contains 30 GMEAs arranged in a circular manner, and have smaller electrodes closer to the middle of the chip (10 µm diameter in the first circle, 20 µm diameter in the second) and larger electrodes to the outer side of the circle (30 µm diameter in the third circle, and 40 µm diameter in the outer circle). This is done in order to resemble the retina's architecture as best as possible: the density of cells is more important in the middle of the chip than in peripheral. The length of the whole probe is shorter to reduce any passive noise, and the end of the probe has a round shape, of approximately 1.5 mm in diameter, in order to fit typical retina's size of animals (e.g. rats).

- **Probe 4. "Through retina" GMEAs.** This layout consists of very small probes, 2.2 mm long and 0.6 mm wide (see Figure 7.2d). Each of the probes has four shanks, and four electrodes per shank. Each shank is just 80 µm wide and embodies three electrodes of 15 µm in diameter, and one electrode of 25 µm. The design of these probes is adjusted from the so-called BiMEA design [187], and intended to use for similar purpose of simultaneous measurement and stimulation of different layers of the retina.

7.3 Fabrication

In general, the device fabrication recipe is similar to a typical flexible GMEA/GFET fabrication. The only problem is that the bottom polyimide layer can not be shaped in the last step, as the shapes are rather complex, and not just a set of orthogonal lines. Therefore, we need to shape the bottom polyimide layer prior to other fabrication steps. This is done by using HD-8820, a photostructurable polyimide. Further metallization, graphene transfer, second metallization and passivation are done similar to the process reported before in Chapter 6.

For the step-by step fabrication see Figure 7.3 and description below:

1. **Sacrificial layer.** The first fabrication step is to evaporate a uniform Cr/Au/Cr metal layer on top of a wafer. It serves as a sacrificial layer, and will be etched in the

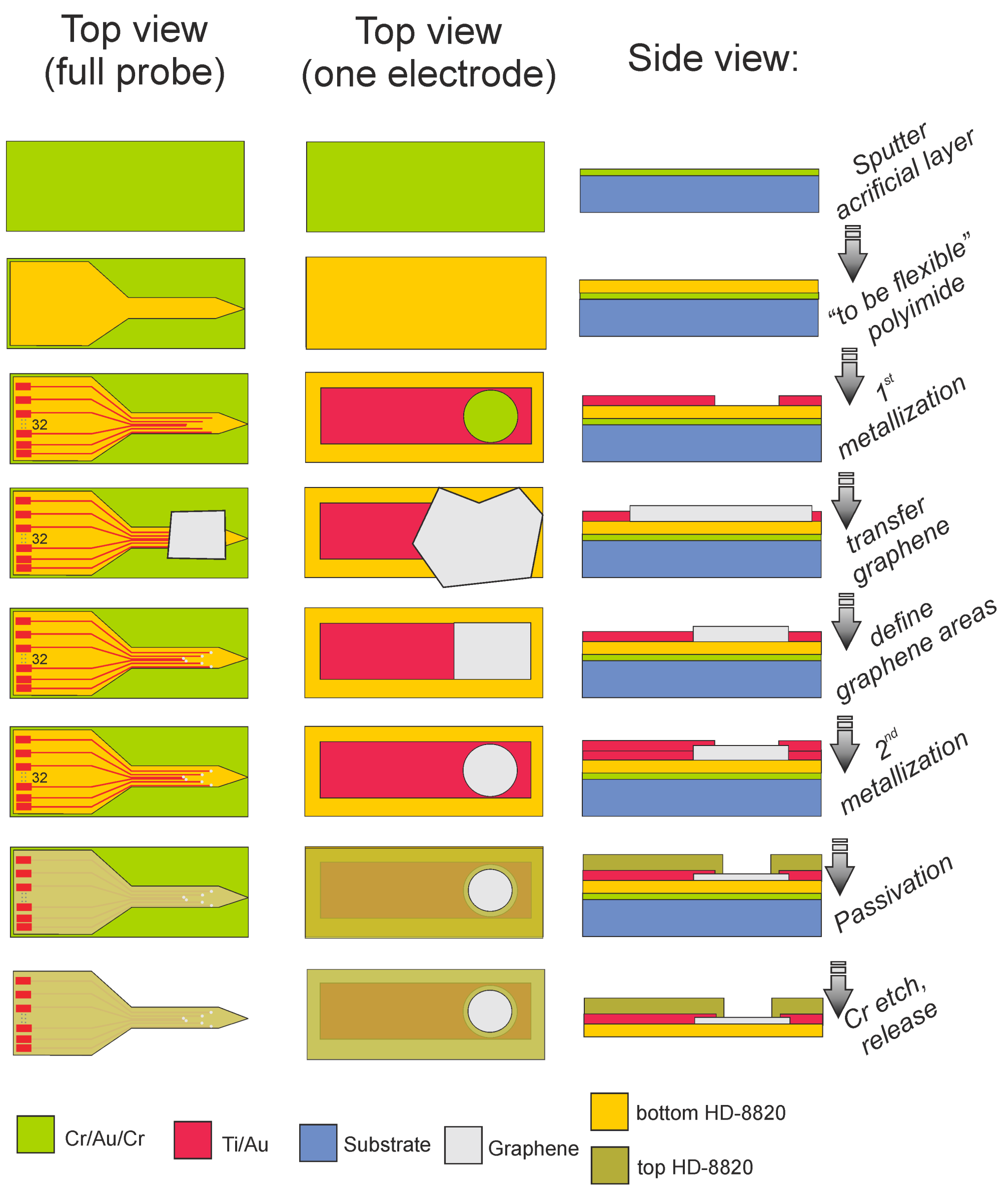

Figure 7.3: The overall fabrication steps with three different views: top view on the whole probe; top view on one electrode; side view on one electrode.

very last step to detach the flexible probe from the rigid wafer. It is important to have a wafer support in order to align the masks sequentially. Gold in the triple stack (Cr/Au/Cr) serves as the charge flow interlayer, and helps the etching to happen. A simple Cr layer was tested, however the etching process was saturated after 1-2 mm of

Cr etched and no further underetch was possible. With this, a stack of Cr/Au/Cr with thickness of 10nm/100nm/50nm (from bottom to top) thickness stack was selected.

2. **The flexible base.** HD-8820 was chosen to serve as the flexible base since it is a photostructurable resist. Spin-coated and developed as described in Appendix (A), the polyimide results in a 3-4 µm thick base.

3. **First metallization.** An AZ nLOF-2020 / LOR-3B photoresist stack then was used to fabricate a first layer of feedlines and graphene transfer alignment markers.

4. **Graphene transfer.** Graphene was transfered using a high throughput transfer technique, as described in Chapter 4.

5. **Defining graphene areas.** Graphene was shaped into smaller areas, defined to the active areas of GMEAs or GFETs, as described in Chapter 4.

6. **Second metallization.** Similar to the first metallization (see step 3);

7. **Passivation**. The same polyimide, HD-8820, and the procedure was used to passivate the probes.

8. **Release.** Chromium etch is performed to release the flexible probe.

SEM images of the GFETs, GMEAs and “retina through” GMEAs, fabricated on a dummy SiO_2/Si wafer are shown in Figure 7.4 in order to check the fabrication flow.

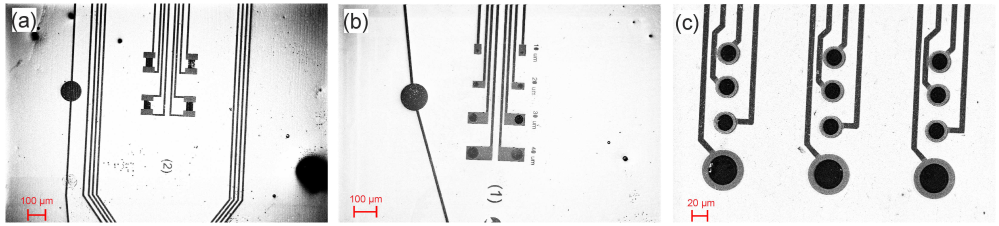

Figure 7.4: SEM images of GFET probes (a), GMEA probes (b), and “through retina” GMEAs, fabricated on a rigid silicon dioxide substrate. The images are taken after the second metallization step.

After the final annealing of polyimide, the probes could be in general released. However, as the first tests showed, the probes tend to bend up and roll upon releasing. Therefore, in order to perform first checks, a thin layer of PDMS was dropped on top of the chips and baked, then the chromium etch was performed, releasing the thin *in vivo* probes, but with a PDMS support. The PDMS is chosen due to its low adhesion properties, allowing, in general, to stamp/transfer the probe onto any other substrate. As shown in some works, PDMS can be used even for direct stamping of the graphene, therefore no damage to graphene due to the stamping process is expected [188]. The optical and SEM images of the PDMS-supported probes can be seen in Figure 7.5.

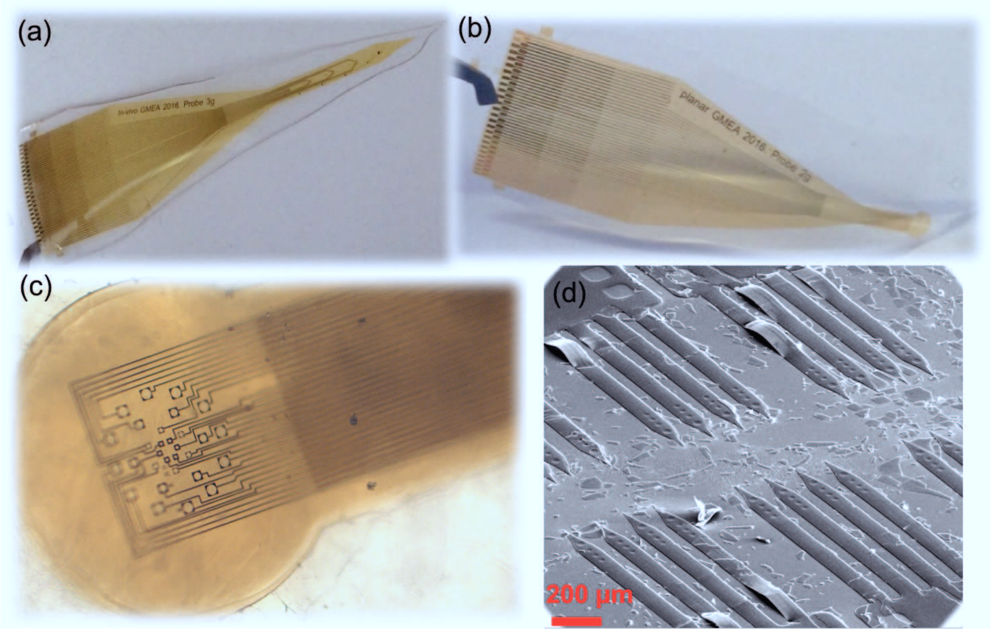

Figure 7.5: Optical image of general GMEA probe (a), "on retina" GMEA probe (b), and a zoom into the middle area of the "on retina" GMEA probe (c), all supported by PDMS. In (d) is given an SEM image of the set of "through retina" GMEA probes, supported by PDMS, but sputtered with a thick layer of Iridium to ensure charge flow.

7.4 Characterization

As this is still an on-going research, only partial characterization of the GFETs is shown in this thesis. From the variety of the probes, only parts of the flexible GFET-based devices were characterized and analyzed. The V-shaped I-V curves (see Figure 7.6), which are typical for graphene transistors, are recorded for the flexible GFETs. The GFETs are fairly stable and show characteristic performance similar to the polyimide-based GFETs, as reported in Chapter 5. The width and length of the transistors is this case are fixed and equal to 40 µm and 20 µm, respectively. The maximum transconductance measured so far was in the range of 550 $\mu S\,V^{-1}$, which is comparable to typical polyimide-based GFETs. However it is important to mention that the GFETs have not been fully annealed (see Chapter 5) in order to not damage the chips prior to full analysis. Therefore, a more comprehensive annealing will be implemented in order to find the stable values of the transconductance, and as it can be drawn from Figure 5.2d, the final performance can be expected to be least a factor of 2 larger.

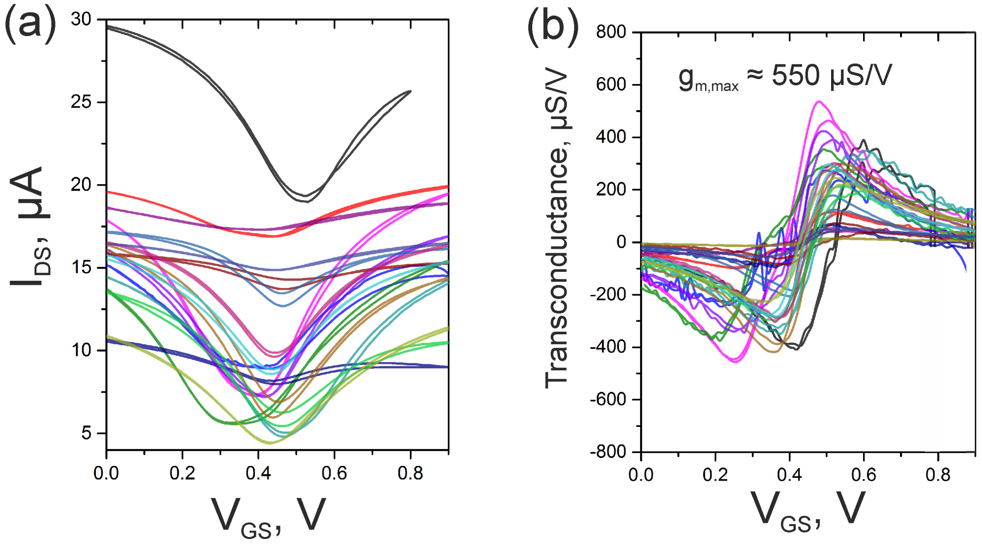

Figure 7.6: (a) I-V curves of the *in vivo* GFETs. (b) The transconductance plots of the GFETs. Each color represents a single transistor.

Up to this moment, the devices are measured using the Keithley 4200 SCS probe station (as described in details in Section 3.3.1) and (careful) needle contacts. However, in order to establish stable, long-term, and multi-channel measurement system, we work on extending the already existing BioMAS platform via two-stage connectors:

- One from a headstage to a manually designed printed circuit board (PCB). The PCB will be varied for each chip's kind in order to assign a correct potential (measure a correct current) to each pin and consequently to each feedling of the probes.
- The board has a connector, designed and fabricated in the way to fit onto the I/Os of the flexible chips.

7.5 Summary and outlook

In summary, we have developed an initial platform for *in vivo* probes and *in vivo* measurements. The wafer design consists of probes designed for different purposes and different applications. The probes are thin (around 10µm) and biocompatible (as polyimide and graphene are biocompatible). However, in order to establish a versatile measurement technology, further efforts should be given for:

- Development and modifications of the multichannel measurement technology based on existing BioMAS to ensure stable long-term measurements;
- Development of an insertion protocol. Since the probes are thin and soft, it is good to minimize tissue inflammation response, but it makes difficult to insert the probe in the tissue. This can be done using silk proteins [189], or other biodegradable polymers [190], which are rigid while insertion, but dissolve upon exposure to saline solutions [189].

Chapter 8

Conclusions and Outlook

In the previous chapters of this dissertation, fabrication, characterization, implementation and improvement of graphene-based transistors and electrodes was shown. During the work, numerous batches of GFETs and GMEAs were fabricated, analyzed and used for interfacing with cells.

The first challenge of the work was to overcome the problem of how to fabricate graphene-based devices on a large scale (4-inch wafers) without having constant access to CVD grown graphene. Since the graphene was grown by our collaborators (who ensured the excellent quality of it) [71], a great effort was given to establish a high-throughput graphene transfer set-up and method. The developed [55] and patented method, as presented in Chapter 4 of the thesis, now allows me to fabricate a 4-inch wafer with 52 chips, using only a 4 cm^2 piece of CVD grown graphene. Compared to a conventional large piece graphene wet transfer, this method results in 34-fold improvement in terms of used-to-wasted graphene ratio. The method is unique, but at the same time is universal and scalable to any wafer size and and device-per-wafer distribution. When the high-throughput transfer method was established, it became possible to fabricate different kinds of devices on a wafer scale. The rigid GFETs (Chapter 5), rigid GMEAs (Chapter 6), flexible GMEAs (Chapter 6), and *in vivo* probes (Chapter 7) were fabricated, utilizing this technique for graphene transfer.

Liquid-gated GFETs was my first priority, as based on literature reports, they outperform any other state-of-the-art transistors that can be used for bioelectronic applications [45,52]. For my studies, the GFETs were fabricated with the following parameters:

- different substrates (SiO_2/Si, HfO_2, sapphire, polyimide) in order to study substrate effect;
- variations in width and length (from 20×20 μm^2 down to 2×3 μm^2);
- variation in passivation type ("windows" and "feedline follower").

Moreover, since the transistors were intended to be used for liquid operation, a general and simplified models of the interface capacitance were developed and used for data analysis in the thesis.

In terms of the GFETs' performance, the following main conclusions were drawn (see Chapter 5 and ref. [52, 58] for details):

- the transconductance was found to increase with increased W/L ratio of the graphene channel;
- the substrate does not drastically affect the average normalized transconductance of the devices. However, it was found that a SiO_2/Si substrate suppresses the maximum mobility values of the GFETs;
- the "feedline follower" and "passivation window" passivation types are generally stable and suitable for liquid gating experiments, however the "feedline follower" passivation type was found to be more suitable for neuronal interfacing.

It was demonstrated that the GFETs can be used for action potential recordings from:

i. *ex vivo* heart tissue signals with signal-to-noise ratio (SNR) up to 14;
ii. *in vitro* HL-1 action potentials with SNR up to 7;
iii. *in vitro* neuronal spiking-bursting activity with SNR up to 3;

Moreover, the GFETs were found to be fully stable and versatile, therefore in general form a flawless tool for extracellular electrophysiology. However, the gate noise (in the range of 100-200 μV) of the transistors is still too large for fault-free measurements from neuronal cells. Therefore, further work on the GFETs must be performed in order to find ways to minimize/suppress the noise without reducing transconductance, and in total increasing the SNR. This can be done by further varying the width-to-length ratio to ensure high enough transconductance but still low noise. Alternatively, the conducting graphene channel can be passivated/sandwiched with other two-dimensional materials, such as hexagonal boron nitride. In order to investigate the influence of defects and grain boundaries of the performance, a comprehensive study must be performed, varying the channel's geometry with combination of comprehensive SEM and Raman imaging.

As a step towards fully flexible devices, some of my GFETs were fabricated on controllably flexible PIonS substrates. That allowed me to perform flexibility and stability tests of the GFETs. Additionally, *ex vivo* heart tissue activity was successfully recorded with the the flexible GFETs. The PIonS-based GFETs exhibit the largest maximum transconductance ($\sim$11 mS V^{-1}) ever reported, showing that polyimide is a promising materials for interfacing with graphene.

In order to commit the knowledge of GFETs to the study of other biological molecules (such as DNA and aptamers), a side project on point-of-care (PoC) GFETs was started. The details on PoC-GFETs fabrication and characterization can be found in Appendix D. The devices are fabricated specifically to fit into a micro-SD card design to simplify the measurements and be one step closer to the commercializable biomedical testing devices.

GMEAs, in contrast to GFETs, are less difficult to fabricate and implement for extracellular recordings. The GMEAs, fabricated in this work are typically of 10 and 20 μm in diameter, and based on rigid and non-transparent SiO_2/Si, rigid but transparent borofloat, and flexible and transparent polyimide substrates. Transparency of borofloat and polyimide substrates is important to ensure an optical control of the *in vitro* cultures, especially of cortical neurons.

As characterized by electrical impedance spectroscopy, the GMEAs' performance is comparable to those of standard MEAs, allowing to record extracellular potentials from:

i. *in vitro* HL-1 cells with SNR up to 116 (45±22 average ± SD);
ii. *ex vivo* heart tissue with SNR up to 80 (65±15 average ± SD);
iii. *in vitro* neuronal networks with spiking-bursting activity with SNR up to 100 (48±26 average ± SD);

To my knowledge, this is the first extensive record of *in vitro* neuronal bursting action potentials, measured by graphene MEAs. Moreover, a variety of HL-1 action potentials have been recorded, extracted, and analyzed. Low noise of the potentiometric recordings (15±10 μV) increases the general sensitivity of the measurements, leading to recording of complex neuronal spiking-bursting patterns.

Flexible GMEAs, fabricated on polyimide substrate, show exceptional stability and robustness. The flexible GMEAs were used for *in vitro* and *ex vivo* extracellular recordings multiple times, maintaining low noise and high signal-to-noise ratio recordings even after severe mechanical deformations.

To conclude, the GMEAs, fabricated and used during this thesis, have shown their suitability for neuronal interfacing, however some improvements can be made to advance performance or increase the range of applications. For example, the impedance of the devices can be improved by using multilayer graphene, or even 3D structured graphene. Porous/3D graphene, with improved charge injection capability, may be also suitable for further stimulation of the neuronal cell, resulting in a combination of on-chip stimulation and recording technology. Transparency of graphene (97% transmittance for monolayer graphene) opens new roads for on-chip optogenetics.

The main advantage of the GMEAs is their simplicity. Simplicity of fabrication, handling, and measurements, combined with mechanical stability and flexibility, provides high expectations for further *in vivo* implementation of the devices.

In order to get closer to real *in vivo* applications of the GFETs and GMEAs, a new fabrication routine of graphene-based *in vivo* probes was designed and implemented. In order to cover several applications at once, the GFET- and GMEA- *in vivo* probes are fabricated on one wafer with the following variations:

i. general *in vivo* GFETs and GMEAs – with one long (10 mm) shank and linear distribution of the devices with a general purpose (e.g. brain's cortex);
ii. "on retina" GMEAs – with radially distributed electrodes for interfacing and measurements from retina's ganglion cells;
iii. "through retina" GMEAs – with four small shanks (1 mm) and four electrodes per shank for simultaneous measurement and stimulation of different layers (cell types) of the retina;

To date, the probes are fabricated and pre-characterized for their performance. The extensive work on establishing the *in vivo* measurement technology with these probes has just begun, and requires further efforts to establish insertion (using silk fibroin or other biodegradable proteins), and measurement (preferable using the existing BioMAS platform) methodology prior to the measurements.

To conclude the work, I believe that the graphene-based devices (GFETs and GMEAs) and *in vivo* probes fabricated on their basis can advance the fields of electrophysiology and neuroprosthesis.

Acknowledgments

A PhD life is full of problems and solutions, discussions and arguments, brain work and hand work. This work would not have been possible without the people (friends and colleagues) around me, those who worked with, helped, encouraged, and pushed me towards my goal. Hereby I would like to express my gratitude to these people.

First of all I would like to thank **Prof. Dr. Andreas Offenhäusser** for the supervision, constant support, and scientific discussions. The three years in the institute and your supervision gave me a strong background in many aspects of scientific life.

Prof. Dr. Bernhard Wolfrum – thank you for the numerous discussions, corrections, and help with understanding of scientific relevance of the topic. Special thanks for the inspiring ideas and insights of answering to reviever's comments.

Prof. Dr. Jörg Fitter – thank you for kindly agreeing to be the second examiner of my work.

Silke Seyock – thank you for being the biological part of the project, help with all the cell cultures and measurements. It was great to work with you!

Dr. Vanessa Maybeck – thank you for being the mentor in many aspects, especially in the bio-related experiments and data interpretation. The special gratitude is for all the corrections of my writings.

Fabian Brings and **Jan Schnitker** – for the help with electronics of the measurement set-ups and large-scale data interpretation. Corresponding gratitude is to **Norbert Wolters** for building and support the hardware and **Dieter Lomparski** for programming the software.

Dr. Dirk Mayer, **Dr. Svetlana Vitusevich**, **Prof. Dr. Roger Wördenweber**, **Dr. Yulia Murzina**, and **Prof. Dr. Hans-Joachim Krause** – for understanding of my, sometimes crazy, ideas, discussion, and help in realization of the projects, helpful insights and comments.

Dr. Kyryl Greben, **Ihor Zadorozhnyi**, **Dr. Sergii Pud**, **Dr. Wangyang Fu**, **Tianyu Qiu**, **Ekaterina Koposova**, **Dr. Lingyang Feng** – for the work together under these bright (not always) ideas, conducted experiments, fun in the labs, and scientific discussions.

Michael Prömpers and **Marko Banzet** – for the cleanroom support and process discussions.

Mathis Ernst, **Dario Sarik**, **Max Brambach**, and **Pegah Shokoohimehr** – for the great experience of being a supervisor :) Thank you for all these days and years, problems, questions, ups and downs. I learned with you and proud of having worked with you.

Prof. Dr. Jose Garrido, **Benno Blaschke**, and **Martin Lottner** – for the collaboration and introduction to your knowledge. It helped me to understand the topic deeper.

Dr. Tianru Wu and **Prof. Dr. Xiaoming Xie** – Thank you for the constant support with graphene samples, discussion of the problems and further collaboration.

Bettina Breuer - for taking care of all neuronal preparations and support in cell culture labs.

Dr. Elmar Neumann and **Elke Brauweiler-Reuters** - for the help with SEM and TEM measurements and image interpretation.

Stella and **Andreea** – thank you for the fun part of these years.

Hanna – thank you for being always by my side.

Appendices

Appendix A

Cleanroom fabrication steps

Metallization

A double layer of LOR-3B and AZ nLOF-2020 is always used for metallization in order to result in an undercut structure for further metal evaporation. The overall process is described below:

- **Dehydration:** 150°C anneal on a hotplate for at least 5–10 minutes.
- **Spin-coating:** LOR-3B, 3000 rpm, with ramp, closed lid, 5 ml, disperse around the whole wafer, otherwise causing problems;
- **Soft bake:** 150°C, 5 minutes, hotplate;
- **Spin-coating:** AZ nLOF-2020, 3000 rpm, with ramp, closed lid, 3 ml;
- **Soft bake:** 100°C, 2 minutes, hotplate;
- **Exposure:** i–line, 40 mJ/cm^2;
- **Post-exposure bake:** 110°C, 1 minute, hotplate;
- **Develop:** in AZ 326 MIF for approximately 33-35 seconds. The margin depends on the structure and external parameters;
- **Washing:** water cascade, drying with N_2 gun;
- **e-beam assisted evaporation:**
  - ✓ Balzers PLS 570;
  - ✓ Argon pre sputtering for 1 minute, 150 V and 5 A discharge potential and current accordingly.

  - ✗ No argon pre sputtering when doing 2nd metallization to contact graphene on top;
- Lift–off in acetone overnight. Following clean in IPA, AZ 326 MIF, and water cascade

Defining graphene areas

Using AZ-5214e resist as a common, thick and easy photoresist.

- **Dehydration:** 150°C, for at least 5–10 minutes, hotplate.
- **Spin-coating:** AZ-5214e, 3000 rpm, with ramp, closed lid, 3 ml;
- **Soft bake:** 110°C, 1 minute, hotplate;
- **Exposure:** i–line, 50 mJ/cm^2;
- **Develop:** in AZ 326 MIF for approximately 60–70 seconds. The margin depends on the structure and external parameters;
- **Washing:** water cascade, drying with N_2 gun;
- **Oxygen plasma:**
  - Barrel Reactor TePla Gigabatch 310M;
  - To remover the unnecessary parts of graphene;
  - 300W, 200 sccm, 10 minutes.
- **Remove AZ-5214e** in acetone for 10 minutes;
- **Clean** in IPA and N_2 blow dry.

Passivation

- **Dehydration:** 150°C, for at least 5–10 minutes, hotplate.
- **Spin-coating:** VM-652 adhesion promoter (always use a fresh one), 3000 rpm, closed lid, 3 ml;
- **Spin-coating:** HD-8820, 5000 rpm, closed lid, 3-4 ml, disperse directly from a bottle;
- **Slow soft bake:** hotplate set to 120°C,
  - wafer is automatically moving slowly down on the supporting pins;

  - starting hight 10 mm;
  - 0.1mm/s speed;
  - annealing for 4 minutes as soon as reaches the surface.
- **Exposure:** i–line, 250 mJ/cm^2;
- **Develop:** in AZ 326 MIF for 75-90 seconds. The margin depends on the structure and external parameters;
- **Washing:** water cascade, drying with N_2 gun;
- **Hard bake in a convection furnace:**
  - Start:room temperature, N_2 atmosphere;
  - Ramp up to 200°C with a speed of 4°C/min;
  - Hold the 200°C for 30 minutes;
  - Ramp up to 350°C with a speed of 2.5°C/min;
  - Hold the 350°C for 30 minutes;
  - Cool down to room temperature with as lowest speed as possible (set to 4°C/min, but depends on the furnace);

Chemicals, reagents and resists

Table A.1: List of chemicals used in the cleanroom and for cleanroom fabrication process.

Reagent	Supplier
PI-2611	HD Microsystems
PI-2545	HD Microsystems
VM-652	HD Microsystems
HD-8820	HD Microsystems
LOR-3B	MicroChem Corp.
AZ-5214e	MicroChemicals GmbH
AZ nLOF-2020	MicroChemicals GmbH
AZ 326 MIF	MicroChemicals GmbH
PMMA AR-P 669.04	Allresists GmbH

Appendix B

Device fabrication recipes

In the following Chapter, the concise recipes for fabrication of the Rigid GFETs, Flexible GFETs, Rigid GMEAs and Flexible GMEAs are given with references to details of each fabrication steps in the Appendix A.

Rigid GFETs and GMEAs

- **Wafer:** 4-inch, SiO_2/Si or Sapphire;
- **1st Metallization:** (10/50 nm) Ti/Au, see details in A;
- **Graphene transfer:** High-throughput transfer, see 4 and 3.2;
- **Define graphene areas:** Oxygen plasma, see details in A;
- **2nd Metallization:** (10/100 nm Ti/Au, see details in A;
- **Passivation:** 3-4 µm thick polyimide HD-8820, details in A;
- **Dicing** GFETs into 11×11 mm^2, GMEAs into 24×24 mm^2.

Flexible GFETs and GMEAs

- **Wafer:** 4-inch, SiO_2/Si;
- **Sacrificial layer:** Evaporation of Cr/Au/Cr (10/100/50 nm) stack, see details in A;
- **Flexible substrate:** PI-2611, 10µm in thickness, fabricated similar to HD-8820, as described in A;
- **1st Metallization:** (10/50 nm) Ti/Au, see details in A;
- **Graphene transfer:** High-throughput transfer, see 4 and 3.2;

- **Define graphene areas:** Oxygen plasma, see details in A;
- **2nd Metallization:** (10/100 nm) Ti/Au, see details in A;
- **Passivation:** 3-4 µm thick polyimide HD-8820, details in A;
- **Dicing** GFETs into 11×11 mm^2, GMEAs into 24×24 mm^2;
- **Release:** Chromium etch to suspend the chips from the rigid carrier substrate.

PIonS GFETs

- **Substrate:** 12×40 mm^2 in size steel substrate;
- **Flexible substrate:** PI-2611, 10µm in thickness, hard-baked similar to described in A;
- **1st Metallization:** (10/50 nm) Ti/Au, see details in A;
- **Graphene transfer:** Standard wet transfer, see 3.2
- **Define graphene areas:** Oxygen plasma, see details in A;
- **2nd Metallization:** (10/100 nm) Ti/Au, see details in A;
- **Passivation:** 3-4 µm thick polyimide HD-8820, details in A;

Appendix C

Device Encapsulation

To use the chips of the graphene transistor arrays for multi-channel extracellular measurement, they have to be prepared. That includes contacting the chip to a carrier with standardized contacts and a so called encapsulation of the chip. This is necessary in order to make sure that (a) chip is not damaged by the saline solutions; (b) the chip fits into pre-amplifier headstage (see section 3.3.4) and can be reliably measured.

Depending on a chip sizes and substrates (rigid/flexible; transparent/non-transparent), the procedures are different and are listed below as well as shown in Figure C.1.

- **Wire Bonding to a carrier.** In this method, the chip is first glued (with a small amount of epoxy glue) to the ceramic carrier. The carrier has corresponding to each other inner and outer contact pads, whilst inner are made for the wire bonding, and outer for the use in the measurement systems. The chip to carrier connection is done on a semi-automated wire-bonding machine. When the wires are created, the space around is filled (slowly and carefully) with PDMS in order to isolate them from the liquid environment

- **Flip-chip to a carrier.** The carrier was placed on a hotplate (180°C), and a soldering paste (42Sn/58Bi alloy) was dispersed around the contact pads. When the solvent was evaporated and the excess alloy was removed, only small amounts of alloy were left on top of the carrier‘s contact pads. Afterwards, the transparent chip was simply placed on top of the carrier and aligned under the microscope. When cooled down, any residual solvent was removed with ethanol, and the back side of the chip was sealed with medical epoxy (EPO–TEK 302–3M). The advantage of this procedure is that the whole chip is contacted to the carrier at once, which saves time and simplifies the procedure. However, the process is only easily applicable to transparent chips.

- **Conductive magnets.** This is the method used to measure the GFETs on PIonS substrates. The method had to be invented since simple probe needles would punch though the polyimide layer if measured constantly and repeatedly. However, the method allows just one or two transistors characterization at a time, which is a drawback for extracellular measurements.

- **Measure directly.** The method is only possible for the rigid GMEA devices, with either SiO_2 or borofloat substrate, since the devices and their contact pads are already large enough to fit into the BioMAS system.

Regardless of the above-mentioned methods, which have their own peculiarities, there is one necessary step in all the methods:

- **PDMS-assisted gluing of a glass ring.** The step is required to create a sealed environment for the cell culture medium, large enough to provide the nutrition solution for cells for a certain amount of time, but short enough that direct measurements, such as patch clamp are possible. For the GMEA chips, the glass ring with an outer diameter of 20 mm (17.8mm inner diameter) was glued on top of the 24×24 mm^2 chip using PDMS (10:1, Sylgard). For the GFET chips, there are usually two glass rings: a large one (20 mm of outer diameter) to supplement enough liquid and a small one (9 mm outer diameter) to provide a statistically equal surface at which the cells are seeded.

Devices	Substrates	Solution	Final look
GFETs small (11×11mm^2) 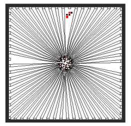	SiO$_2$/Si rigid non-transparent	Wire-bonding	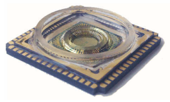
	Sapphire rigid transparent	Carrier	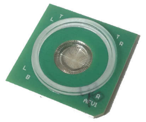
	PIonS semi-rigid non-transparent	Conductive magnets	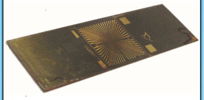
	Polyimide flexible transparent	Carrier	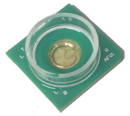
GMEAs large (24×24mm^2) 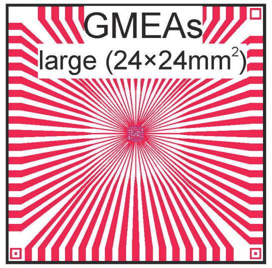	SiO$_2$/Si rigid non-transparent	Measure directly	
	Borofloat rigid transparent	Measure directly	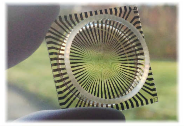
	Polyimide flexible transparent	Carrier	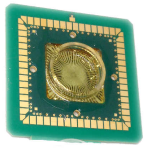

Figure C.1: The overview of the encapsulation of different chips.

Appendix D

Graphene PoC devices

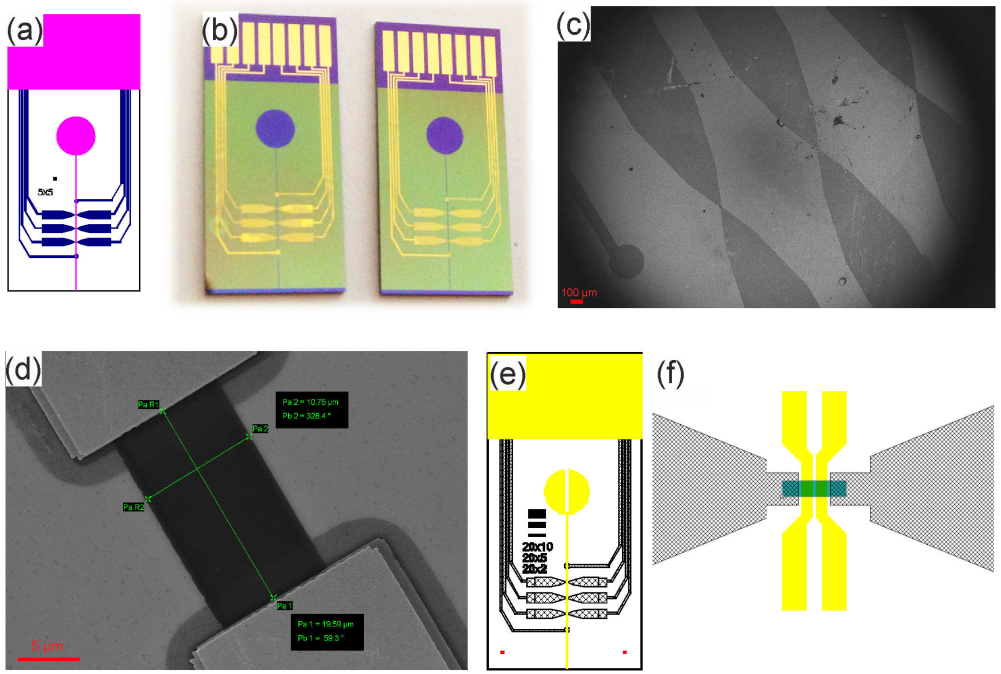

Figure D.1: (a-b) Optical pictures of the fabricated G-PoC devices as well as their design. (c-d) SEM images of the devices made prior to passivation, showing the metal feedlins (dark grey in (c)) and graphene area (black in (d)). In (e-f) is given the design of the chips with two liquid channels, one of which can be modified with a biomolecules, and other not, for a direct on-chip comparison, multianalyte analysis, or selectivity.

The main application our GFETs is intended to be used for was electrophysiological measurements from different types of cell cultures. Therefore, the chips, layout and geometrical distribution were specifically designed to meet that goal. However, graphene, and specially graphene FETs possess other properties which could be used for to study a diversity of different biological mechanisms, including DNA and aptamer interactions. In order to commit our GFETs for such a goal, we have designed another kind of GFET chips with a point-of-care (PoC) purpose (see Figure D.1a).

PoC design and fabrication

The chips (see Figure D.1) are designed to fit into the micro-SD card to simplify and standardize the read-out system. Each PoC chip consists of 8 electrodes, 3 pairs from which are used to contact three GFETs, and two other electrodes are intended for reference, comparison, and stimulation purposes (see Figure D.1a-d). Each chip is passivated with HD-8820 polyimide, except the guideline connected to a big passivation opening (3 mm in diameter) for a drop-in analysis (see Figure D.1). Some of the chips have a special design with two liquid channels in order to perform more complicated comparison of responses to different analytes (see Figure D.1e-f).

Characterization

One test PoC wafer was fabricated, and the I-V curves of each transistor was taken in order to analyze their performance. The overall transconductance also depends on the Width to Length ratio, as proposed previously in the GFETs chapter (see 5). The normalized transconductance has a value of 0.77 ± 0.5 mS V^{-1} □, which is comparably to the values reported for typical GFETs on $\mathrm{SiO_2/Si}$ substrates.

Use and further applications

In order to use the chips for the PoC applications, there is a headstage developed by Fabian Brings, for a similar kind of devices (Silicon Nanowires FETs), however can be easily used for the GFET-PoC applications:

- The headstage is mobile;
- To make the measurements more stable and reproducible, a simple microfluidic system was built and attached to the chip;
- To create an easy “analyte in – measure – analyte out” set-up.

Further research will consist of studies to see a response of attachments of analytes with different functional groups to the graphene, and a further development into, for example aptamer, DNA, glucose, or immunoglobulin (Ig) based sensors.

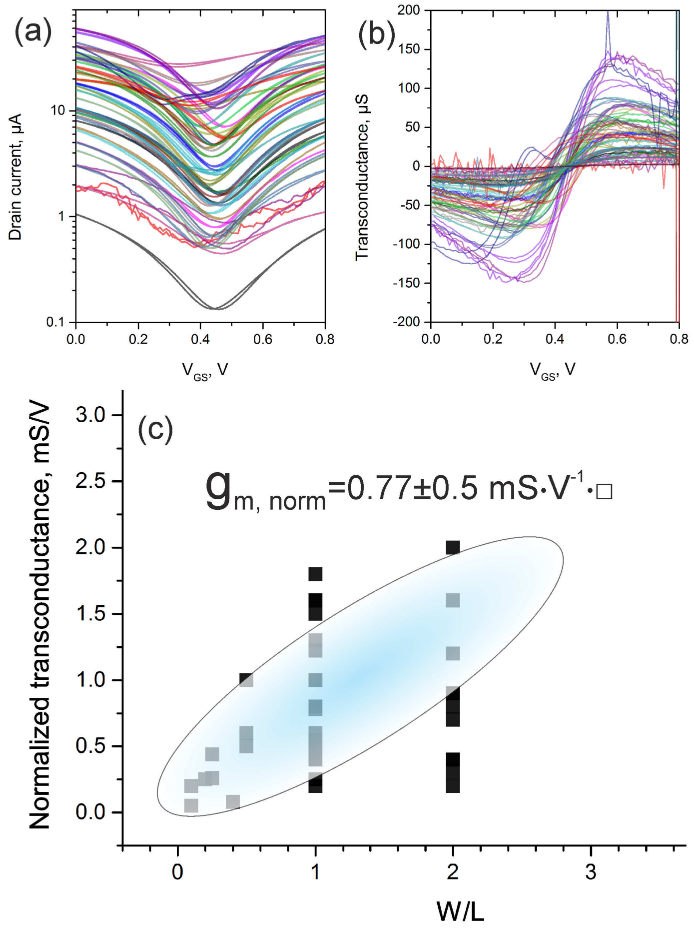

Figure D.2: (a) I-V curves of all the working graphene PoC FETs, showing an overall consistency in the position of Dirac point. (b) the transconductance plots for these devices, showing that typically p-type transconductance (as well as mobility) is larger than n-type. (c) Is given the plot of normalized transconductance of the devices depending on their widths and lengths. The analysis is done similar to explained in section 5.1.

Appendix E

Neuronal guiding

As several works suggested, graphene could be an interesting material for a direct interface with the neuronal cells [48–50, 191]. Moreover, some works suggest that graphene and it's surface can be used for "guiding" the neuronal outgrowth [48, 191]. In order to investigate the issue we have developed simple linear arrays of graphene. The CVD grown pieces graphene of large size (over 5×5 mm^2) were transfered on top of SiO_2/Si chips following the standard wet transfer protocol. After that, AZ-5214e photoresist was spin-coated and shaped to make the lines with different width and pitch. Then, oxygen plasma was used to structure the graphene. The final results of the arrays were checked by SEM and optical microscopy.

When the chips were ready, prior to the cell culture they were covered with PDL, a common peptide which is used for improved cellular adhesion. The first neuronal cultures on each chip result in a clear guiding effect, similar to reported previously (see Figure E.1). Some of the chips were also fixated with gluteraldehyde, dehydrated in a series of ethanol steps and dried ou in CPD machine in order to be visualized in SEM. Prior to the SEM the chips were covered with an extra layer of Ir (around 10 nm). The resulting SEM images can be seen at the Figure E.2. Both SEM and live-dead images show that the neuronal bodies prefer to grow/attach to the places with graphene rather than without graphene. However, at the closer look it seems that the edges of graphene play a more important role, as it seems that the cells prefer the edges and not the graphene itself.

Literature suggests two theories of the effect behind this phenomena: it is either the oxygen plasma termination of the graphene edges or the binding between graphene and the PDL polymer. However, every consecutive culture (with a corresponding cleaning, and extra PDL coating in between) never resulted in the same effect. None of the theories can explain this part, neither any of the paper show reproducibility of the result for one sample. Every fresh sample results in a clear guiding effect, while every re-used sample does not. In order to investigate the problem comprehensively we will continue to study the effect, via:

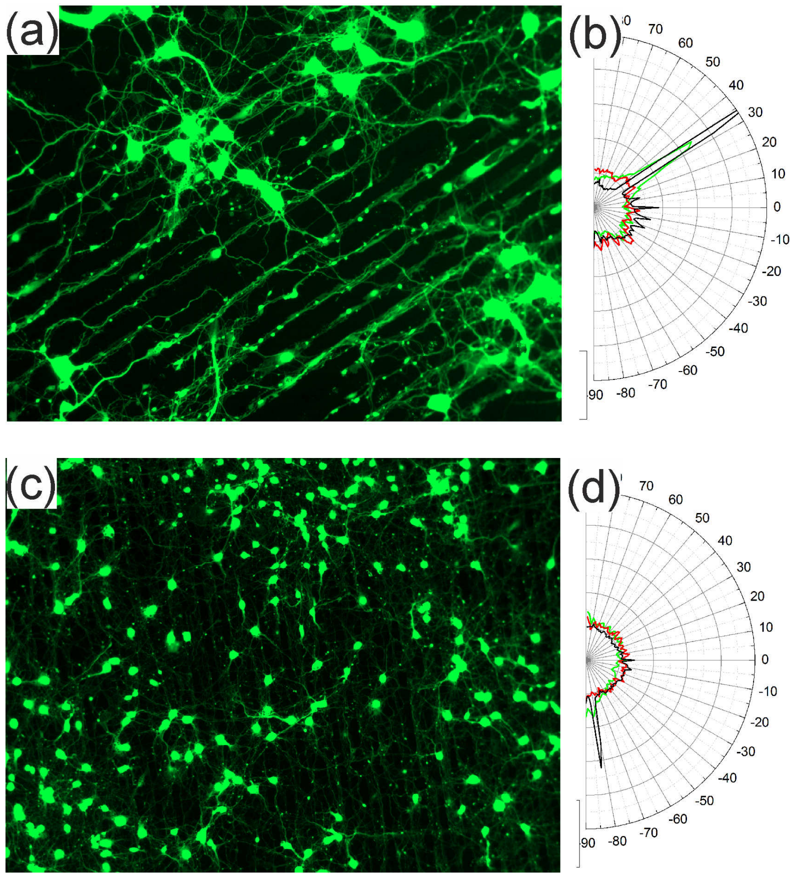

Figure E.1: Two examplary live-dead images (a, c) of the neuronal cells following the graphene stripes, and the corresponding polar plots (b,d) showing the overall directionality of the neuronal outgrowth.

1. etching graphene in a different way (not using oxygen plasma, but Ar plasma for example, therefore excluding the O_2–termination of the edges theory);
2. exploring the possible problems causing the irreproducibility of the guiding effect.

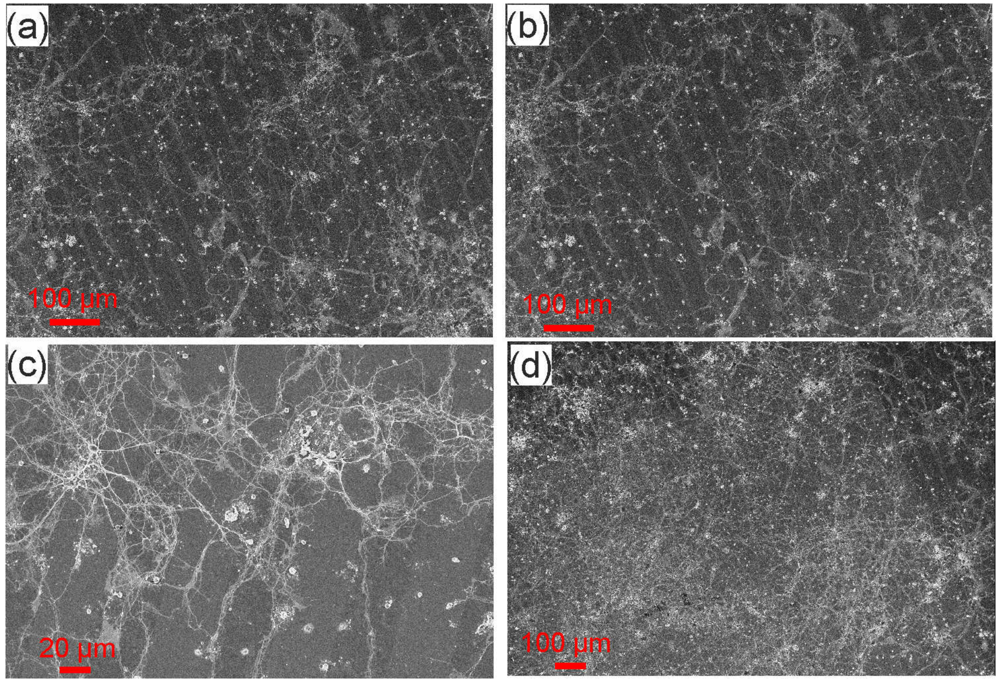

Figure E.2: SEM images of the neuronal cells, grown on top of the graphene stripes. Following the gluteraldehyde fixation, ethanol dehydration, CPD and Iridium deposition, it is clear that the neurons prefer to attach to the graphene' edges and in general follow the directionality of graphene underneath.

Appendix F

HL-1 action potentials recorded by GMEAs

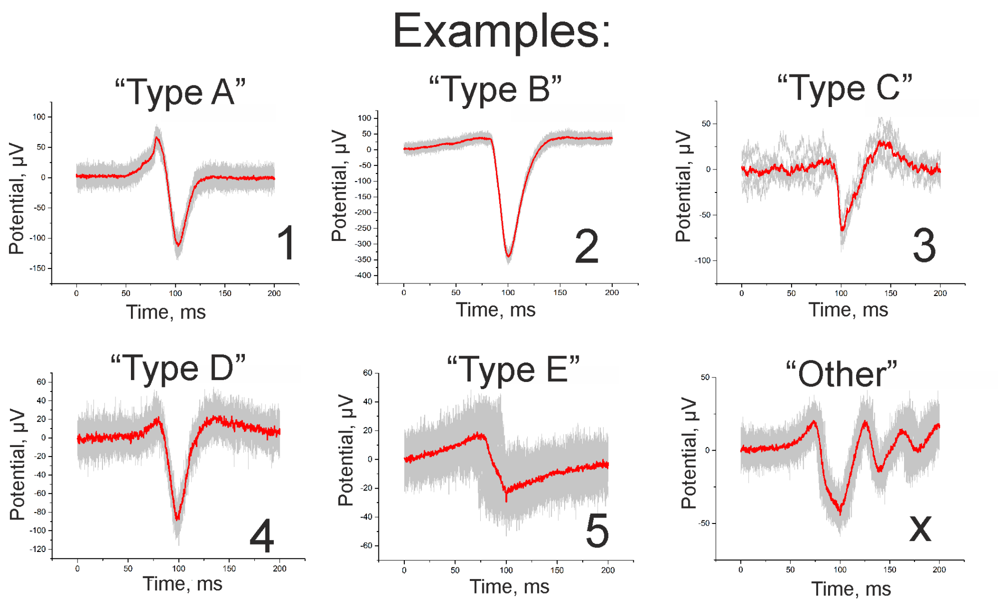

Figure F.1: The six different types of the spikes, sorted and selected manually basing on the signal’s shape: pre-spike, post-spike, etc.

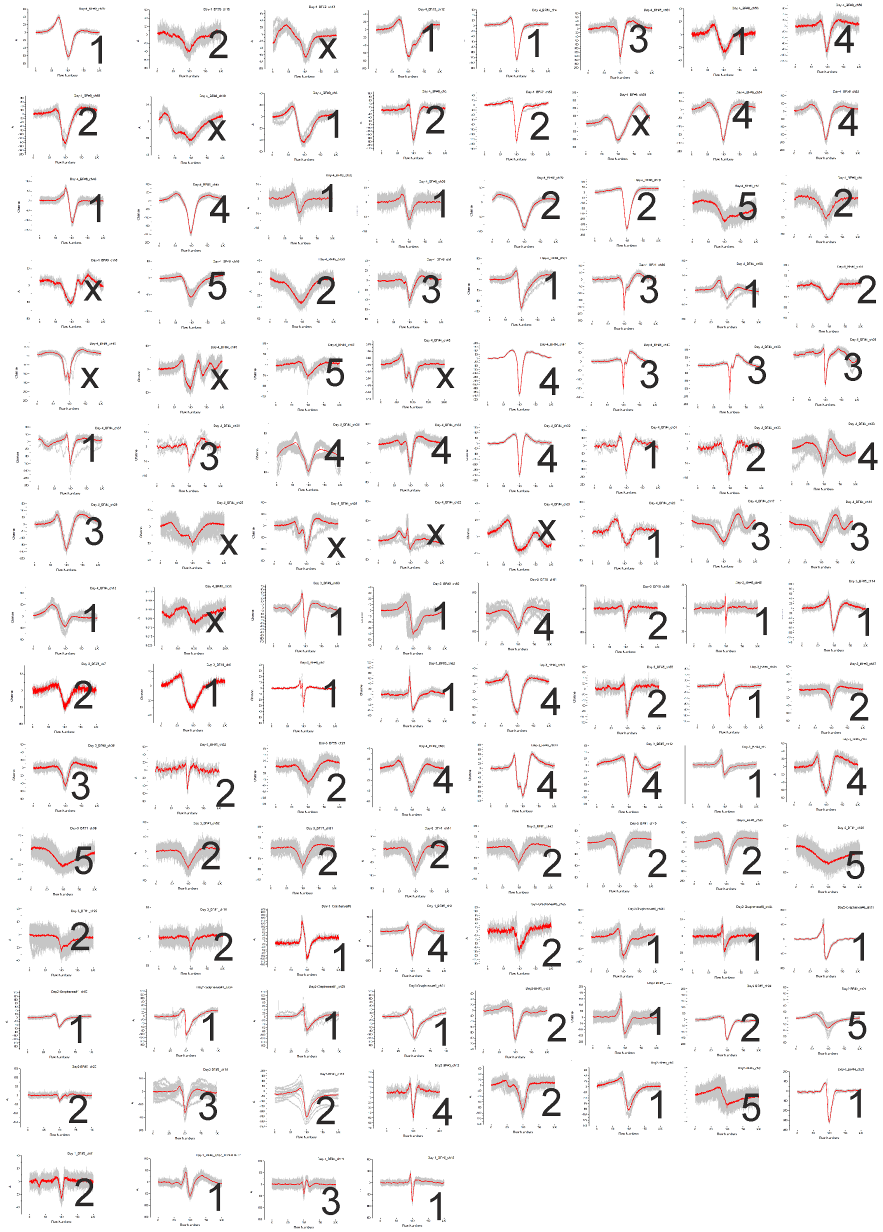

Figure F.2: The 116 unique AP of HL-1 cells, recorded by the GMEA devices. Five types of the spikes were selected as representing the difference.

Appendix G

MAD vs RMS

In our case, the noise values, throughout the thesis is estimated as 2×MAD (median average distribution), since the noise analysis was performed on a whole timetrace, without the selection of inter-spike regions for further analysis (see Figures G.1 and G.2 for two real examples). As visible from both examples, especially from Figure G.1, where large amplitude heart tissue APs are recorded, the root mean square (RMS) values are a poor estimate. In the most cases the RMS values are overestimating the real peak-to-peak noise. At the same time, the 2×MAD values in all of the cases exhibit the best fit and therefore were chosen for further analysis.

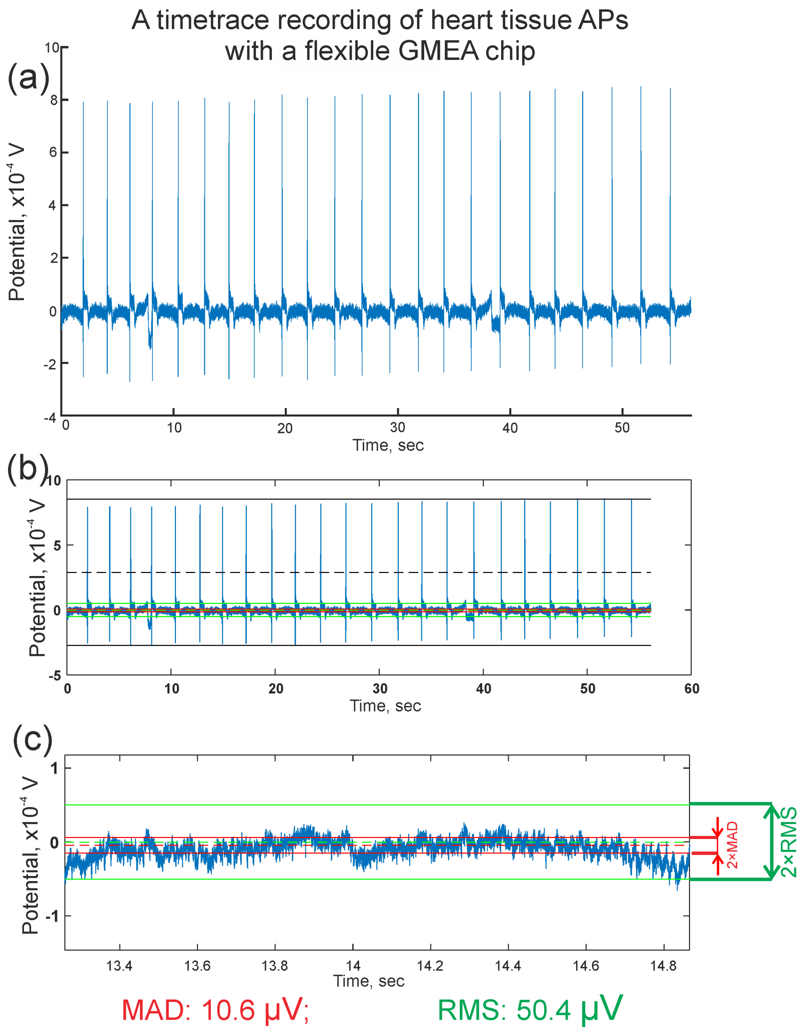

Figure G.1: Comparison of the RMS and MAD noise values for a heart-tissue recordings from a flexible GMEA chip (a). In (b) and (c) are given the results of noise analysis, where green horizontal lines represent RMS estimates, and red represent MAD estimates. The RMS value is 2.5 times larger that 2×MAD. The problem in this case is very large APs, resulting in huge overestimate for the RMS values.

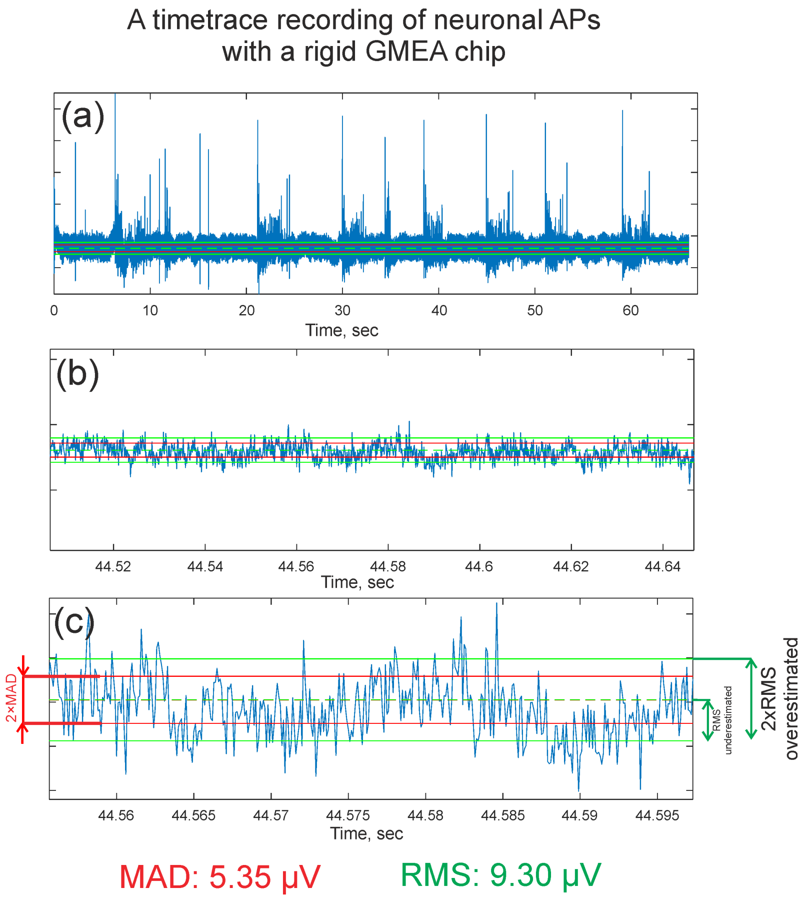

Figure G.2: In (a) a 60 second long recording with neuronal spiking-bursting activity is shown. The noise analysis is done on the whole timetrace. (b) gives a 10 ms zoom into a region without spikes. In (c) is shown just 4 ms so that individual noise peaks are visible. Green horizontal lines on each trace represent the RMS values, red horizontal lines mark the MAD values. In figures (b) and (c) is easily visible that 2×RMS value is much larger than actual peak-to-peak noise. However, in this case, an RMS value, on the other hand is found to be slightly smaller than the peak-to-peak noise (depends on culture and amount of spikes in the timetrace). The 2×MAD values are found to represent the actual peak-to-peak noise most accurately.

Appendix H

Cell culture, daily care and protocols

HL-1 cells

The HL-1 cells are artificially derived heart tumor cells. They are received in a frozen state, then thawed and cultured in T25 flasks until reaching confluency. As tumor cells, they double their amount per 24 hours. In order to transfer the cells onto a chip, or another flask and keep the cells growing it is important to split them.

Splitting HL-1 cells:

1. Prepare and warm up the supplemented Claycomb medium (see Table H.1);
2. Remove whole medium from the T25 flask, immediately add 1 ml of Trypsin/EDTA(0.05%) and leave for one minute;
3. Remove the 1 ml of Trypsin/EDTA(0.05%) and add another 1 ml of new Trypsin/EDTA(0.05%). Incubate at 37°C, 5% CO_2, for 5 minutes;
4. Add 5 ml of the warm Claycomb medium into the flask, slowly mix, then collect all 6 ml of the cellular solution and transfer into a 15 ml Falcon tube;
5. Centrifuge the solution at 500g (1700 rpm) for 5 minutes;
6. Remove the liquid, leaving the dense cellular pellet at the bottom;
7. Re-suspend the cells in 1 ml of new, warm Claycomb medium;
8. Count the amount of cells per volume using manual counter and hemocytometer.
9. **Make a new flask:**
   - Take a new T25 flask, fill in with 5 ml of the Claycomd medium;
   - Place a certain amount of cells (volume of the cellular solution) into the new flask. Use the following formula: $F = 1/2^{d-1}$, where F is the fraction of the cellular solution (1/2=500 µl; 1/8=125 µl), and calculate the day, d, at which the cells will be confluent again.

10. **Plate cells on chips:**
    - First, sterilize the chips in 70% Ethanol for at least 15 minutes;
    - *Protein Coating:*
      - Prepare solution of fibronectin and gelatin (5 µg/ml and 0.2 mg/ml) in double distilled water;
      - Incubate the protein solution on the chips at 37°C, 5% CO_2, for 1 hour;
      - Wash three times carefully with PBS (1x);
    - Place a certain amount of cells (volume of the cellular solution) on the chips. An approximate scaling by area can be applied in order to estimate the day of confluency. The usual initial density, the HL-1 cells are cultured on the chip's surface is in the range of 100-200 cells/mm^2 leads to a total culture of 3-4 days.

Table H.1: Supplemented Claycomb medium used for HL-1 cells. The listed below substances are added into Claycomb medium with specified concentrations.

Substance	**Add volume**	**Stock solution**	**Final Concentration**
Claycomb medium	100 ml	—	—
Fetal bovine serum	11.2 ml	—	10% (v/v)
Penicillin Streptomycin	1.14ml	10^4 units/ml 10^4 µg/ml	100 units/ml 100 µg/ml
Norepinephrine	1.14ml	10 mM	0.1 mM
L-glutamine	1.14ml	200 mM	2 mM

Cortical Rat Neurons

The primary cortical neurons are prepared from E18 Wistar rat embryos, mechanically dissociated and plated onto chips/substrates with certain concentrations.

1. Sterilize the chips in 70% Ethanol for at least 15 minutes;
2. *Protein coating*
   - Prepare solution 0.01 mg/ml of PDL, 0.004 mg/ml of gelatin, and 0.1 mg/ml of ECM in GBSS;
   - Apply the protein solution on the chips for 1 hour at room temperature;
   - Wash three times carefully with GBSS;
3. From the dissociated neuronal solution take a certain amount of cells (usually around 800 cells/µm^2), scaled to the seeding area, apply in a to the chips;

4. Let the chips for 10 minutes at room temperature for neuronal adhesion;
5. Transfer into 37°C, 5% CO_2 humidified incubator;
6. 2-3 hours after the seeding, replace the whole media with a fresh supplemented Neurobasal medium (see Table H.2);
7. Exchange half of the medium twice per week;
8. Prior to the measurements, the neurobasal medium is exchanged with extracellular patch solution (see Table H.3)

Table H.2: Supplemented Neurobasal medium used for embyonic cortical cells from rats. The medium was prepared by adding the listed substances to Neurobasal medium with specified concentrations.

Substance	Add volume	Stock solution	Final concentration
Neurobasal medium	10 ml	—	—
B27 supplement	100 µl	—	1 % (v/v)
L-glutamine	25 µl	200 mM	0.5 mM
gentamicin	10 µl	50 mg/ml	50 µg/ml

Table H.3: Recipe for extracellular patch solution used for embyonic cortical cells from rats. The reagents were dissolved in bi-distilled water, and the pH-value was adjusted to 7.4 with NaOH.

Substance	Extracellular concentration (mmol/L)
NaCl	125
KCl	3
$MgCl_2$	1
HEPES	10
$CaCl_2$	2

Terg-A-zyme cleaning

In order to carefully remove a cellular layer from a chip's surface after each culture, a Terg-A-zyme assisted cleaning is performed. Terg-A-zyme is a concentrated anionic detergent with protease enzyme typically used ultrasonic cleaning. The overall protocol is given below:

1. Prepare a 1% Terg-A-zyme solution in DI water;

2. Soak a chip in the 1% Terg-A-Zyme solution for at least one hour;

3. Rinse thoroughly with running water.

List of Chemicals

Table H.4: List of chemicals used for cell culture with embryonic rat cortical neurons and HL-1.

Substance	Supplier
ascorbic acid	Sigma-Aldrich
B27 supplement	Life Technologies
Claycomb medium	Sigma-Aldrich
ECM gel	Sigma-Aldrich
ethanol	Riedel-de Haën
fetal bovine serum	Life Technologies
fibronectin	Sigma-Aldrich
GBSS	Sigma-Aldrich
gelatin	Sigma-Aldrich
gentamicin	Sigma-Aldrich
glucose	Sigma-Aldrich
glutaraldehyde	Sigma-Aldrich
HBSS	Sigma-Aldrich
HEPES	Sigma-Aldrich
isopropanol	Merck
KCl	Sigma-Aldrich
KH_2PO_4	Sigma-Aldrich
L-glutamine	Life Technologies
$MgCl_2$	Sigma-Aldrich
NaCl	Sigma-Aldrich
NaOH	Sigma-Aldrich
Neurobasal medium	Life Technologies
norepinephrine	Sigma-Aldrich
PDL	Sigma-Aldrich
penicillin/streptomycin	Life Technologies
PLL	Sigma-Aldrich
trypan blue	Sigma-Aldrich
trypsin EDTA	Life Technologies

Table H.4: List of chemicals (continued).

Substance	Supplier
terg-A-zyme	Sigma-Aldrich

The chemicals used for all cell culture related protocols are listed here and were supplied by one of the following companies:

- Sigma-Aldrich Chemie GmbH, Taufkirchen, Germany (Sigma-Aldrich)
- Life Technologies GmbH, Darmstadt, Germany (Life Technologies)
- Merck KGaA, Darmstadt, Germany (Merck)

Table H.5: Recipe for phosphate buffered saline (PBS). The reagents were dissolved in bi-distilled water, and the pH-value was adjusted to 7.4 with NaOH.

Chemical	Concentration (mmol/l)
NaCl	137
KCl	2.7
Na_2HPO_4	8.1
KH_2PO_4	1.47

Ethics statement. The experiments were done with the approval of the Landesumweltamt für Natur, Umwelt und Verbraucherschutz Nordrhein-Westfalen, Recklinghausen, Germany, number 84-02.04.2015.A173.

Bibliography

[1] Neher, E. & Sakmann, B. Single-channel currents recorded from membrane of denervated frog muscle fibres. *Nature* **260**, 799–802 (1976). URL `http://www.nature.com/doifinder/10.1038/260799a0`.

[2] Hamill, O. P., Marty, A., Neher, E., Sakmann, B. & Sigworth, F. J. Improved patch-clamp techniques for high-resolution current recording from cells and cell-free membrane patches. *Pflügers Archiv - European Journal of Physiology* **391**, 85–100 (1981). URL `http://link.springer.com/10.1007/BF00656997`.

[3] Thomas, C. A., Springer, P. A., Loeb, G. E., Berwald-Netter, Y. & Okun, L. M. A miniature microelectrode array to monitor the bioelectric activity of cultured cells. *Experimental Cell Research* **74**, 61–66 (1972). URL `http://linkinghub.elsevier.com/retrieve/pii/0014482772904818`.

[4] Gross, G. W. Simultaneous Single Unit Recording in vitro with a Photoetched Laser Deinsulated Gold Multimicroelectrode Surface. *IEEE Transactions on Biomedical Engineering* **BME-26**, 273–279 (1979). URL `http://ieeexplore.ieee.org/lpdocs/epic03/wrapper.htm?arnumber=4123046`.

[5] Gross, G. W., Williams, A. N. & Lucas, J. H. Recording of spontaneous activity with photoetched microelectrode surfaces from mouse spinal neurons in culture. *Journal of Neuroscience Methods* **5**, 13–22 (1982). URL `http://linkinghub.elsevier.com/retrieve/pii/0165027082900462`.

[6] Pine, J. Recording action potentials from cultured neurons with extracellular microcircuit electrodes. *Journal of Neuroscience Methods* **2**, 19–31 (1980). URL `http://linkinghub.elsevier.com/retrieve/pii/0165027080900424`.

[7] Fromherz, P., Offenhäusser, A., Vetter, T. & Weis, J. A neuron-silicon junction: a Retzius cell of the leech on an insulated-gate field-effect transistor. *Science (New York, N.Y.)* **252**, 1290–1293 (1991). URL `http://www.sciencemag.org/cgi/doi/10.1126/science.1925540`.

[8] Offenhäusser, A., Sprössler, C., Matsuzawa, M. & Knoll, W. Field-effect transistor array for monitoring electrical activity from mammalian neurons in culture. *Biosensors and Bioelectronics* **12**, 819–826 (1997). URL `http://linkinghub.elsevier.com/retrieve/pii/S095656639700047X`.

[9] Offenhäusser, A. & Knoll, W. Cell-transistor hybrid systems and their potential applications. *Trends in Biotechnology* **19**, 62–66 (2001). URL `http://linkinghub.elsevier.com/retrieve/pii/S0167779900015444`.

[10] Egert, U. *et al.* A novel organotypic long-term culture of the rat hippocampus on substrate-integrated multielectrode arrays. *Brain Res. Protoc.* **2**, 229–242 (1998). URL `http://linkinghub.elsevier.com/retrieve/pii/S1385299X98000130`.

[11] Neumann, T., Ziegler, C. & Blau, A. Multielectrode array recordings reveal physiological diversity of intrinsically photosensitive retinal ganglion cells in the chick embryo. *Brain Research* **1207**, 120–127 (2008). URL `http://linkinghub.elsevier.com/retrieve/pii/S0006899308003739`.

[12] Natarajan, A., Molnar, P., Sieverdes, K., Jamshidi, A. & Hickman, J. Microelectrode array recordings of cardiac action potentials as a high throughput method to evaluate pesticide toxicity. *Toxicology in Vitro* **20**, 375–381 (2006). URL `http://linkinghub.elsevier.com/retrieve/pii/S0887233305001712`.

[13] Spira, M. E. & Hai, A. Multi-electrode array technologies for neuroscience and cardiology. *Nat. Nanotechnol.* **8**, 83–94 (2013). URL `http://dx.doi.org/10.1038/nnano.2012.265`.

[14] Obien, M. E. J., Deligkaris, K., Bullmann, T., Bakkum, D. J. & Frey, U. Revealing neuronal function through microelectrode array recordings. *Frontiers in Neuroscience* **8**, 423 (2015). URL `http://journal.frontiersin.org/article/10.3389/fnins.2014.00423/abstract`.

[15] Rutten, W. L. C. Selective electrical interfaces with the nervous system. *Annual review of biomedical engineering* **4**, 407–452 (2002). URL `http://www.ncbi.nlm.nih.gov/pubmed/12117764`.

[16] Frey, U., Egert, U., Heer, F., Hafizovic, S. & Hierlemann, A. Microelectronic system for high-resolution mapping of extracellular electric fields applied to brain slices. *Biosens. Bioelectron.* **24**, 2191–2198 (2009). URL `http://linkinghub.elsevier.com/retrieve/pii/S095656630800643X`.

[17] Brüggemann, D. *et al.* Nanostructured gold microelectrodes for extracellular recording from electrogenic cells. *Nanotechnology* **22**, 265104 (2011). URL `http://www.ncbi.nlm.nih.gov/pubmed/21586820`.

[18] Kim, J.-H., Kang, G., Nam, Y. & Choi, Y.-K. Surface-modified microelectrode array with flake nanostructure for neural recording and stimulation. *Nanotechnology* **21**, 85303 (2010). URL `http://www.ncbi.nlm.nih.gov/pubmed/20101076`.

[19] James, C. *et al.* Extracellular Recordings From Patterned Neuronal Networks Using Planar Microelectrode Arrays. *IEEE Transactions on Biomedical Engineering* **51**, 1640–1648 (2004). URL `http://ieeexplore.ieee.org/document/1325824/`.

[20] Berdondini, L. *et al.* Extracellular recordings from locally dense microelectrode arrays coupled to dissociated cortical cultures. *Journal of Neuroscience Methods* **177**, 386–396 (2009). URL `http://linkinghub.elsevier.com/retrieve/pii/S0165027008006432`.

[21] Ceyssens, F., Sree, S. P., Martens, J. & Puers, R. Fabrication of Nanostructured Platinum with Multilevel Porosity for Low Impedance Biomedical Recording and Stimulation Electrodes. *Procedia Engineering* **120**, 355–359 (2015). URL `http://linkinghub.elsevier.com/retrieve/pii/S1877705815022985`.

[22] Nguyen-Vu, T. D. B. *et al.* Vertically Aligned Carbon Nanofiber Arrays: An Advance toward Electrical-Neural Interfaces. *Small* **2**, 89–94 (2006). URL `http://doi.wiley.com/10.1002/smll.200500175`.

[23] Gabay, T. *et al.* Electro-chemical and biological properties of carbon nanotube based multi-electrode arrays. *Nanotechnology* **18**, 035201 (2007). URL `http://www.ncbi.nlm.nih.gov/pubmed/19636111`.

[24] Hofmann, B., Kätelhön, E., Schottdorf, M., Offenhäusser, A. & Wolfrum, B. Nanocavity electrode array for recording from electrogenic cells. *Lab Chip* **11**, 1054–1058 (2011). URL `http://www.ncbi.nlm.nih.gov/pubmed/21286648http://xlink.rsc.org/?DOI=c0lc00582g`.

[25] Czeschik, A. *et al.* Nanostructured cavity devices for extracellular stimulation of HL-1 cells. *Nanoscale* **7**, 9275–81 (2015). URL `http://pubs.rsc.org/en/Content/ArticleHTML/2015/NR/C5NR01690H`.

[26] Fendyur, A. & Spira, M. E. Toward on-chip, in-cell recordings from cultured cardiomyocytes by arrays of gold mushroom-shaped microelectrodes. *Frontiers in Neu-*

roengineering **5**, 1–10 (2012). URL `http://journal.frontiersin.org/article/10.3389/fneng.2012.00021/abstract`.

[27] Santoro, F. *et al.* Interfacing electrogenic cells with 3D nanoelectrodes: Position, shape, and size matter. *ACS Nano* **8**, 6713–6723 (2014). URL `http://pubs.acs.org/doi/abs/10.1021/nn500393p`.

[28] Shoval, A. *et al.* Carbon nanotube electrodes for effective interfacing with retinal tissue. *Frontiers in neuroengineering* **2**, 4 (2009). URL `http://journal.frontiersin.org/article/10.3389/neuro.16.004.2009/abstract`.

[29] David-Pur, M., Bareket-Keren, L., Beit-Yaakov, G., Raz-Prag, D. & Hanein, Y. All-carbon-nanotube flexible multi-electrode array for neuronal recording and stimulation. *Biomedical microdevices* **16**, 43–53 (2014). URL `http://link.springer.com/10.1007/s10544-013-9804-6`.

[30] Kim, T., Park, J., Sohn, J., Cho, D. & Jeon, S. Bioinspired, Highly Stretchable, and Conductive Dry Adhesives Based on 1D–2D Hybrid Carbon Nanocomposites for All–in–One ECG Electrodes. *ACS Nano* **10**, 4770–4778 (2016). URL `http://pubs.acs.org/doi/abs/10.1021/acsnano.6b01355`.

[31] Ingebrandt, S., Yeung, C. K., Krause, M. & Offenhäusser, A. Neuron-transistor coupling: Interpretation of individual extracellular recorded signals. *Eur. Biophys. J.* **34**, 144–154 (2005). URL `http://www.ncbi.nlm.nih.gov/pubmed/15459800`.

[32] Keyes, R. W. Physical limits of silicon transistors and circuits. *Reports on Progress in Physics* **68**, 2701–2746 (2005). URL `http://stacks.iop.org/0034-4885/68/i=12/a=R01?key=crossref.2616e1f5c0492983197fd500ea57cdfe`.

[33] He, Y. & Su, Y. *Silicon Nano-biotechnology*. SpringerBriefs in Molecular Science (Springer Berlin Heidelberg, Berlin, Heidelberg, 2014). URL `http://link.springer.com/10.1007/978-3-642-54668-6`.

[34] Lu, W., Xie, P. & Lieber, C. M. Nanowire Transistor Performance Limits and Applications. *IEEE Transactions on Electron Devices* **55**, 2859–2876 (2008). URL `http://ieeexplore.ieee.org/document/4668552/`.

[35] Zhang, A., Zheng, G. & M. Lieber, C. *Nanowires*. NanoScience and Technology (Springer International Publishing, Cham, 2016). URL `http://link.springer.com/10.1007/978-3-319-41981-7`.

[36] Zhou, W., Dai, X. & Lieber, C. M. Advances in nanowire bioelectronics. *Reports on Progress in Physics* **80**, 016701 (2017). URL `http://stacks.iop.org/0034-4885/80/i=1/a=016701?key=crossref.e7b8cb3e7b09303b0a4e664d543f900b`.

[37] Bianco, A. *et al.* All in the graphene family - A recommended nomenclature for two-dimensional carbon materials. *Carbon* **65**, 1–6 (2013). URL `http://linkinghub.elsevier.com/retrieve/pii/S0008622313008002`.

[38] Novoselov, K. S. *et al.* Electric Field Effect in Atomically Thin Carbon Films. *Science (80-.).* **306**, 666–669 (2004). URL `http://arxiv.org/ftp/cond-mat/papers/0410/0410550.pdf`.

[39] Servant, A., Bianco, A., Prato, M. & Kostarelos, K. Graphene for multi-functional synthetic biology: the last 'zeitgeist' in nanomedicine. *Bioorganic & medicinal chemistry letters* **24**, 1638–49 (2014). URL `http://www.ncbi.nlm.nih.gov/pubmed/24594351`.

[40] Li, N. *et al.* Graphene meets biology. *Chinese Science Bulletin* **59**, 1341–1354 (2014). URL `http://link.springer.com/10.1007/s11434-014-0158-0`.

[41] Duan, X., Fu, T.-M., Liu, J. & Lieber, C. M. Nanoelectronics-biology frontier: From nanoscopic probes for action potential recording in live cells to three-dimensional cyborg tissues. *Nano Today* **8**, 351–373 (2013). URL `http://linkinghub.elsevier.com/retrieve/pii/S1748013213000480`.

[42] Cohen-Karni, T., Qing, Q., Li, Q., Fang, Y. & Lieber, C. M. Graphene and Nanowire Transistors for Cellular Interfaces and Electrical Recording. *Nano Letters* **10**, 1098–1102 (2010). URL `http://pubs.acs.org/doi/abs/10.1021/nl1002608`.

[43] Hess, L. H. *et al.* Graphene transistor arrays for recording action potentials from electrogenic cells. *Advanced materials* **23**, 5045–9, 4968 (2011). URL `http://www.ncbi.nlm.nih.gov/pubmed/21953832`.

[44] Dankerl, M. *et al.* Graphene solution-gated field-effect transistor array for sensing applications. *Adv. Funct. Mater.* **20**, 3117–3124 (2010). URL `http://doi.wiley.com/10.1002/adfm.201000724`.

[45] Hess, L. H. *et al.* High-transconductance graphene solution-gated field effect transistors. *Appl. Phys. Lett.* **99**, 033503 (2011). URL `http://scitation.aip.org/content/aip/journal/apl/99/3/10.1063/1.3614445`.

[46] Kuzum, D. *et al.* Transparent and flexible low noise graphene electrodes for simultaneous electrophysiology and neuroimaging. *Nat. Commun.* **5**, 5259 (2014). URL `http://www.nature.com/doifinder/10.1038/ncomms6259`.

[47] Park, D.-W. *et al.* Graphene-based carbon-layered electrode array technology for neural imaging and optogenetic applications. *Nat. Commun.* **5**, 5258 (2014). URL `http://www.nature.com/doifinder/10.1038/ncomms6258`.

[48] Bendali, A. *et al.* Purified neurons can survive on peptide-free graphene layers. *Advanced healthcare materials* **2**, 929–33 (2013). URL `http://doi.wiley.com/10.1002/adhm.201200347`.

[49] Fabbro, A. *et al.* Graphene-Based interfaces do not alter target nerve cells. *ACS Nano* **10**, 615–623 (2016). URL `http://pubs.acs.org/doi/10.1021/acsnano.5b05647`.

[50] Veliev, F., Briançon-Marjollet, A., Bouchiat, V. & Delacour, C. Impact of crystalline quality on neuronal affinity of pristine graphene. *Biomaterials* **86**, 33–41 (2016). URL `http://www.sciencedirect.com/science/article/pii/S0142961216000569`.

[51] Fu, W. *et al.* Graphene transistors are insensitive to pH changes in solution. *Nano Letters* **11**, 3597–3600 (2011). URL `http://pubs.acs.org/doi/abs/10.1021/nl201332c`.

[52] Kireev, D. *et al.* Graphene field effect transistors for in vitro and ex vivo recordings. *IEEE Transactions on Nanotechnology* **17**, 140–147 (2016). URL `http://ieeexplore.ieee.org/document/7782310/`.

[53] Vieira, N. C. S. *et al.* Graphene field-effect transistor array with integrated electrolytic gates scaled to 200 mm. *J. Phys. Condens. Matter* **085302**, 85302 (2016). URL `http://dx.doi.org/10.1088/0953-8984/28/8/085302`.

[54] Stieglitz, T., Beutel, H., Schuettler, M. & Meyer, J.-U. Micromachined, Polyimide-Based Devices for Flexible Neural Interfaces. *Biomedical Microdevices* **2**, 283–294 (2000). URL `http://link.springer.com/article/10.1023/A:1009955222114`.

[55] Kireev, D. *et al.* High throughput transfer technique: Save your graphene. *Carbon N. Y.* **107**, 319–324 (2016). URL `http://www.sciencedirect.com/science/article/pii/S0008622316304249`.

[56] Kireev, D. *et al.* Versatile Flexible Graphene Multielectrode Arrays. *Biosensors* **7**, 1 (2017). URL `http://www.mdpi.com/2079-6374/7/1/1`.

[57] Kireev, D. *et al.* Graphene Multielectrode Arrays as a Versatile Tool for Extracellular Measurements. *Adv. Healthc. Mater.* **6**, 1601433 (2017). URL `http://doi.wiley.com/10.1002/adhm.201601433`.

[58] Kireev, D. *et al.* Graphene transistors for interfacing with cells: towards a deeper understanding of liquid gating and sensitivity. *Sci. Rep.* **7**, 6658 (2017). URL `http://www.nature.com/articles/s41598-017-06906-5`.

[59] Gogotsi, Y. & Presser, V. (eds.) *Carbon Nanomaterials* (Taylor & Francis Group, Boca Raton, F, 2014).

[60] Kroto, H. W., Heath, J. R., O'Brien, S. C., Curl, R. F. & Smalley, R. E. C60: Buckminsterfullerene. *Nature* **318**, 162–163 (1985). URL `http://www.nature.com/doifinder/10.1038/318162a0`.

[61] Iijima, S. Helical microtubules of graphitic carbon. *Nature* **354**, 56–58 (1991). URL `http://www.nature.com/doifinder/10.1038/354056a0`.

[62] Partoens, B. & Peeters, F. M. From graphene to graphite: Electronic structure around the K point. *Physical Review B* **74**, 075404 (2006). URL `http://link.aps.org/doi/10.1103/PhysRevB.74.075404`.

[63] Castro Neto, A. H., Guinea, F., Peres, N. M. R., Novoselov, K. S. & Geim, A. K. The electronic properties of graphene. *Rev. Mod. Phys.* **81**, 109–162 (2009). URL `http://link.aps.org/doi/10.1103/RevModPhys.81.109`. `0709.1163`.

[64] Reich, S., Maultzsch, J., Thomsen, C. & Ordejón, P. Tight-binding description of graphene. *Physical Review B* **66**, 035412 (2002). URL `http://link.aps.org/doi/10.1103/PhysRevB.66.035412`.

[65] Deacon, R. S., Chuang, K.-C., Nicholas, R. J., Novoselov, K. S. & Geim, A. K. Cyclotron resonance study of the electron and hole velocity in graphene monolayers. *Physical Review B* **76**, 081406 (2007). URL `http://link.aps.org/doi/10.1103/PhysRevB.76.081406`.

[66] Katsnelson, M. I. Graphene: carbon in two dimensions. *Materials Today* **10**, 20–27 (2007). URL `http://linkinghub.elsevier.com/retrieve/pii/S1369702106717886`.

[67] Eletskii, A. V., Iskandarova, I. M., Knizhnik, A. a. & Krasikov, D. N. Graphene: fabrication methods and thermophysical properties. *Physics-Uspekhi* **54**, 227–258 (2011). URL `http://stacks.iop.org/1063-7869/54/i=3/a=R01?key=crossref.06f34faa0c6b914d27e430554c52e6e7`.

[68] Avouris, P. Graphene: Electronic and photonic properties and devices. *Nano Lett.* **10**, 4285–4294 (2010). URL `http://pubs.acs.org/doi/abs/10.1021/nl102824h`.

[69] Avouris, P. & Dimitrakopoulos, C. Graphene: synthesis and applications. *Materials Today* **15**, 86–97 (2012). URL `http://linkinghub.elsevier.com/retrieve/pii/S1369702112700445`.

[70] Norimatsu, W. & Kusunoki, M. Epitaxial graphene on SiC{0001}: advances and perspectives. *Physical Chemistry Chemical Physics* **16**, 3501 (2014). URL `http://xlink.rsc.org/?DOI=c3cp54523g`.

[71] Wu, T. *et al.* Fast growth of inch-sized single-crystalline graphene from a controlled single nucleus on Cu-Ni alloys. *Nature Materials* **15**, 43–47 (2015). URL `http://dx.doi.org/10.1038/nmat4477`.

[72] Sham, A. Y. W. & Notley, S. M. A review of fundamental properties and applications of polymer-graphene hybrid materials. *Soft Matter* **9**, 6645 (2013). URL `http://xlink.rsc.org/?DOI=c3sm00092c`.

[73] Mattevi, C., Kim, H. & Chhowalla, M. A review of chemical vapour deposition of graphene on copper. *Journal of Materials Chemistry* **21**, 3324 (2011). URL `http://xlink.rsc.org/?DOI=c0jm02126a`.

[74] Somani, P. R., Somani, S. P. & Umeno, M. Planer nano-graphenes from camphor by CVD. *Chemical Physics Letters* **430**, 56–59 (2006). URL `http://linkinghub.elsevier.com/retrieve/pii/S0009261406009018`.

[75] Pierce, J. The naming of the transistor. *Proceedings of the IEEE* **86**, 37–45 (1998). URL `http://ieeexplore.ieee.org/document/658756/`.

[76] Esmaeilzadeh, H., Blem, E., St. Amant, R., Sankaralingam, K. & Burger, D. Dark Silicon and the End of Multicore Scaling. *IEEE Micro* **32**, 122–134 (2012). URL `http://ieeexplore.ieee.org/document/6175879/`.

[77] Tans, S., Verschueren, A. & Dekker, C. Room-temperature transistor based on a single carbon nanotube. *Nature* **672**, 669–672 (1998). URL `http://www.nature.com/doifinder/10.1038/29954`.

[78] Bolotin, K. *et al.* Ultrahigh electron mobility in suspended graphene. *Solid State Communications* **146**, 351–355 (2008). URL `http://linkinghub.elsevier.com/retrieve/pii/S0038109808001178`.

[79] Banszerus, L. *et al.* Ultrahigh-mobility graphene devices from chemical vapor deposition on reusable copper. *Science Advances* **1**, e1500222–e1500222 (2015). URL `http://advances.sciencemag.org/cgi/doi/10.1126/sciadv.1500222`.

[80] Morozov, S. V. *et al.* Giant Intrinsic Carrier Mobilities in Graphene and Its Bilayer. *Physical Review Letters* **100**, 016602 (2008). URL `http://link.aps.org/doi/10.1103/PhysRevLett.100.016602`.

[81] Long, M.-q., Tang, L., Wang, D., Wang, L. & Shuai, Z. Theoretical Predictions of Size-Dependent Carrier Mobility and Polarity in Graphene. *Journal of the American Chemical Society* **131**, 17728–17729 (2009). URL `http://pubs.acs.org/doi/abs/10.1021/ja907528a`.

[82] Schwierz, F. Graphene transistors. *Nat. Nanotechnol.* **5**, 487–496 (2010). URL `http://www.nature.com/nnano/journal/v5/n7/full/nnano.2010.89.html`.

[83] Ramayya, E. B., Vasileska, D., Goodnick, S. M. & Knezevic, I. Electron Mobility in Silicon Nanowires. *IEEE Transactions On Nanotechnology* **6**, 113–117 (2007). URL `http://ieeexplore.ieee.org/document/4063341/`.

[84] Kim, K., Choi, J.-Y., Kim, T., Cho, S.-H. & Chung, H.-J. A role for graphene in silicon-based semiconductor devices. *Nature* **479**, 338–44 (2011). URL `http://www.ncbi.nlm.nih.gov/pubmed/22094694`.

[85] Hess, L. H., Seifert, M. & Garrido, J. A. Graphene transistors for bioelectronics. *Proc. IEEE* **101**, 1780–1792 (2013). URL `http://ieeexplore.ieee.org/lpdocs/epic03/wrapper.htm?arnumber=6518189`.

[86] Xia, J., Chen, F., Li, J. & Tao, N. Measurement of the quantum capacitance of graphene. *Nat Nanotechnol* **4**, 505–509 (2009). URL `http://www.ncbi.nlm.nih.gov/pubmed/19662012`.

[87] Luryi, S. Quantum capacitance devices. *Applied Physics Letters* **52**, 501–503 (1988). URL `http://aip.scitation.org/doi/10.1063/1.99649`.

[88] Israelachvili, J. N. Electrostatic Forces between Surfaces in Liquids. In *Intermolecular and Surface Forces*, chap. 14, 291–340 (Elsevier, Oxford, 2011), 3 edn. URL `http://linkinghub.elsevier.com/retrieve/pii/B9780123751829100144`.

[89] Bard, A. J. & Faulkner, L. R. *Electrochemical Methods: Fundamentals and Applications* (Wiley, 2000). URL `https://books.google.de/books?id=kv56QgAACAAJ`.

[90] Helmholtz, H. Studien über electrische Grenzschichten. *Annalen der Physik und Chemie* **243**, 337–382 (1879). URL `http://doi.wiley.com/10.1002/andp.18792430702`.

[91] Gouy, M. Sur la constitution de la charge électrique à la surface d'un électrolyte. *Journal de Physique Théorique et Appliquée* **9**, 457–468 (1910). URL `http://www.edpsciences.org/10.1051/jphystap:019100090045700`.

[92] Chapman, D. L. LI. A contribution to the theory of electrocapillarity. *Philosophical Magazine Series 6* **25**, 475–481 (1913). URL `http://www.tandfonline.com/doi/abs/10.1080/14786440408634187`.

[93] Stern, O. Zur Theorie der Elektrolytischen Doppelschicht. *Zeitschrift für Elektrochemie und angewandte physikalische Chemie* **30**, 508–516 (1924). URL `http://dx.doi.org/10.1002/bbpc.192400182`.

[94] Nakamura, M., Sato, N., Hoshi, N. & Sakata, O. Outer Helmholtz Plane of the Electrical Double Layer Formed at the Solid Electrode-Liquid Interface. *ChemPhysChem* **12**, 1430–1434 (2011). URL `http://doi.wiley.com/10.1002/cphc.201100011`.

[95] Kandel, E. R., Schwartz, J. H. & Jessel, T. M. *Principles of Neural Science* (McGraw-Hill, Health Professions Division, New York, 4 edition, 2000).

[96] Dudel, J. Innerneurale Homeostase und Kommunikation, Erregung. In Schmidt, R. F. (ed.) *Neuro- und Sinnesphysiologie*, 31–58 (Springer Berlin Heidelberg, Berlin, Heidelberg, 1998). URL `http://link.springer.com/10.1007/978-3-662-22216-4_2`.

[97] Hodgkin, A. L. & Huxley, A. F. A quantitative description of membrane current and its application to conduction and excitation in nerve. *J. Physiol.* **117**, 500–544 (1952).

[98] Polder, H. R., Weskamp, M., Linz, K. & Meyer, R. Voltage-Clamp and Patch-Clamp Techniques. In *Practical Methods in Cardiovascular Research*, 272–323 (Springer-Verlag, Berlin/Heidelberg, 2005). URL `http://link.springer.com/10.1007/3-540-26574-0_16`.

[99] Wang, P. & Liu, Q. *Cell-Based Biosensors: principles and applications* (Artech House, Boston, MA, 2009).

[100] Fromherz, P. Extracellular recording with transistors and the distribution of ionic conductances in a cell membrane. *European Biophysics Journal* **28**, 254–258 (1999). URL `http://link.springer.com/10.1007/s002490050206`.

[101] Hofmann, B. *et al.* Light induced stimulation and delay of cardiac activity. *Lab on a Chip* **10**, 2588 (2010). URL `http://xlink.rsc.org/?DOI=c003091k`.

[102] Maybeck, V. *Tools for Non-Invasive Communication with Electrogenetic Cells: Optogenetic Stimulation and Diamond Recording Devices*. Ph.D. thesis, RWTH Aachen, Aachen (2011). URL `http://juser.fz-juelich.de/record/16833`.

[103] Czeschik, A. *Nanocavity Arrays for Extracellular Recording and Stimulation of Electroactive Cell Systems*. Ph.D. thesis, RWTH Aachen, Aachen (2016). URL `http://juser.fz-juelich.de/record/205052`.

[104] Bae, S. *et al.* Roll-to-roll production of 30-inch graphene films for transparent electrodes. *Nat. Nanotechnol.* **5**, 574–578 (2010). URL `http://www.nature.com/doifinder/10.1038/nnano.2010.132`.

[105] Li, X. *et al.* Large-Area Synthesis of High-Quality and Uniform Graphene Films on Copper Foils. *Science* **324**, 1312–1314 (2009). URL `http://www.sciencemag.org/cgi/doi/10.1126/science.1171245`.

[106] Liang, X. *et al.* Toward clean and crackless transfer of graphene. *ACS Nano* **5**, 9144–9153 (2011). URL `http://www.ncbi.nlm.nih.gov/pubmed/21999646`.

[107] Vitusevich, S. A. *et al.* Excess low-frequency noise in AlGaN/GaN-based high-electron-mobility transistors. *Appl. Phys. Lett.* **80**, 2126–2128 (2002). URL `http://aip.scitation.org/doi/10.1063/1.1463202`.

[108] Eick, S. *Extracellular Stimulation of Individual Electrogenic Cells with Micro-Scaled Electrodes*. Ph.D. thesis, RWTH Aachen, Aachen (2009).

[109] Ecken, H. *et al.* 64-Channel Extended Gate Electrode Arrays for Extracellular Signal Recording. *Electrochim. Acta* **48**, 3355–3362 (2003). URL `http://linkinghub.elsevier.com/retrieve/pii/S0013468603004055`.

[110] Krause, M. Extended gate electrode arrays for extracellular signal recordings. *Sensors Actuators B Chem.* **70**, 101–107 (2000). URL `http://linkinghub.elsevier.com/retrieve/pii/S0925400500005682`.

[111] Brewer, G. J., Torricelli, J. R., Evege, E. K. & Price, P. J. Optimized survival of hippocampal neurons in B27-supplemented Neurobasal, a new serum-free medium combination. *J. Neurosci. Res.* **35**, 567–76 (1993). URL `http://www.ncbi.nlm.nih.gov/pubmed/8377226`.

[112] Bittermann, A. G., Burkhardt, C. & Hall, H. Imaging of Cell-to-Material Interfaces by SEM after in situ Focused Ion Beam Milling on Flat Surfaces and Complex 3D-Fibrous Structures. *Adv. Eng. Mater.* **11**, B182–B188 (2009). URL `http://doi.wiley.com/10.1002/adem.200900080`.

[113] Randviir, E. P., Brownson, D. A. C. & Banks, C. E. A decade of graphene research: Production, applications and outlook. *Materials Today* **17**, 426–432 (2014). URL `http://dx.doi.org/10.1016/j.mattod.2014.06.001`.

[114] Geim, A. K. Graphene: Status and prospects. *Science* **324**, 1530–1534 (2009). URL `http://science.sciencemag.org/content/324/5934/1530`.

[115] Bonaccorso, F. *et al.* Production and processing of graphene and 2d crystals. *Materials Today* **15**, 564–589 (2012). URL `http://linkinghub.elsevier.com/retrieve/pii/S1369702113700142`.

[116] Novoselov, K. S. *et al.* Two-dimensional gas of massless Dirac fermions in graphene. *Nature* **438**, 197–200 (2005). URL `http://www.nature.com/doifinder/10.1038/nature04233`.

[117] Arvidsson, R., Molander, S. & Sandén, B. A. Review of Potential Environmental and Health Risks of the Nanomaterial Graphene. *Human and Ecological Risk Assessment: An International Journal* (2013). URL `http://www.tandfonline.com/doi/abs/10.1080/10807039.2012.702039`.

[118] Allen, M. J., Tung, V. C. & Kaner, R. B. Honeycomb Carbon: A Review of Graphene. *Chemical Reviews* **110**, 132–145 (2010). URL `http://pubs.acs.org/doi/abs/10.1021/cr900070d`.

[119] Zhang, Y., Zhang, L. & Zhou, C. Review of chemical vapor deposition of graphene and related applications. *Accounts of Chemical Research* **46**, 2329–2339 (2013). URL `http://www.ncbi.nlm.nih.gov/pubmed/23480816`.

[120] Kobayashi, T. *et al.* Production of a 100-m-long high-quality graphene transparent conductive film by roll-to-roll chemical vapor deposition and transfer process. *Applied Physics Letters* **102**, 023112 (2013). URL `http://scitation.aip.org/content/aip/journal/apl/102/2/10.1063/1.4776707`.

[121] Wang, L. *et al.* Facile preparation of an n-type reduced graphene oxide field effect transistor at room temperature. *Chem. Commun.* **50**, 1224–1226 (2014). URL `http://pubs.rsc.org/en/content/articlehtml/2014/cc/c3cc47224h`.

[122] Hao, Y. *et al.* The Role of Surface Oxygen in the Growth of Large Single-Crystal Graphene on Copper. *Science* **342**, 720–723 (2013). URL `http://www.sciencemag.org/content/342/6159/720.short`.

[123] Zhang, Y. H. *et al.* Controllable growth of millimeter-size graphene domains on Cufoil. *Materials Letters* **96**, 149–151 (2013). URL `http://linkinghub.elsevier.com/retrieve/pii/S0167577X13000438`.

[124] Kang, J., Shin, D., Bae, S. & Hong, B. H. Graphene transfer: key for applications. *Nanoscale* **4**, 5527–5537 (2012). URL `http://www.ncbi.nlm.nih.gov/pubmed/22864991`.

[125] Wood, J. D. *et al.* Annealing free, clean graphene transfer using alternative polymer scaffolds. *Nanotechnology* **26**, 055302 (2015). URL `http://iopscience.iop.org/article/10.1088/0957-4484/26/5/055302`.

[126] Her, M., Beams, R. & Novotny, L. Graphene transfer with reduced residue. *Phys. Lett. Sect. A Gen. At. Solid State Phys.* **377**, 1455–1458 (2013). URL `http://linkinghub.elsevier.com/retrieve/pii/S0375960113003617`.

[127] Lin, Y.-C. *et al.* Graphene Annealing: How Clean Can It Be? *Nano Letters* **12**, 414–419 (2012). URL `http://pubs.acs.org/doi/abs/10.1021/nl203733r`.

[128] Lee, J. *et al.* Crack-Release Transfer Method of Wafer-Scale Grown Graphene Onto Large-Area Substrates. *ACS Applied Materials & Interfaces* **6**, 12588–12593 (2014). URL `http://pubs.acs.org/doi/abs/10.1021/am502565z`.

[129] Barin, G. B. *et al.* Optimized graphene transfer: Influence of polymethylmethacrylate (PMMA) layer concentration and baking time on grapheme final performance. *Carbon N. Y.* **84**, 82–90 (2015). URL `http://linkinghub.elsevier.com/retrieve/pii/S0008622314011269`.

[130] Zaretski, A. V. & Lipomi, D. J. Processes for non-destructive transfer of graphene: widening the bottleneck for industrial scale production. *Nanoscale* **7**, 9963–9969 (2015). URL `http://xlink.rsc.org/?DOI=C5NR01777G`.

[131] Lee, S. *et al.* Graphene transfer in vacuum yielding a high quality graphene. *Carbon N. Y.* **93**, 286–294 (2015). URL `http://linkinghub.elsevier.com/retrieve/pii/S0008622315004352`.

[132] Chen, X.-D. *et al.* The selective transfer of patterned graphene. *Scientific reports* **3**, 3216 (2013). URL `http://www.nature.com/articles/srep03216`.

[133] Pizzocchero, F. *et al.* Non-destructive electrochemical graphene transfer from reusable thin-film catalysts. *Carbon* **85**, 397–405 (2015). URL `http://www.sciencedirect.com/science/article/pii/S0008622314012226`.

[134] Zhan, Z. *et al.* Pore-free bubbling delamination of chemical vapor deposited graphene from copper foils. *J. Mater. Chem. C* **3**, 8634–8641 (2015). URL `http://xlink.rsc.org/?DOI=C5TC01771H`.

[135] Sharma, B. K. & Ahn, J.-H. Graphene based field effect transistors: Efforts made towards flexible electronics. *Solid. State. Electron.* **89**, 177–188 (2013). URL `http://linkinghub.elsevier.com/retrieve/pii/S0038110113002803`.

[136] Lin, Y.-M. *et al.* 100 GHz Transistors from Wafer Scale Epitaxial Graphene. *Science* **327**, 662 (2010). URL `http://www.sciencemag.org/cgi/doi/10.1126/science.327.5966.734-b`.

[137] Hwang, W. S. *et al.* Graphene nanoribbon field-effect transistors on wafer-scale epitaxial graphene on SiC substrates a. *APL Mater.* **3**, 011101 (2015). URL `http://scitation.aip.org/content/aip/journal/aplmater/3/1/10.1063/1.4905155`.

[138] Avsar, A. *et al.* Toward Wafer Scale Fabrication of Graphene Based Spin Valve Devices. *Nano Lett.* **11**, 2363–2368 (2011). URL `http://pubs.acs.org/doi/abs/10.1021/nl200714q`.

[139] Smith, A. D., Vaziri, S., Rodriguez, S., Östling, M. & Lemme, M. C. Large scale integration of graphene transistors for potential applications in the back end of the line. *Solid. State. Electron.* **108**, 61–66 (2015). URL `http://www.sciencedirect.com/science/article/pii/S0038110114003074`.

[140] Wang, X. *et al.* Large-Scale Synthesis of Few-Layered Graphene using CVD. *Chemical Vapor Deposition* **15**, 53–56 (2009). URL `http://doi.wiley.com/10.1002/cvde.200806737`.

[141] Cheng, J. *et al.* Flexible solution-gated graphene field effect transistor for electrophysiological recording. *J. Microelectromechanical Syst.* **23**, 1311–1317 (2014). URL `http://ieeexplore.ieee.org/lpdocs/epic03/wrapper.htm?arnumber=6783801`.

[142] Cheng, Z. *et al.* Sensitivity limits and scaling of bioelectronic graphene transducers. *Nano Lett.* **13**, 2902–2907 (2013). URL `http://www.ncbi.nlm.nih.gov/pubmed/23638876`.

[143] Khodagholy, D. *et al.* High transconductance organic electrochemical transistors. *Nat. Commun.* **4**, 2133 (2013). URL `http://www.nature.com/doifinder/10.1038/ncomms3133`.

[144] Wang, H. & Pilon, L. Accurate Simulations of Electric Double Layer Capacitance of Ultramicroelectrodes. *The Journal of Physical Chemistry C* **115**, 16711–16719 (2011). URL `http://pubs.acs.org/doi/abs/10.1021/jp204498e`.

[145] Schroder, D. K. Contact Resistance and Schottky Barriers. In *Semiconductor Material and Device Characterization*, 127–184 (John Wiley & Sons, Inc., Hoboken, NJ, USA, 2005). URL `http://doi.wiley.com/10.1002/0471749095.ch3`.

[146] Ohno, Y., Maehashi, K., Yamashiro, Y. & Matsumoto, K. Electrolyte-gated graphene field-effect transistors for detecting ph and protein adsorption. *Nano Lett.* **9**, 3318–3322 (2009). URL `http://pubs.acs.org/doi/abs/10.1021/nl901596m.0606284v1`.

[147] Blaschke, B. M. *et al.* Flexible graphene transistors for recording cell action potentials. *2D Mater.* **3**, 025007 (2016). URL `http://stacks.iop.org/2053-1583/3/i=2/a=025007?key=crossref.809cc7aaa19e68ab49b72000ec6b2d02`.

[148] Brown, M. A., Crosser, M. S., Leyden, M. R., Qi, Y. & Minot, E. D. Measurement of high carrier mobility in graphene in an aqueous electrolyte environment. *Applied Physics Letters* **109**, 093104 (2016). URL `http://scitation.aip.org/content/aip/journal/apl/109/9/10.1063/1.4962141`.

[149] Eschermann, J. F. *et al.* Action potentials of HL-1 cells recorded with silicon nanowire transistors. *Appl. Phys. Lett.* **95**, 083703 (2009). URL `http://scitation.aip.org/content/aip/journal/apl/95/8/10.1063/1.3194138`.

[150] Sprössler, C., Denyer, M., Britland, S., Knoll, W. & Offenhäusser, A. Electrical recordings from rat cardiac muscle cells using field-effect transistors. *Phys. Rev. E. Stat. Phys. Plasmas. Fluids. Relat. Interdiscip. Topics* **60**, 2171–2176 (1999). URL `http://www.ncbi.nlm.nih.gov/pubmed/11970010`.

[151] Schottdorf, M., Hofmann, B., Kätelhön, E., Offenhäusser, A. & Wolfrum, B. Frequency-dependent signal transfer at the interface between electrogenic cells and nanocavity electrodes. *Phys. Rev. E - Stat. Nonlinear, Soft Matter Phys.* **85**, 031917 (2012). URL `http://link.aps.org/doi/10.1103/PhysRevE.85.031917`.

[152] Maybeck, V. *et al.* Boron-doped nanocrystalline diamond microelectrode arrays monitor cardiac action potentials. *Adv. Healthc. Mater.* **3**, 283–289 (2014). URL `http://doi.wiley.com/10.1002/adhm.201300062`.

[153] Natarajan, A. R., Rong, Q., Katchman, A. N. & Ebert, S. N. Intrinsic cardiac catecholamines help maintain beating activity in neonatal rat cardiomyocyte cultures. *Pediatric research* **56**, 411–7 (2004). URL `http://www.ncbi.nlm.nih.gov/pubmed/15333759`.

[154] Stuart, G., Spruston, N., Sakmann, B. & Häusser, M. Action potential initiation and backpropagation in neurons of the mammalian CNS. *Trends in Neurosciences* **20**, 125–131 (1997). URL `http://linkinghub.elsevier.com/retrieve/pii/S0166223696100758`.

[155] Dankerl, M. *et al.* Diamond transistor array for extracellular recording from electrogenic cells. *Adv. Funct. Mater.* **19**, 2915–2923 (2009). URL `http://doi.wiley.com/10.1002/adfm.200900590`.

[156] Claycomb, W. C. *et al.* HL-1 cells: a cardiac muscle cell line that contracts and retains phenotypic characteristics of the adult cardiomyocyte. *Proc Natl Acad Sci USA* **95**, 2979–2984 (1998). URL `http://www.pnas.org/content/95/6/2979.long`.

[157] Ghosh, M. *Polyimides: Fundamentals and Applications*. Plastics Engineering (Taylor & Francis, 1996). URL `https://books.google.de/books?id=H1K4YNfY-JgC`.

[158] Guo, B., Fang, L., Zhang, B. & Gong, J. R. Graphene Doping: A Review. *Insciences Journal* **1**, 80–89 (2011). URL `http://journal.insciences.org/1664-171x-1-2-80/`.

[159] Fratini, S. & Guinea, F. Substrate-limited electron dynamics in graphene. *Physical Review B* **77**, 195415 (2008). URL `http://link.aps.org/doi/10.1103/PhysRevB.77.195415`.

[160] Jang, C., Xiao, S., Ishigami, M. & Fuhrer, M. S. Intrinsic and extrinsic performance limits of graphene devices on SiO2. *Nature nanotechnology* **3**, 206–9 (2008). URL `http://www.ncbi.nlm.nih.gov/pubmed/18654504`.

[161] Hwang, E. H., Adam, S. & Sarma, S. D. Carrier Transport in Two-Dimensional Graphene Layers. *Physical Review Letters* **98**, 186806 (2007). URL `http://link.aps.org/doi/10.1103/PhysRevLett.98.186806`.

[162] Pallecchi, E. *et al.* Graphene microwave transistors on sapphire substrates. *Applied Physics Letters* **99**, 113502 (2011). URL `http://scitation.aip.org/content/aip/journal/apl/99/11/10.1063/1.3633105`.

[163] Zhang, Y., Mendez, E. E. & Du, X. Mobility-dependent low-frequency noise in graphene field-effect transistors. *ACS Nano* **5**, 8124–8130 (2011). URL `http://www.ncbi.nlm.nih.gov/pubmed/24345726`.

[164] Timko, B. P. *et al.* Electrical recording from hearts with flexible nanowire device arrays. *Nano Lett.* **9**, 914–918 (2009). URL `http://pubs.acs.org/doi/abs/10.1021/nl900096z`.

[165] Blake, P. *et al.* Making graphene visible. *Appl. Phys. Lett.* **91**, 063124 (2007). URL `http://aip.scitation.org/doi/10.1063/1.2768624`.

[166] Bulai, P. M., Molchanov, P. G., Denisov, A. A., Pitlik, T. N. & Cherenkevich, S. N. Extracellular electrical signals in a neuron-surface junction: model of heterogeneous membrane conductivity. *European Biophysics Journal* **41**, 319–327 (2012). URL `http://link.springer.com/10.1007/s00249-012-0787-7`.

[167] Puglisi, J. L., Wang, F. & Bers, D. M. Modeling the isolated cardiac myocyte. *Progress in Biophysics and Molecular Biology* **85**, 163–178 (2004). URL `http://linkinghub.elsevier.com/retrieve/pii/S0079610703001147`.

[168] Xie, C., Lin, Z., Hanson, L., Cui, Y. & Cui, B. Intracellular recording of action potentials by nanopillar electroporation. *Nature nanotechnology* **7**, 185–90 (2012). URL `http://www.nature.com/doifinder/10.1038/nnano.2012.8`.

[169] Du, X., Guo, H., Jin, Y., Jin, Q. & Zhao, J. Electrochemistry Investigation on the Graphene/Electrolyte Interface. *Electroanalysis* **27**, 2760–2765 (2015). URL `http://doi.wiley.com/10.1002/elan.201500302`.

[170] Droge, M. H., Gross, G. W., Hightower, M. H. & Czisny, L. E. Multielectrode analysis of coordinated, multisite, rhythmic bursting in cultured CNS monolayer networks. *The Journal of neuroscience : the official journal of the Society for Neuroscience* **6**, 1583–92 (1986). URL `http://www.ncbi.nlm.nih.gov/pubmed/3711997`.

[171] Chiappalone, M., Bove, M., Vato, A., Tedesco, M. & Martinoia, S. Dissociated cortical networks show spontaneously correlated activity patterns during in vitro development. *Brain Research* **1093**, 41–53 (2006). URL `http://linkinghub.elsevier.com/retrieve/pii/S0006899306008018`.

[172] Pasquale, V., Massobrio, P., Bologna, L., Chiappalone, M. & Martinoia, S. Self-organization and neuronal avalanches in networks of dissociated cortical neurons. *Neuroscience* **153**, 1354–1369 (2008). URL `http://linkinghub.elsevier.com/retrieve/pii/S0306452208004028`.

[173] VanPelt, J., Wolters, P., Corner, M., Rutten, W. & Ramakers, G. Long-Term Characterization of Firing Dynamics of Spontaneous Bursts in Cultured Neural Networks. *IEEE Transactions on Biomedical Engineering* **51**, 2051–2062 (2004). URL `http://ieeexplore.ieee.org/document/1344208/`.

[174] Ruch, T. C. & Patton, H. D. *Physiology and biophysics* (Saunders (W.B.) Co Ltd, Philadelphia, 20 edition, 1982).

[175] Wheeler, B. C. & Nam, Y. In Vitro Microelectrode Array Technology and Neural Recordings. *Crit. Rev. Biomed. Eng.* **39**, 45–61 (2011). URL `http://www.dl.begellhouse.com/journals/4b27cbfc562e21b8,7d5e987c7e576915,41cf5d45336340f0.html`.

[176] Massobrio, P., Massobrio, G. & Martinoia, S. Interfacing cultured neurons to microtransducers arrays: A review of the neuro-electronic junction models. *Front. Neurosci.* **10**, 1–13 (2016). URL `http://journal.frontiersin.org/Article/10.3389/fnins.2016.00282/abstract`.

[177] Fromherz, P. Three Levels of Neuroelectronic Interfacing: Silicon Chips with Ion Channels, Nerve Cells, and Brain Tissue. *Annals of the New York Academy of Sciences* **1093**, 143–160 (2006). URL `http://doi.wiley.com/10.1196/annals.1382.011`.

[178] Du, X. *et al.* Graphene microelectrode arrays for neural activity detection. *J. Biol. Phys.* **41**, 339–347 (2015). URL `http://link.springer.com/10.1007/s10867-015-9382-3`.

[179] Bareket-Keren, L. & Hanein, Y. Carbon nanotube-based multi electrode arrays for neuronal interfacing: progress and prospects. *Front. Neural Circuits* **6**, 122 (2012). URL `http://journal.frontiersin.org/article/10.3389/fncir.2012.00122/abstract`.

[180] Yi, W. *et al.* A flexible and implantable microelectrode arrays using high-temperature grown vertical carbon nanotubes and a biocompatible polymer substrate. *Nanotechnology* **26**, 125301 (2015). URL `http://www.ncbi.nlm.nih.gov/pubmed/25742874`.

[181] Crosser, M. S., Brown, M. A., McEuen, P. L. & Minot, E. D. Determination of the Thermal Noise Limit of Graphene Biotransistors. *Nano Letters* **15**, 5404–5407 (2015). URL `http://pubs.acs.org/doi/abs/10.1021/acs.nanolett.5b01788`.

[182] Werth, G. & Dadgar, P. Zum Elektrokardiogramm der Ratte mit und ohne Narkose, bei Beatmung mit Sauerstoffmangelgemischen sowie bei Intoxikation mit Malachitgruen, unter gleichzeitiger Bestimmung des effektiven Sauerstoffverbrauches. *Arch. fur Kreislaufforsch.* **48**, 118–131 (1965). URL `http://link.springer.com/10.1007/BF02119584`.

[183] Halbach, M. D., Egert, U., Hescheler, J. & Banach, K. Estimation of action potential changes from field potential recordings in multicellular mouse cardiac myocyte cultures. *Cell. Physiol. Biochem.* **13**, 271–284 (2003). URL `http://www.ncbi.nlm.nih.gov/pubmed/14586171`.

[184] Egert, U., Heck, D. & Aertsen, A. Two-dimensional monitoring of spiking networks in acute brain slices. *Exp. Brain Res.* **142**, 268–274 (2002). URL `http://link.springer.com/10.1007/s00221-001-0932-5`.

[185] Fahrenbach, J. P., Mejia-Alvarez, R. & Banach, K. The relevance of non-excitable cells for cardiac pacemaker function. *J. Physiol.* **585**, 565–78 (2007). URL `http://doi.wiley.com/10.1113/jphysiol.2007.144121`.

[186] Nick, C., Joshi, R., Schneider, J. J. & Thielemann, C. Three-Dimensional Carbon Nanotube Electrodes for Extracellular Recording of Cardiac Myocytes. *Biointerphases* **7**, 58 (2012). URL `http://avs.scitation.org/doi/10.1007/s13758-012-0058-2`.

[187] Brusius, J. *3-dimensionale penetrierende Multielektrodenarrays zur Stimulation und Ableitung in der Retina*. Ph.D. thesis, RWTH Aachen, Aachen (2015). URL `http://juser.fz-juelich.de/record/188924`.

[188] Kim, K. S. *et al.* Large-scale pattern growth of graphene films for stretchable transparent electrodes. *Nature* **457**, 706–710 (2009). URL `http://www.nature.com/doifinder/10.1038/nature07719`.

[189] Wu, F. *et al.* A multi-shank silk-backed parylene neural probe for reliable chronic recording. In *2013 Transducers Eurosensors XXVII 17th Int. Conf. Solid-State Sensors, Actuators Microsystems (TRANSDUCERS EUROSENSORS XXVII)*, June, 888–891 (IEEE, 2013). URL `http://ieeexplore.ieee.org/document/6626910/`.

[190] Irimia-Vladu, M., Głowacki, E. D., Voss, G., Bauer, S. & Sariciftci, N. S. Green and biodegradable electronics. *Mater. Today* **15**, 340–346 (2012). URL `http://dx.doi.org/10.1016/S1369-7021(12)70139-6`.

[191] Lorenzoni, M., Brandi, F., Dante, S., Giugni, A. & Torre, B. Simple and effective graphene laser processing for neuron patterning application. *Sci. Rep.* **3**, 1954 (2013). URL `http://www.nature.com/articles/srep01954`.

Author’s List of Publications

Dmitry Kireev, Dario Sarik, Tianru Wu, Xiaoming Xie, Bernhard Wolfrum, and Andreas Offenhäusser. High throughput transfer technique: save your graphene. *Carbon* **2016**, 107, 319-324

Dmitry Kireev, Ihor Zadorozhnyi, Tianyu Qiu, Dario Sarik, Fabian Brings, Tianru Wu, Silke Seyock, Vanessa Maybeck, Martin Lottner, Benno M. Blaschke, Jose Garrido, Xiaoming Xie, Svetlana Vitusevich, Bernhard Wolfrum and Andreas Offenhäusser. Graphene field effect transistors for in vitro and ex vivo recordings. *IEEE Transactions on Nanotechnology* **2016**, 17, 140-147

Dmitry Kireev, Silke Seyock, Mathis Ernst, Vanessa Maybeck, Bernhard Wolfrum and Andreas Offenhäusser. Versatile flexible graphene multielectrode arrays. *Biosensors* **2017**, 7, 1.

D. Kireev, M. Brambach, S. Seyock, V. Maybeck, W. Fu, B. Wolfrum, A. Offenhäusser. Graphene transistors for interfacing with cells: towards a deeper understanding of liquid gating and sensitivity. *Scientific Reports*, **2017**, 7, 6658.

D. Kireev, S. Seyock, J. Lewen, V. Maybeck, B. Wolfrum, and A. Offenhäusser. Graphene Multielectrode Arrays as a Versatile Tool for Extracellular Measurements. *Advanced Healthcare Materials* **2017**, 6, 1601433.

Wangyang Fu, Lingyang Feng, Gregory Panaitov, **Dmitry Kireev**, Andreas Offenhäusser, and Hans-Joachim Krause. Electrolyte-Gated Graphene Ambipolar Frequency Multipliers for Biochemical Sensing *Nano Letters* **2016**, 16 (4), 2295.

Wangyang Fu, Lingyang Feng, Gregory Panaitov, **Dmitry Kireev**, Dirk Mayer, Andreas Offenhäusser, and Hans-Joachim Krause. Biosensing near the neutrality point of graphene. Accepted to *Science Advances*.

A.V. Emelianov, **D. Kireev**, D.D. Levin, and I.I. Bobrinetskiy. The effect of ultraviolet light on structural properties of exfoliated and CVD graphene. *Applied Physics Letters* **2016**, 109 (17), 173101.

Author’s List of Patents

Dmitry Kireev, Dario Sarik, Bernhard Wolfrum, and Andreas Offenhüsser. “Verfahren zum Transfer von graphen-stuecken auf ein Substrat”, DE 102015016143.1, filed 21.12.2015.

Band / Volume 143
Etablierung eines Systems aus Cysteinmutanten der Phosphoglycerat-Kinase für Entfaltungsstudien mit Einzelmolekül-FRET
A. Schöne (2017), 137 pp
ISBN: 978-3-95806-237-5

Band / Volume 144
Structural and electronic characterization of hetero-organic NTCDA-CuPc adsorbate systems on Ag(111)
S. Schröder (2017), vi, 154 pp
ISBN: 978-3-95806-239-9

Band / Volume 145
Tailoring Molecular Magnetism
T. Esat (2017), viii, 163 pp
ISBN: 978-3-95806-240-5

Band / Volume 146
Spin-wave excitations and electron-magnon scattering in elementary ferromagnets from *ab initio* many-body perturbation theory
M. C. T. D. Müller (2017), vi, 174 pp
ISBN: 978-3-95806-242-9

Band / Volume 147
Neutron Scattering
Lectures of the JCNS Laboratory Course held at Forschungszentrum Jülich and at the Heinz-Maier-Leibnitz Zentrum Garching
edited by T. Brückel, S. Förster, G. Roth, and R. Zorn (Eds.) (2017),
ca 400 pp
ISBN: 978-3-95806-243-6

Band / Volume 148
Neutron scattering
Experimental Manuals of the JCNS Laboratory Course held at Forschungszentrum Jülich and at the Heinz-Maier-Leibnitz Zentrum Garching
edited by T. Brückel, S. Förster, G. Roth, and R. Zorn (Eds.) (2017),
ca 200 pp
ISBN: 978-3-95806-244-3

Band / Volume 149
Kinetic and thermodynamic considerations on the formation of heteromolecular layers on metal surfaces
C. Henneke (2017), vii, 157, XIV pp
ISBN: 978-3-95806-245-0

Schriften des Forschungszentrums Jülich
Reihe Schlüsseltechnologien / Key Technologies

Band / Volume 150
Spectroscopic characterization of local valence change processes in resistively switching complex oxides
C. Bäumer (2017), x, 206 pp
ISBN: 978-3-95806-246-7

Band / Volume 151
Magnetic structure in relation to the magnetic field induced ferroelectricity in Y-type hexaferrite $Ba_{2-x}Sr_xZn_2Fe_{12}O_{22}$
P. Thakuria (2017), 17, 180 pp
ISBN: 978-3-95806-250-4

Band / Volume 152
Statistical analysis tools for assessing the functional relevance of higher-order correlations in massively parallel spike trains
V. Rostami (2017), x, 176 pp
ISBN: 978-3-95806-251-1

Band / Volume 153
The influence of the substrate on the structure and electronic properties of carbon-based 2D materials
J. Sforzini (2017), XIII, 145 pp
ISBN: 978-3-95806-255-9

Band / Volume 154
Gate-All-Around Silicon Nanowire Tunnel FETs for Low Power Applications
G. V. Luong (2017), ii, 136 pp
ISBN: 978-3-95806-259-7

Band / Volume 155
Graphene Devices for Extracellular Measurements
D. Kireev (2017), ix, 169 pp
ISBN: 978-3-95806-265-8

Weitere ***Schriften des Verlags im Forschungszentrum Jülich*** unter
http://wwwzb1.fz-juelich.de/verlagextern1/index.asp

Schlüsseltechnologien / Key Technologies
Band / Volume 155
ISBN 978-3-95806-265-8

Schlüsseltechnologien
Key Technologies
155

Graphene Devices for Extracellular Measurements

Dmitry Kireev

Member of the Helmholtz Association

Graphene Devices for Extracellular Measurements

Dmitry Kireev

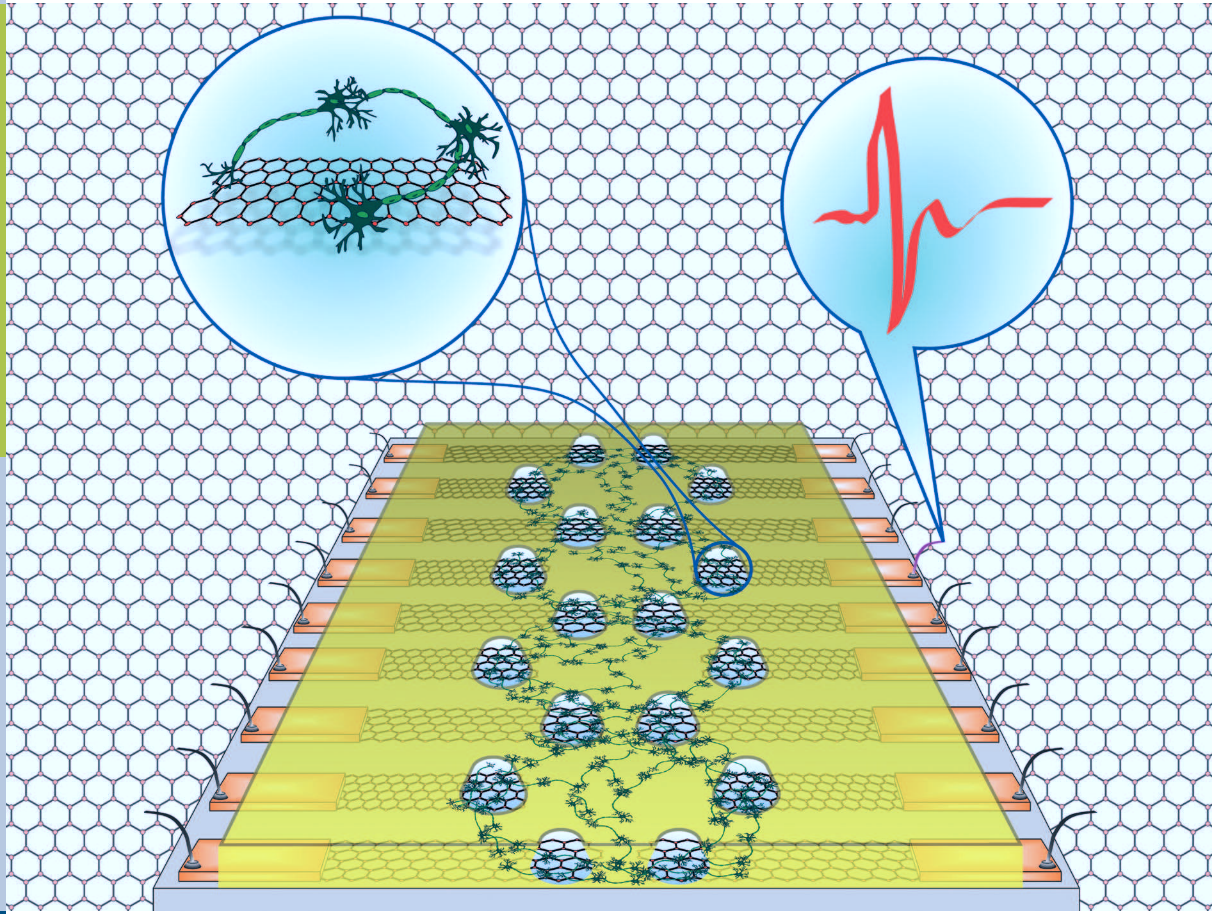

Schlüsseltechnologien / Key Technologies
Band / Volume 155
ISBN 978-3-95806-265-8